Ph. D. Dissertation

Kinetics of charge transfer at the charge transfer layer/halide perovskite interface

Xiangtian Chen

Supervisors:

Dr. Csaba Janáky

Associate Professor

Dr. Gergely Ferenc Samu

Assistant Professor

DOCTORAL SCHOOL OF CHEMISTRY
University of Szeged
Faculty of Science and Informatics
Department of Physical Chemistry and Materials Science

Szeged

2025

Table of Contents

List of Abbreviations

PSC – Perovskite solar cell

LHP – Lead halide perovskites

CTL – Charge transfer layer

ETL – Electron transfer layer

HTL – Hole transfer layer

TRPL – Time resolved photoluminescence

TA – Transient absorption spectroscopy

TR – Transient reflection spectroscopy

PL – Photoluminescence

GSB – Ground state bleaching

SRH – Shockley−Read−Hall

IRF – Instrument response function

CPD – Contact potential difference

SE – Stimulated emission

IA – Induced absorption

CV – Cyclic voltammetry

VB – Valence band

CB – Conduction band

SPS – Surface photovoltage spectroscopy

SPV – Surface photovoltage

FWHM – Full width at half maximum

SEM – Scanning electron microscopy

XRD – X-ray diffraction

UPS – Ultraviolet photoelectron spectroscopy

AFM – Atomic force microscopy

APS – Ambient-pressure photoemission spectroscopy

mp-NiO – Mesoporous-NiO

SC TiO_2 – Single-crystal TiO_2

List of Figures

List of Tables

1. Introduction

Lead halide perovskites (LHP) have received intensive attention in the past decades due to their easy synthesis, high absorption coefficient, long carrier diffusion length, and tunable bandgap.[1] These materials are widely used as active materials in solar cells[2], light emitting diodes[3], photodetectors[4], and lasers[5]. The extensive research effort boosted the power conversion efficiency of lead halide perovskite solar cells (PSCs) over 26% in a decade (**Figure 1**).[6] With efficiencies approaching those of silicon single-junction solar cells, PSCs offer lower production costs due to the abundance of materials and low-temperature synthesis methods. The composition tunable light absorption of lead halide perovskites allows the preparation of tandem solar cells. These can utilize a wider range of the solar spectrum and achieve even higher conversion efficiencies than their single-junction counterparts (**Figure 1**).[7] Additionally, lead halide perovskites can be deposited on a variety of substrates, including flexible ones, offering opportunities for wearable devices.[8]

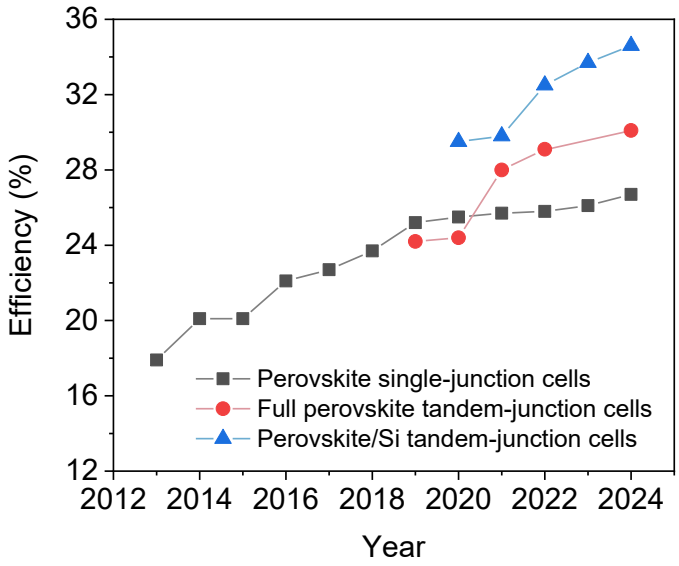

Figure 1. Improvement of perovskite solar cell efficiency (data extracted from NREL database). [9]

PSCs typically have multiple components, namely a light absorption layer, electron extraction and hole layers, and metal contacts. In these architectures, the lead halide perovskite layer absorbs light and generates photo-excited charge carriers (electrons and holes). Free electrons and holes can be transported to the charge transfer layer

(CTL)/perovskite interface and in a subsequent step extracted and collected. Undesired carrier recombination at various trap states in the bulk and interfacial regions leads to carrier losses, deleteriously influencing carrier collection. To improve the efficiency (and stability) of PSCs, suppressing these carrier loss pathways is crucial. Current strategies focus on improving the quality (e.g., crystal quality and interface quality) of the lead halide perovskite layer and CTLs, passivating trap states both in the bulk and on the surface. The thermodynamic driving force behind efficient charge separation and extraction is related to the band energetics (band positions, alignment, and offset) at the CTL/LHP interface. *However, as the charge extraction process is convoluted, exact design principles were not yet established*. Some studies state that large band position offsets at CTL/perovskite interface are beneficial for assisting charge transfer.[10–12] Other studies argue that smaller band position offsets at this interface facilitate smoother charge transfer.[13–15]

By examining and understanding the fate of excited charge carriers design rules can be established that can aid the material choices for PSCs. Charge generation, recombination, and transfer processes typically occur on a short time scale (e.g., from fs to ns). Ultrafast techniques are required to track these processes, such as transient absorption spectroscopy (TA), time-resolved photoluminescence (TRPL), time-resolved microwave conductivity and transient surface photovoltage. Among them, TA and TRPL are the most commonly used techniques. Comparing the determined charge carrier transfer rate constants with these techniques, a large dispersion can be observed in the reported values, ranging from transit times between a few femtoseconds to tens of nanoseconds. Different factors can contribute to this variability, including sample properties, measurement parameters, measurement environment, and evaluation methodology. *To further aid device design, it is crucial to understand the role these factors play in the determination of the charge carrier transfer rate constants and effort must be devoted to minimize the observed dispersion.*

Built-in/applied electric fields present in PSCs can also influence charge carrier dynamics and device stability. Therefore, it is important to understand how the applied electrical bias can influence charge separation, accumulation, and transfer. Operando spectroelectrochemical techniques can be used to monitor the influence of selective charge

carrier injection in in CTL/perovskite half-cell assemblies, with electron transfer layer (ETL) and hole transfer layer (HTL) separately. *To reliably and accurately reveal the influence of external electric bias on the electron/hole injection process through the interfaces the electrochemical stability window of these perovskite layers must be determined* (to avoid undesired phase/chemical changes of perovskite layer).

1.1 Lead halide PSCs

The term 'perovskite' describes a class of materials with the stoichiometry ABX_3. The first discovered perovskite has a chemical compound of $CaTiO_3$. Perovskite structure's tolerance for site substitution enables the development of a new class of perovskites, namely LHP. Typically, the A site hosts a monovalent organic or inorganic cation, such as methylammonium (MA^+), formamidinium (FA^+), and K^+, Rb^+, Cs^+. The B site can be a divalent metal cation, including Pb^{2+}, Sn^{2+}, or Ge^{2+}. The X site is usually halide anions such as F^-, Cl^-, Br^-, or I^-. The material adopts a crystal structure of corner-linked BX_6 octahedrons. By tuning the composition of LHP, especially the X site, we can easily tune the bandgap and band position of the material.[16] This allows for the possibility of full perovskite tandem-junction solar cells. Mixing organic and inorganic cation can provide a balance between PSCs efficiency and stability.[17] Instability is still the major issue of PSCs. LHP is sensitive to many environmental factors, such as humidity, light, oxygen, and heat. LHP material and PSC structure optimizations are still needed to further improve the efficiency and stability of PSCs.

1.1.1 The architecture of PSCs

Lead halide perovskites were initially used in a similar architecture to dye-sensitized solar cells. In these, a ~ 10 μm mesoporous metal oxide scaffold (e.g., TiO_2) acted as an ETL, and the LHP was anchored to this layer. The sensitizer (lead halide perovskite) absorbs light and generates electrons and holes. These excited electrons are then injected into the mesoporous metal oxide scaffold, and holes are transferred to a redox-active electrolyte (e.g., I_2/I_3^-). However, due to the instability of the perovskite layer when contacted with liquid electrolytes, rapid performance degradation was observed.[18] To tackle this instability, solid-state devices were developed by replacing the liquid electrolyte with a hole-transporting

layer (e.g., spiro-MeOTAD, **Figure 2A**).[19,20] Apart from improving the stability, simultaneously the power conversion efficiency was also boosted from 3.8%[18] to 15%[19]. It was also demonstrated that the electron conductive mesoporous scaffold (TiO_2) can be substituted for an insulating Al_2O_3 scaffold.[21] This Al_2O_3 could be thinned down to ~ 80 nm, while the perovskite layer thickness could be further increased (400 nm).[22] This was the first example of lead halide perovskite thin film solar cells (**Figure 2B**).[22] Together with the appearance of HTL free PSCs[23], the ambipolar charge transport of metal-halide perovskites was recognized, which led to the rise of planar PSCs.[24] Substituting the mesoporous metal-oxide scaffold to thin film charge transfer layers can allow the use of a simpler processing procedure, where milder annealing temperatures (~500 °C) can be used.

PSCs can be prepared in two different arrangements, depending on the order of the layer deposition: n–i–p (**Figure 2C**) and p-i-n (**Figure 2D**). The choice of CTL materials is different in these arrangements as in some metal halide compositions high temperature annealing steps must be avoided. In conventional n-i-p arrangements an n-type semiconductor (e.g.,TiO_2, ZnO, and SnO_2) is deposited on transparent conductive substrates (e.g., FTO) and used as an ETL. On top of the ETL an intrinsic (i) semiconductor (e.g., metal-halide perovskite thin film) is deposited. The PSC is completed by a p-type semiconductor, such as spiro-MeOTAD, P3HT, and CuSCN acting as an HTL. On the contrary, inverted p-i-n PSCs adopt an opposite structure. A p-type HTL, such as PEDOT:PSS, poly[bis(4-phenyl)(2,4,6-trimethylphenyl)amine] (PTAA), and NiO, is deposited on the FTO. Then followed by a sequential deposition of the perovskite layer and the ETL, such as $PC_{61}BM$, C_{60}. Conventional ETL (e.g.,TiO_2, ZnO, and SnO_2) cannot be used as they require high temperature sintering, which can damage perovskite layer. Although PSCs is n-i-p architecture show slightly better power conversion efficiency, PSCs with the p-i-n architecture generally show better stability and are better suited for tandem photovoltaic applications.[25]

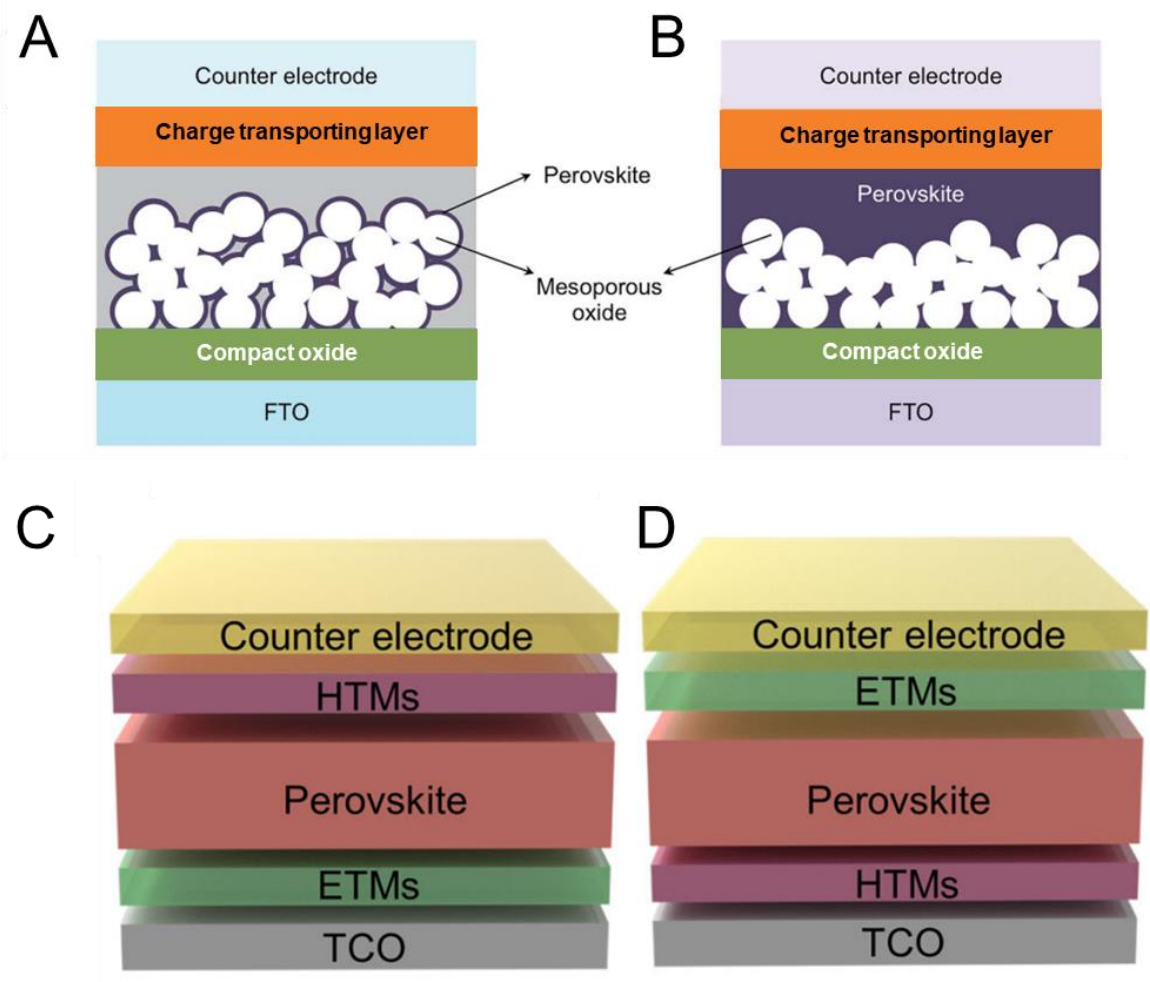

Figure 2. The architecture of lead halide PSCs. (A) mesoscopic architecture with a thin perovskite layer. Adapted from ref [26]. (B) mesoscopic architecture with a thick perovskite thin film. Planar architecture in (C) "n–i–p" order and (D) "p–i–n" order. Adapted from ref[27].

In all arrangements an appropriate band alignment is a necessity to ensure successful charge separation, extraction and collection (**Figure 3**). After light absorption in the perovskite layer the formed excitons dissociate into free carriers (small exciton binding energy at room temperature). The potential difference between electrons in the conduction band (CB) and holes in the valence band (VB) results in an internal voltage, which is referred to as quasi-Fermi level splitting (QFLS).[28] The excited electrons can only be extracted by the ETL if the used material possesses a lower-lying CB compared to the LHP. In the meanwhile, the VB of ETL should be lower than the LHP to block the excited holes. Similarly, the excited holes in the VB can only be extracted by an HTL with a higher-lying VB than the LHP. Higher CB of HTL than the LHP is required to inhibit the excited electrons

transfer to HTL side. This arrangement ensures successful separation of the excited electrons and holes and suppresses electron-hole recombination. To passivate interface trap states, alleviate possible interfacial energy barrier, and assist better conductivity, an interlayer (e.g., graphene**,** fullerene C_{60} and its derivatives, and excess PbI_2) can be inserted between the LHP and ETL or HTL.[29] In some cases, insulating interlayers are employed, such as polystyrene and Teflon. The thickness of these insulating interlayers must be precisely controlled within 1–2 nm to enable electron tunneling.[29] Some interlayers can also protect the LHP from moisture and boost the stability of PSCs.[30] Theoretically, the achievable open circuit voltage (V_{OC}) should be equal to QFLS. However, the measured V_{OC} always differs from QFLS, caused by recombination losses, both in bulk and interfacial processes (**Figure 3**).[28,31]

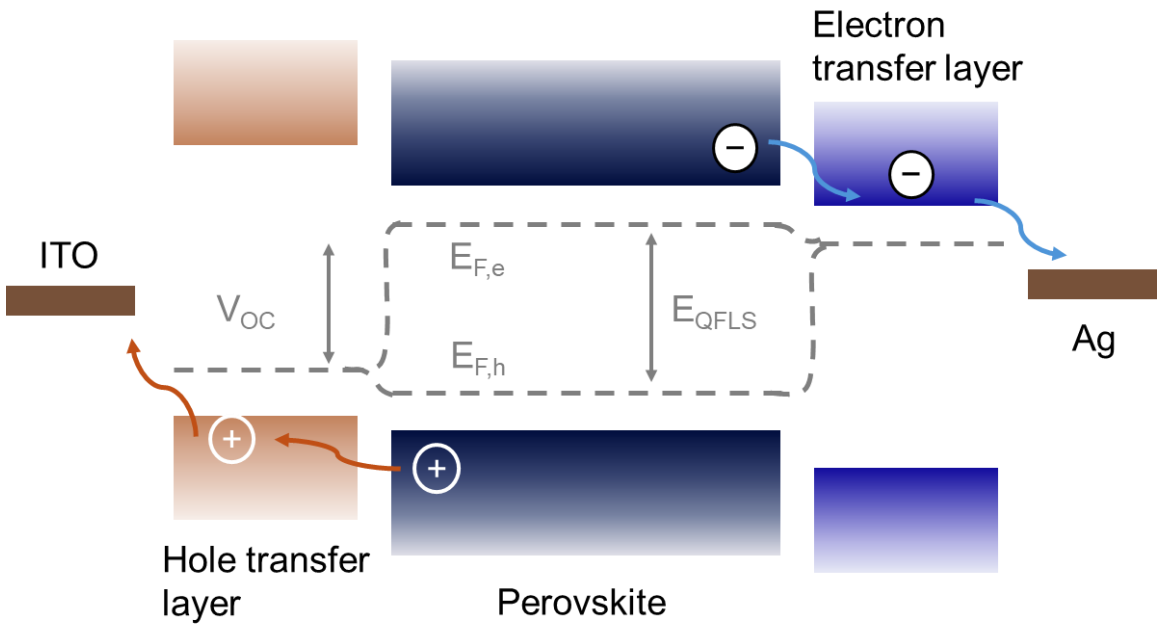

Figure 3. Schematic diagram of band alignment and quasi-Fermi level splitting of a functioning PSC.

1.1.2 The fate of generated charge carriers

In LHP devices, the fate of the excited carriers after light irradiation is a convoluted process. **Figure 4** represents a detailed photophysical picture, highlighting processes occurring in a CTL/perovskite assembly after light excitation, together with the corresponding time scale of these processes. Excitation with larger energy than the LHP band gap forms hot carriers within the LHP layer. These hot carriers thermalize and cool down to the CB of the

perovskite within 1 ps.[32,33] Direct extraction of these hot carriers is an extensively studied area as it can lead to higher solar cell efficiencies, surpassing the Shockley–Queisser limit.[34] The thermalized charge carriers at the CB edge undergo either trapping or radiative band to band recombination (without the use of CTLs). The time scale of these two processes extends from picoseconds to microseconds.[35] The trapped charge carriers can live as long as 10 microseconds[36], and then participate in various non-radiative recombination processes with free carriers. Charge carriers that escape recombination and trapping can diffuse (or migrate) to the respective CTL/perovskite interface to be extracted. However, the existence of interfacial defects can cause additional carrier losses or even introduce an energy barrier which hinders the charge transfer process.[37] The time scale of the diffusion process depends on the thickness of the perovskite layer. Charge transfer is generally interpreted to be a fast process, which extends from picoseconds to nanoseconds.[35] The reason for this large dispersion will be discussed in detail in the following paragraphs. Charge transfer and charge recombination/trapping are competitive processes. Suppressing charge carrier recombination/trapping and facilitating charge transfer lead to less carrier losses and thus an efficiency enhancement of PSCs.

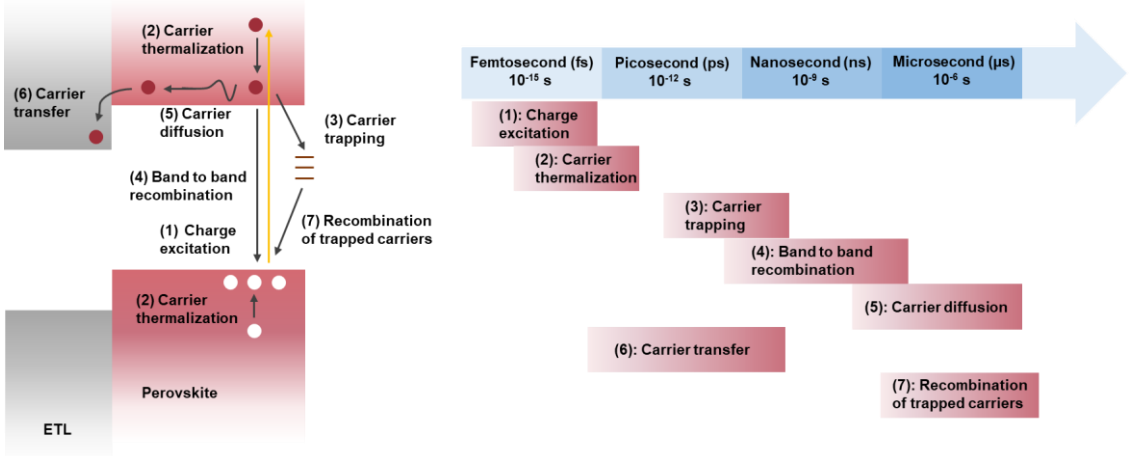

Figure 4. Schematic diagram of the photophysical processes occurring in a CTL/perovskite assembly following light excitation, together with the corresponding time scale of these processes. Reproduced from ref[35].

1.1.3 Methods to improve PSC efficiency

Although single-junction PSCs have achieved efficiencies exceeding 20% in recent years,

this remains below the theoretical Shockley–Queisser limit of 33%.[38] There are still ample room for further improvement. In this vein, focus is devoted to improving the properties of the perovskite layer itself by material engineering and trap state management (**Figure 5**).[39] For example, solvent and template engineering can control the crystallization process, achieving perovskite layers with large grain size, dense microstructure and uniform morphology.[40,41] These features usually lead to less intrinsic trap states and thus mitigate carrier recombination losses. Perovskite composition tuning, such as doping at cation and anion sites, helps to achieve a suitable bandgap and thus a higher V_{OC}.[42] Additionally, small amount of Cs and Rb can also increase the stability of perovskite layers suppressing phase segregation.[43] Trap state passivation at the surface or at the CTL/LHP interface with PbI_2[44,45], PEAI salt[46], or PMMA[47] can reduce extrinsic trap densities and suppress non-radiative recombination carrier losses.

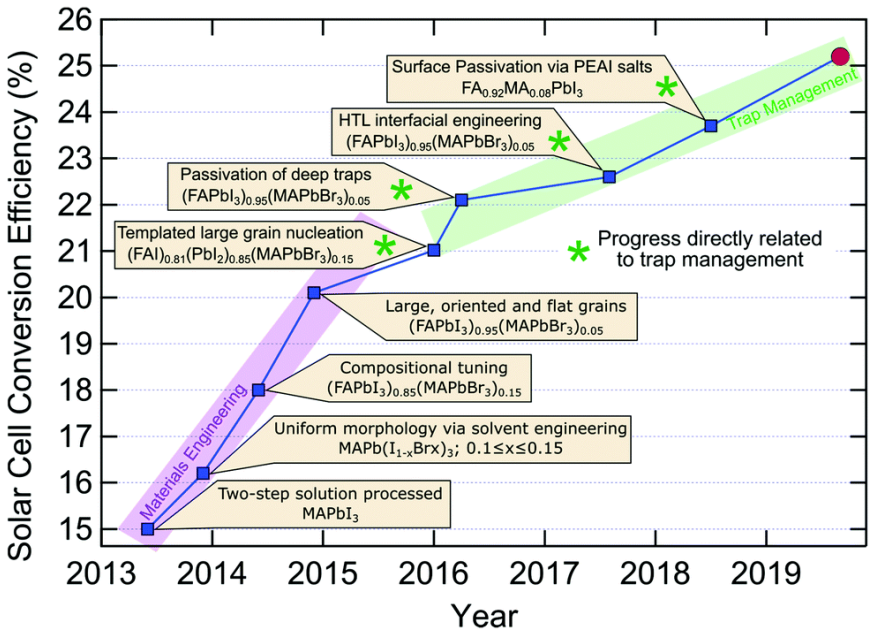

Figure 5. Methods to improve the efficiency of PSCs focusing on optimizing perovskite layer itself. Reproduced from ref[39].

Further PSC efficiency improvements can be realized by carefully optimizing the properties of CTLs, that also directly participate in the charge extraction process. CTLs in high-performing PSCs must meet several criteria, which fall into three main categories regarding electronic, optical and chemical properties. (**Figure 6**). CTLs should have an appropriate

band alignment with the corresponding perovskite layer to form the built-in electric field for charge separation. Generally, a CB position with lower energy is needed for an ETL and a VB position with higher energy is needed for a HTL. As stated previously it remains controversial whether a large energy offset will result in a more efficient charge transfer. Some studies suggest that a lower energy level offset at the interface creates an easier pathway for charge transfer.[13–15] Therefore, either interlayers[48] or hybrid layers[13] with smaller band offsets are incorporated between the CTL/LHP to assist charge transfer and collection. Contrastingly other studies indicate that larger energy offset at the interface offers a higher thermodynamic driving force and thus facilitates charge transfer.[10–12] CTLs possessing a high charge carrier mobility can improve charge transport and collection, which leads to less charge accumulation at the interface, suppressing back recombination and current–voltage hysteresis.[49] The population of trap states in CTLs also need to be minimized to reduce carrier recombination losses. A balanced carrier extraction is vital to avoid carrier accumulation on both sides of CTL/perovskite interfaces. Contact potential difference (CPD) mapping conducted by kelvin probe force microscopy (KPFM) has revealed an accumulation of holes at the HTL/perovskite side, indicating hole extraction at HTL/perovskite is slower than electron extraction at ETL/perovskite interface.[50,51] This hole accumulation caused by unbalanced charge separation can lead to severe current–voltage hysteresis thus a lower device performance. Furthermore, CTLs should have a wide bandgap and a small refractive index to minimize the parasitic absorption and undesired scattering of sunlight.[52] UV-light and chemical stability are also essential properties to prevent gradual performance degradation. Commonly used CTLs include inorganic ones and organic ones. Examples of them are listed in **Table 1**. Generally, organic CTLs based PSCs demonstrate higher efficiency, but show relatively lower stability compared to PSCs prepared from inorganic CTLs due to ion diffusion into the structure.[53] In this thesis, TiO_2 and NiO_x are used as ETL and HTL for investigation. Detailed introduction of these two materials as CTLs are given in the following paragraphs. Further investigation and optimization in CTLs, especially in HTLs, are essential to improve the performance of PSCs.

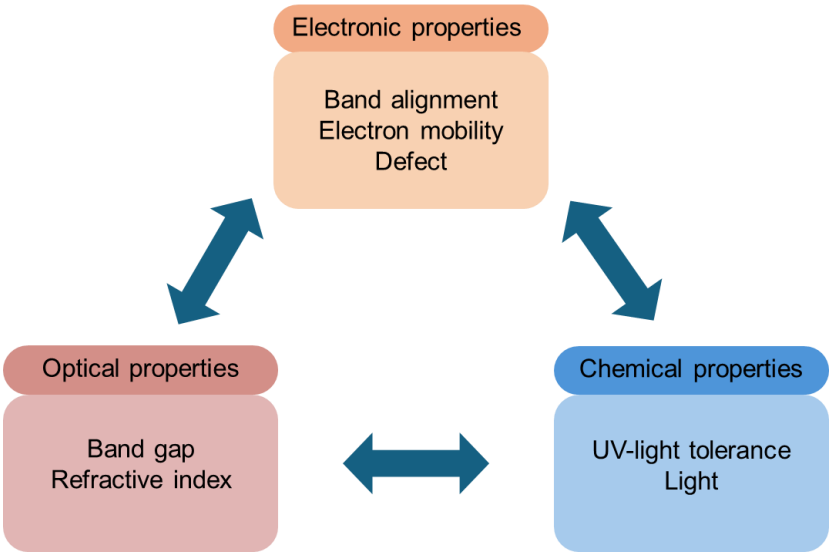

Figure 6. Essential properties of an ideal CTL. Adapted from ref[52].

Table 1. Examples of commonly used CTLs.

Inorganic ETLs	organic ETLs	Inorganic HTLs	organic HTLs
TiO_2, ZnO, SnO_2, Nb_2O_5	fullerenes and their derivatives (e.g., PCBM and C_{60})	NiO_x, Cu_xO, CuSCN, CuI	Spiro-OMeTAD, PEDOT:PSS, PTAA and P3HT

TiO_2 as an ETL

TiO_2 has been extensively used in n-i-p configuration PSCs as an ETL because of its suitable CB position, high thermal stability, good transparency, and low cost.[54] However, there are also some drawbacks associated to this material which hinders the further improvement of TiO_2 ETL-based PSCs. For example, slow electron mobility in TiO_2 can cause electron accumulation at the interface, and high density of surface trap states (e.g., oxygen vacancies) can lead to fast carrier recombination.[55] Additionally, UV light instability of TiO_2 ETLs results in the light-induced desorption of oxygen adsorbed on the surface causing critical performance degradation of PSCs.[56] To mitigate these limitations, various modification methods have been developed, such as doping[11], surface treatment[57], and interface engineering [58]. TiO_2 doped with metal ions, such as Li, Nb and Mg, has higher electrical conductivity.[11] Doping can also tune the CB of TiO_2, enabling more efficient charge extraction.[11] $TiCl_4$ surface treatment is a common method to suppress surface trap states of

TiO_2 and reduce carrier recombination at the TiO_2/perovskite interface.[57] A similarly effective strategy is interface passivation with very thin insulating layers (e. g., MgO, Al_2O_3, ZrO_2).[58] Crystal-facet engineering, which has been demonstrated in photoelectrochemistry[59] and photocatalysis[60] field, is also an effective method. Crystallographic orientation of the TiO_2 ETL can also influence the band positions, thus influence charge transfer properties. Transient absorption (TA) spectroscopy has revealed that electron transfer from $MAPbI_3$ to TiO_2 (100) and (110) facets are faster than (001) facet.[61] Single-crystalline TiO_2 nanoparticle ETLs, with high electron mobility and low density of defects, were shown to be a good choice for PSCs.[62] The derived devices show an efficiency of 24.05% with exceptional long-term stability (1400 h). Also, the possibility to fabricate large-area modules based on these single-crystalline TiO_2 nanoparticle ETLs can be achieved.

NiO_x as an HTL

NiO_x is a commonly used HTL, especially in p-i-n configuration PSCs. NiO_x has a wide band gap (~3.7 eV),[63] ensuring transparency to solar light. A deep valence band position of NiO_x allows hole extraction from perovskite layers. PSCs fabricated from NiO_x possess imrpoved photo and thermal stability, owing to the stable crystal structure and non-corrosive properties of NiO_x.[64] Various methods are being explored to prepare NiO_x layers, including electrodeposition, sol-gel method, combustion, sputtering, and atomic layer deposition.[65] The chosen deposition technique will have a large impact on the cost and quality of the prepared NiO_x layers. Similarly to TiO_2, undoped NiO_x has a low conductivity, which can cause hole accumulation at the NiO_x/perovskite interface. The Fermi level of NiO_x is relatively far from its valence band position, resulting in a small built-in electric field at the NiO_x/perovskite interface (required for charge separation).[64] Elements like Cu[66], Li[67], Mg[68] and N[69] have been demonstrated to be effective dopants for improving conductivity and tuning the Fermi level, resulting in efficiency improvements in PSCs. UV ozone and oxygen plasma treatment is a convenient surface treatment method, which introduces more polar NiOOH species at the surface and thus leads to a higher work function.[65] It can also improve the adhesion and uniformity of the deposited perovskite layer on NiO_x. Nevertheless, the

surface work function tuning effect of oxygen plasma treatment is limited. Surface modification with organic monolayers, such as 4-cyanophenylphosphonic acid[70] and diethanolamine (DEA)[71], provides possibility for larger work function adjustments. This method is also effective in improving interface contact and thus achieving a higher fill factor and a better performance for PSCs.[71]

1.2 Charge transfer at the CTL/perovskite interface

1.2.1 Methods used to probe charge transfer processes

To better understand the mechanism of charge transfer at the CTL/perovskite interface, various techniques (with differing applicable time-domains), such as time-resolved microwave conductivity[72,73] transient surface photovoltage[74], time-resolved photoluminescence (TRPL), and transient absorption/reflection (TA/TR) spectroscopy can be used. Time-resolved microwave conductivity can probe processes occurring on several hundreds of nanoseconds to several microseconds time scales. [72,73] Transient surface photovoltage can resolve time scale down to several microseconds, while surface photovoltage can expand to the second time scale.[74] TRPL and TA/TR are the most widely utilized methods to evaluate the kinetics of charge transfer as their time scale expands from femtoseconds to nanoseconds and will be the focus of the following chapters.[75]

TRPL

TRPL employs pulsed laser to excite the sample and uses time-correlated single-photon counting (TCSPC) to record the photoluminescence intensity decay trend. TRPL can be used to probe the relaxation kinetics of the excited charge carriers in various perovskite materials. This method indirectly contains information on the charge carrier transfer rate to charge extraction layers. As the same pool of free carriers participates in both radiative and non-radiative recombination channels, the radiative decay of the PL signal will be influenced by the presence of trap states and charge carrier transfer. By coupling modeling, the measurement can be extended to determine charge carrier diffusion lengths and charge transfer yields. TRPL results are shown to be also in good correlation with PSC performance.[76] It is important to note that steady-state PL spectroscopy is also an important

method to show the effect of the CTLs on excited charge carrier in perovskite layers. The quenching of the PL signal can indicate charge transfer of excited charge carriers from the perovskite layers to the CTLs. Photoluminescence quantum yield (PLQY) is also an additional parameter that can be included in elaborate modelling studies.

TA/TR spectroscopy

TA is a pump-probe technique which employs short laser pulses and can resolute processes in the sub-picoseconds time range. The pump pulse is used to excite the sample and a probe pulse to monitor the change in absorption of the sample before and after excitation. In contrast to TRPL measurements, TA/TR spectroscopy can directly probe both radiative and non-radiative carrier relaxation processes. When performing TA measurements, the probe light passes through the perovskite sample, primarily capturing the bulk properties of the perovskite films (influenced by carrier diffusion). By contrast, the reflected light from the sample surface is recorded in TR mode, which is induced by the change of the refractive index after light excitation. This measurement mode is very sensitive to surface-related processes, such as surface charge carrier recombination.[77] Perovskites have their characteristic ground state bleach (GSB) signal, induced by the excited carriers at the conduction band of perovskite after bandgap excitation. The recovery of GSB indicates charge carrier recombination, trapping or charge extraction with the presence of CTLs. TA/TR spectroscopy can also monitor the formation and decay of hot carriers (above bandgap excitation), which processes occur only in the first several picoseconds, which fall outside the detection range of TRPL measurements.[78] Comparing the broadening of the TA/TR spectra on the higher energy side with and without CTLs can shed light on the hot carrier extraction kinetics in these assemblies.[78] Additionally, the probing wavelength can be shifted to the infrared region. In this manner, transient signals related to the presence of electrons in the CB of the ETLs (e.g., TiO_2)[61,79] or holes in the VB of the HTLs (e.g., PEDOT)[80] can be observed. This can serve as a complementary tool to probe the charge transfer process. However, it should be noted that usually high-intensity excitation fluence needs to be applied due to the low signal intensity in the infrared range. The possible presence of higher-order recombination processes in such situations needs to be considered.

1.2.2 Analysis methods

Different evaluation protocols are generally used to determine charge transfer rates from TRPL and TA/TR decay curves. This includes:

(i) (multi)exponential fitting,

(ii) stretched exponential fitting,

(iii) calculation of the effective lifetime and using the charge transfer rate equation,

(iv) modeling and global fitting.

Among these methods, (multi)exponential fitting is the most frequently used approach due to its convenience in achieving a decent fit by increaseing the number of exponential components.

$$I(t) = A_0 + A_{CT}exp^{\left(-\frac{t}{\tau_{CT}}\right)} + A_T exp^{\left(-\frac{t}{\tau_T}\right)} + A_{recomb}exp^{\left(-\frac{t}{\tau_{recomb}}\right)} \quad (1)$$

When attributing these time constants to physical processess in a CTL/perovskite bilayer, the longest lifetime component is usually attributed to band-to-band recombination, A_{recomb} and τ_{recomb} are the amplitude and lifetime of this recombination processes, respectively. The middle component (A_T and τ_T) is usually related to charge trapping or non-radiative recombination at defect sites, and the fastest component (A_{CT} and τ_{CT}) is interpreted as charge transfer from perovskite to CTL. Disentangling charge transfer from trap state related recombination is not straightforward, and often one component is used, merging these two processes.[81] With this analysis method, one can calculate the charge transfer rate constant (k_{CT}) by taking the reciprocal of the charge transfer lifetime:

$$k_{CT} = \frac{1}{\tau_{CT}} \quad (2)$$

However, the arbitrary number of exponential components in this method makes the physical meaning of the components ambiguous. To avoid such arbitrary fitting and ambiguity, one can calculate the charge transfer lifetime using the charge transfer equation (3):

$$\frac{1}{\tau_{CT}} = \frac{1}{\tau_{CTL/perovskite}} - \frac{1}{\tau_{perovskite}} \quad (3)$$

where $\tau_{CTL/perovskite}$ and $\tau_{perovskite}$ is the effective lifetime of CTL/perovskite sample and bare perovskite sample, respectively. Effective lifetime can be calculated by the following

equation:

$$I(\tau_{ef}) = \frac{I(0)}{e} \tag{4}$$

Where *I(0)* is the intensity of photoluminescence or absorption at time 0. The advantage of employing an effective lifetime and charge transfer equation is that the result is independent on the used fitting function. Stretched exponential function can be used when TRPL and TA/TR decays deviate significantly from ideal cases:

$$I(t) = \sum_{i=1}^{n} A_i exp^{\left(-\frac{t}{\tau_i}\right)\beta_i} \tag{5}$$

The deviations are described by β_i ($0<\beta_i<1$), which represents the spatial inhomogeneity in perovskite layers.

The most widely used modelling methods are the ABC model and Shockley−Read−Hall (SRH) model.[36] In ABC model, the photogenerated charge carrier density can be modeled through decaying in three processes: (i) first-order, which includes charge trapping, and charge extraction by CTLs, (ii) a second-order electron-hole recombination process, and (iii) a three-body Auger recombination process:

$$-\frac{dn}{dt} = An + Bn^2 + Cn^3 \tag{6}$$

Here, n is the photogenerated charge carrier density; A, B and C are the rate constants of the respective processes, and t is the time after photoexcitation. If one wants to obtain a more accurate model, separating the process of electrons and holes can be considered by the SRH+ model:

$$\frac{dn}{dt} = G(t) - k_r np - k_t(N - n_t)n - k_E np(N - n_t) - k_A np^2 \tag{7}$$

Similarly, *G(t)* is the photogenerated charge carrier density at time t; n is the free electron density and p free hole density, n_t is the density of electrons being trapped, N is the trap state density, and k_r, k_t, k_E, k_A are the rate constants of radiative recombination, electron trapping, Auger-assisted electron trapping, and Auger-assisted electron−hole recombination, respectively. When both k_E and k_A can be neglected ($k_E = 0$, and $k_A = 0$), SRH+ model can be simplified into SRH model. When no electrons are trapped ($n_t = 0$), which means $n = p$, then SRH+ model can be simplified into ABC model. When perovskite is interfaced to a CTL,

one more process (i.e. charge transfer process) needs to be added to the rate equation.[82] Furthermore, the diffusion process can also be added to deconvolute charge transport and charge transfer.[83,84] Additionally, a differential lifetime approach has been proposed to visually distinguish the two lifetimes resulting from transfer and from interfacial recombination, especially in the low excitation fluence regime.[85] This approach has the advantage that all information about how the decay changes with time is retained.

1.2.3 Parameters influencing charge transfer kinetics

There are different parameters that can affect the kinetics of the charge carriers after light excitation. They can be summarized in two categories: (i) perovskite layer quality, such as trap states densities at grain and crystal boundaries, and interfaces (**Figure 7**); and (ii) measurement parameters, such as excitation fluence, wavelength, repetition rate, and direction. In the case of TRPL, it is also very sensitive to perovskite layer light soaking time and measurement atmosphere. As a result of these contributing factors, the measured carrier extraction rate constants can vary significantly. A selection of examples is presented in **Table 2**.

Table 2. The variation of reported lifetimes (τ) related to charge transfer in different CTL/$CH_3NH_3PbI_3$ assemblies. Reproduced from ref[35].

Method	Architecture	Measurement parameters	τ_{CT}	Rate Constant (10^7 s^{-1})	Reference
TRPL	TiO_2/$CH_3NH_3PbI_3$	λ_{exc} = 625 nm, 0.1 μJ cm^{-2}	11 ns	9.1	86
		λ_{exc} = 464 nm, unknown fluence	2.1 ns	47.6	87
		λ_{exc} = 640 nm, unknown fluence	9.7 ns	10.3	88
TAS	Compact-TiO_2/$CH_3NH_3PbI_3$	λ_{exc} = 400 nm, 10 μJ cm^{-2}	370 ps	270.3	89
		λ_{exc} = 370 nm, 3.0 μJ cm^{-2}	<10 ps	>10000	90
		λ_{exc} = 485 nm, 0.5 – 75 μJ cm^{-2}	50 ns	2.0	91

TRPL	Spiro-MeOTAD/$CH_3NH_3PbI_3$	λ_{exc} = 600 nm, 1.3 μJ cm^{-2}	0.7 ns	142.9	[92]
		λ_{exc} = 625 nm, <0.1 μJ cm^{-2}	1.8 ns	55.6	[86]
	Spiro-MeOTAD/FAMA perovskite	λ_{exc} = 460 nm, 0.4 W cm^{-2}	100 ns	1	[93]
TAS	Spiro-MeOTAD/$CH_3NH_3PbI_3$	λ_{exc} = 600 nm, 10.0 μJ cm^{-2}	0.7 ns	142.9	[92]
		λ_{exc} = 460 nm, 2.0 μJ cm^{-2}	0.8 ps	125000	[79]
		λ_{exc} = 485 nm, 0.5 - 75 μJ cm^{-2}	17 ns	5.9	[94]

Perovskite layer quality

Perovskite layers have a granular structure, leading to the existence of various interfaces (i.e. grain boundaries). These interfaces are rich in defect states, which arise from crystal strain and element vacancies. Charge carrier recombination at defect states is one of the most significant factors contributing to efficiency losses in PSC devices. Furthermore, the time scale of charge carrier recombination falls into a similar scale of the charge transfer process, making it difficult to deconvolute these two processes.[94] Therefore, influence of such charge carrier recombination can affect the observed charge transfer kinetics.

The different photophysical behaviors of excited charge carriers at grain boundaries and interfaces are demonstrated by different experimental results. Lower PL intensity, PL quantum yield, and lifetime are found at grain boundaries[95] and crystal misorientation sites[96]. Moreover, charge carrier recombination at defect sites is found to be more severe in perovskite layers with smaller grain sizes.[97] Because excited charge carriers are more accessible to grain boundaries in these layers. Additionally, grain boundaries are also found to reduce the observed hole mobilities.[98] However, it has less effect on electron mobility. Such property leads to asymmetric charge carrier transport in perovskite layers.[98]

Defect states are also formed at interfaces, such as the HTL/perovskite, ETL/perovskite interface, and also on bare perovskite surfaces. Charge carrier recombination losses were

found to be more severe at these interfaces than at grain boundaries.[77,99] Surface-sensitive TR measurements have shown that surface recombination in polycrystalline perovskite layers influences the determined carrier lifetime more strongly than bulk and grain boundary recombination processess.[100] The severe surface recombination can be effectively suppressed by employing proper passivation layers.[46,100,101]

Charge carrier dynamics also depends on the thickness of perovskite layers. Following light excitation, the generated free charge carriers first have to diffuse to CTL/perovskite interface to be extracted. The diffusion distance depends on the perovskite layer thickness if the excitation is not carried out directly at the CTL side. Previous studies have revealed that an increase in perovskite thickness leads to a reduction in the charge carrier transfer rate.[102,103] When similar perovskite films were deposited on inert substrates perovskite layer thickness-independent PL lifetimes were determined (indicating constant layers qualities, and the absence of diffusion-limited processes).[103] When perovskite films were deposited on CTLs, an acceleration of the excited state recovery was observed due to charge extraction. Moreover, such acceleration was more significant on thin perovskite layers due to the differences in diffusion distances of excited carriers before being extracted.[103] These results demonstrate that diffusion and interfacial charge transfer jointly influence the overall charge transfer rate.

The back contact texture can alter the contact area of the perovskite layer with the substrate. This feature can also lead to variation in carrier lifetimes, as a rough or a mesoporous back contact can lead to internal light-scattering effects and photon recycling.[104] Photons can be reabsorbed and re-emitted and thus influence the carrier distribution within the perovskite film, resulting in higher PL quantum efficiencies and lifetimes.[105,106]

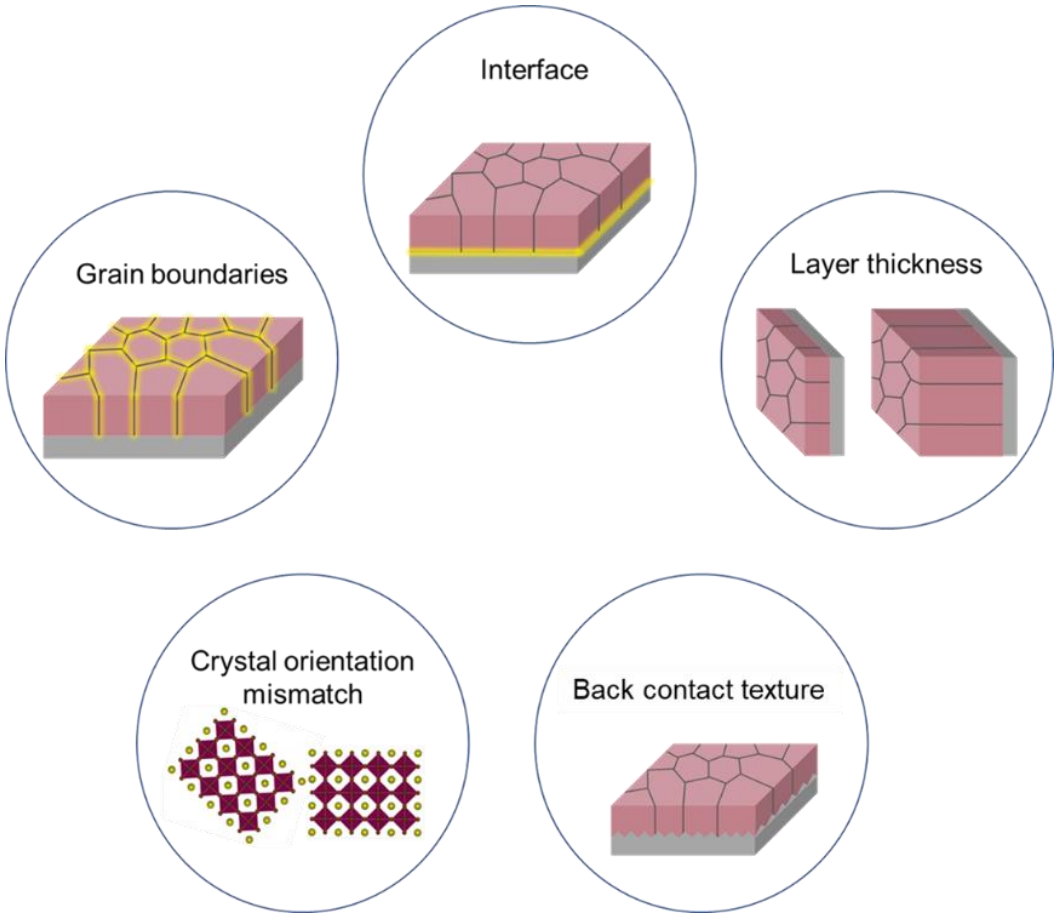

Figure 7. Schematic representation of the perovskite layer properties which influence charge carrier dynamics and thus affect the observed charge transfer kinetics. Reproduced from ref[35].

Measurement parameters

TRPL measurements generally employ nanosecond excitation laser pulses, while TA/TR measurements use femtosecond pulsed lasers which allows them to probe sub nanosecond processes (e. g. hot carrier relaxation). The probing time frame of TRPL and TA/TR measurements are also different, which results in different observed excited carrier lifetimes from the two methods. Other measurement parameters, such as excitation fluence, wavelength, and repetition rate (see **Table 3**), can also induce variation in the observed carrier dynamics, thus influencing the calculated charge transfer rate.

Table 3. Experimental parameters of TRPL measurements and their effect on the different

photophysical processes in CTL/perovskite assemblies. Reproduced from ref[35].

Excitation fluence	Excitation wavelength	Excitation direction
• Trap state filling • Influence band-to-band charge carrier recombination • Influence charge extraction • Possible charge accumulation • Induce Auger recombination at high fluence	• Excitation energy • Penetration depth • Density of mobile ions caused by produced phonons	• Fast decay from perovskite/CTL side • Disentangle diffusion effects
Excitation frequency	**Illumination time**	**Measurement atmosphere**
• Trap states depopulation • Influence band-to-band charge carrier recombination • Influence charge extraction	• Trap state filling • Photoluminescence brightening • Ion migration caused by band bending change	• Oxygen curing effect • Degradation

The employed excitation fluence directly influences the generated carrier densities. At low excitation fluence, trap states are still active, trap filling competes with charge extraction processes, resulting in inefficient charge transfer.[107,108] By gradually increasing the excitation fluence, the fast decay component in TRPL curves can be removed as the trap states being filled.[109] However, at high excitation fluence, high order recombination (e.g. bimolecular recombination and Auger recombination) become dominant, also inducing inefficient charge transfer.[108] Efficient charge transfer can only observed at intermediate excitation fluence (~ 1 sun irradiation).[108] In TA measurements, using higher excitation fluences can lead to charge accumulation in the CB and VB respectively (i.e. band filling effect).[110] These accumulated charge carriers can be beneficial for overcoming the potential barrier at CTL/perovskite interface and initiate subsequent charge transfer.[12]

The excitation wavelength determines (i) the penetration depth of light excitation (excited volume), and (ii) the excess energy of the photogenerated charge carriers. Long

wavelength excitation sources have a deep penetration depth, resulting in uniform excited charge carrier generation across the entirety of perovskite films (**Figure 8A** and **8B**). While a short excitation wavelength induces shallow penetration, limiting the excited volume to the sample surface. Carrier diffusion must be taken into consideration in such cases. On the other hand, short excitation wavelength, with higher energy, is beneficial for creating hot carriers to overcome either band position mismatch or interface potential barriers.[89]

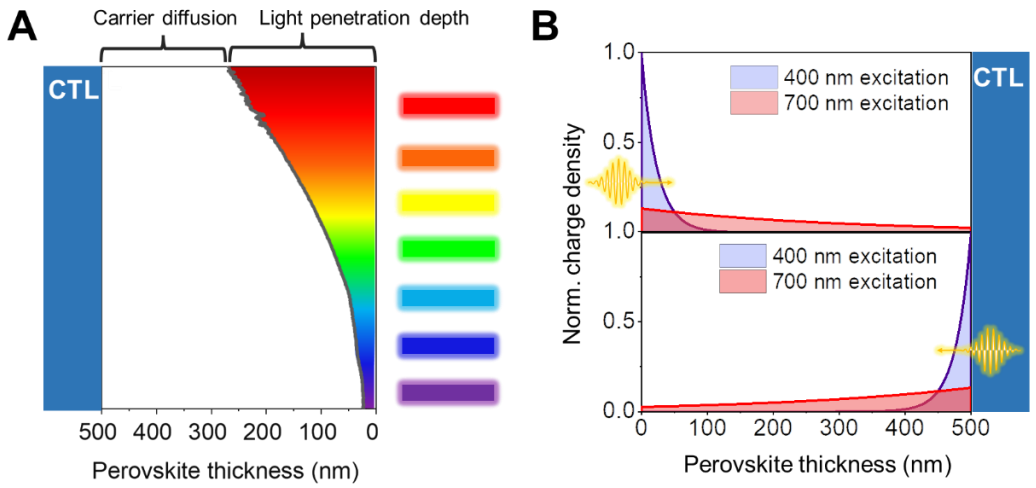

Figure 8. (A) Schematic diagram of light penetration conditions for a perovskite film (thickness: 500 nm) excited by different wavelength lasers. Light penetration depth: the depth at which the intensity of incident light decreases to 1/e of its initial value. (B) Distribution of excited charge density across a 500 nm thick perovskite film illuminated by 400 nm and 700 nm wavelength lasers: excitation occurs from the perovskite/air interface (top) and the perovskite/CTL interface (bottom). Reproduced from ref[35].

The direction in which light excitation is carried out also plays an important role. As presented in **Figure 8B**, front excitation (surface excitation) with short wavelength constrains the excited volume to the surface of the perovskite layers. These carriers have to diffuse to the CTL/perovskite interface first before being extracted. In the case of back excitation (CTL/perovskite interface), the excited carriers are formed in the vicinity of the CTL/perovskite interface and can be extracted directly. A fast decay in the early time scale of TRPL curve can be observed in the latter case, indicating charge transfer process is much faster than carrier diffusion.[35]

The employed repetition rate can also influence the kinetics of the recovery of the

excited state, especially in the case of TRPL which employs much higher repetition rate laser pulses compared to TA/TR. The recovery of trap states in perovskite layers can extend to the microsecond timescales.[111] When the time interval between the two exciting pulses is short (high repetition rate), de-trapping processes cannot fully occur before the next pulse arrives. The filled trap states from the last pulse can introduce "residual effects" for the next pulse and influence the observed decay kinetics.[36] Therefore, increasing the time interval between the two pulses (i.e. decreasing the repetition rate) to allow sufficient time for trap state depopulation is crucial.

As perovskites are sensitive to environmental conditions (e.g. light and atmosphere), these parameters need to be carefully controlled to avoid changes in layer quality and inadvertently influencing carrier dynamics. Light soaking can lead to PL brightening and prolong the PL lifetime.[112,113] For mixed-halide perovskites, light soaking can also cause phase segregation[114], leading to PL peak shifts[115], or even cause ion migration to the CTL/perovskite interface, altering band bending and ultimately influencing the charge transfer process itself.[93] Perovskite layers exposed to oxygen can exhibit similar PL brightening and prolonged excited state lifetime due to defect healing.[116,117] Small amount of water has similar curing effects[116], while high amounts of water can accelerate the degradation of perovskite.

1.3 The effect of electrical bias on charge transfer kinetics

Investigation of PSCs under working conditions can help us better understand, how electrical bias modulates charge separation[51], accumulation, and transfer[118]. Furthermore, the influence of phase and chemical changes in the bulk perovskite films or at the interfaces can be evaluated[119]. Direct measurement of full PSC stacks with or without applied external electric bias [120 121] gives insights on the charge carrier dynamics under working conditions, investigations of CTL/perovskite half-cell stack with transient spectroelectrochemistry allow us to separate the effect of ETLs and HTLs[118]. Due to the sensitivity of perovskites to polar solvents, careful solvent selection needs to be conducted before electrochemical measurements.[122,123] $MAPbI_3$ liquid junction solar cells were demonstrated more than 5

hours of stability under irradiation in dichloromethane (DCM)/Bu_4NPF_6 electrolyte with benzoquinone redox couple.[123] This long-term stability encourages further explorations of perovskite-based photoelectrodes. Electrochemistry coupled with in-situ UV-vis measurements can be used to probe the energy band positions of perovskite electrodes under selective electron injection conditions.[124] However, it was demonstrated that these systems suffer from irreversible decomposition during electron injection without the use of appropriate redox couples.[124] Similarly, hole injection was also shown to be able to cause gradual iodide expulsion from the perovskite lattice in a two-step process.[125] These results addressed the importance of establishing electrochemical stability windows before carrying out electrochemistry measurements on perovskite electrodes.[122]

Electrochemistry coupled with in-situ TA measurement is an effective method to reveal charge carrier dynamics of perovskite-based electrodes after photoexcitation (**Figure 9A**). With the perovskite layer exposed to laser irradiation, faster degradation of the layer can occur. This requires even more careful electrochemical stability potential window establishment, ensuring no decomposition of perovskite layer happening inside the probed potential window. Inside the stability window, transient spectroelectrochemistry was employed to investigate how trap state population and depopulation influence the carrier dynamic in CuI.[126] The applied negative bias was shown to fill the trap states in CuI and accelerate exciton dissociation. Such features of CuI may impact the performance of PCSs when CuI is included as HTL.[126] In another study, the charge carrier dynamics were compared at various applied potentials inside stability potential window between FTO/perovskite and mesoporous TiO_2/perovskite electrodes.[118] Results revealed that with TiO_2 ETL layer, one was able to modulate charge recombination and transfer by applying electrical bias (i. e. by varying the Fermi level of TiO_2). Positive bias was beneficial for accelerating electron transfer from perovskite to TiO_2 as electrons were depleted in TiO_2 in this condition (**Figure 9B**).[118] Negative potential had an exact opposite effect (**Figure 9B**).[118] These effects were, however, not seen in FTO/perovskite electrode (**Figure 9C**). Transient spectroelectrochemistry techniques can also be used to probe how electron injection process is influenced by the presence of certain ions in the electrolyte.[127] A delay of electron injection

from ITO to MoS_2 was observed in aqueous electrolyte which contains H^+, such as H_2SO_4 and Na_2SO_4. This means that a threshold density of electrons is required in ITO before injected into MoS_2. While in organic electrolyte (e.g., Bu_4NPF_6), such delay was not presented.[127] Furthermore, longer time scale time resolved spectroelectrochemistry is capable to probe the carrier dynamics of long lived photogenerated electrons and holes (100 ms - seconds) in photoelectrodes which can be used to drive useful chemical reactions, such as water splitting.[128,129] This can help us to understand how catalytic and surface passivation layers improve the performance of a photoelectrode. Both CoO_x (catalytic layer) and Ga_2O_3 (surface passivation layers) were demonstrated to lead to an electron depletion in the hematite photoelectrode with an applied bias. The achieved electron depletion reduced electron and hole recombination rate and thus left more long-lived holes at the surface of hematite for water oxidation.[129]

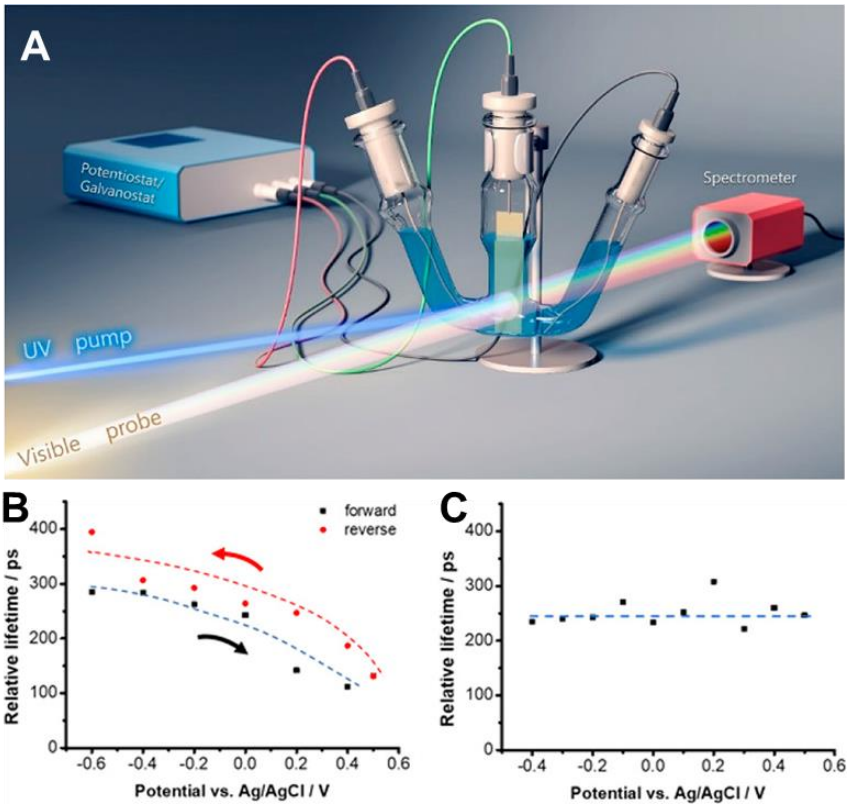

Figure 9. (A) A diagram of in-situ electrochemical and TA measurement setup. The relative lifetime of (B) TiO_2/perovskite and (C) TiO_2/perovskite influenced by the applied potential. Adapted from ref [118].

2. Aims

Throughout my research, I aimed to explore open scientific questions related to charge transfer at the CTL/perovskite interfaces:

- *How does the used analysis method influence the determined charge transfer rate?*
- *How can the dispersion of the determined charge transfer rate be rationalized?*
- *What is the influence of the band alignment at different single crystal TiO_2/perovskite interfaces on the electron transfer rate?*
- *How does the band position of perovskite films influence the hole transfer rate at NiO/perovskite interfaces?*
- *How does applied electrical bias influence the hole transfer process at NiO/perovskite interfaces and will the band alignment conditions at the interface affect it?*

As a first step, I explored different analysis methods and established an appropriate one for the explored systems (i.e. perovskite thin films) to determine the charge transfer rates. I used a 100 nm thick perovskite layer to minimize charge diffusion effect. Careful optimization and characterization were carried out to ensure that the perovskite layers properties were the same on different substrates. Then I coupled TA and TRPL to monitor electron extraction process from sub-picosecond to several hundreds of nanoseconds at TiO_2/perovskite interface. TiO_2 single crystals with different crystallographic orientation were used to explore the effect of band alignment on the kinetics of the electron extraction process. These substrates were chosen to ensure identical properties (e.g.,) apart from their CB positions. The band position tuning was also carried out from the perovskite side, by incorporating different amount of Br into the perovskite lattice. Three perovskite comopsitions with varying VB positions were deposited on ITO/NiO substrates. Hole transfer kinetics at these three NiO/perovskite samples were investigated by TA. Furthermore, Transient spectroelectrochemistry was carried out to explore the effect of external electric bias on the excited charge dynamics of these NiO/perovskite bilayers.

3. Materials and Methods

3.1 Materials

Chemicals used for the preparation of three composition of mixed perovskite ($FA_{0.83}Cs_{0.17}PbI_3$, $FA_{0.83}Cs_{0.17}Pb(I_{0.83}Br_{0.17})_3$, and $FA_{0.83}Cs_{0.17}Pb(I_{0.6}Br_{0.4})_3$) thin films

- lead (II) iodide (PbI_2, Alfa Aesar, ultra dry, 99.999% trace metals basis)
- lead (II) bromide ($PbBr_2$, Alfa Aesar, Puratronic®, 99.998% trace metals basis)
- formamidinium iodide (FAI, Greatcellsolar)
- cesium iodide (CsI, Thermo Scientific, 99.9% trace metals basis)
- dimethyl sulfoxide (DMSO, Sigma-Aldrich, anhydrous, >99.9%)
- n,n-dimethyl-formamide (DMF, Sigma-Aldrich, anhydrous, 99.8%)
- chlorobenzene (C_6H_5Cl, Sigma-Aldrich, anhydrous, 99.8%)

These chemicals were used without further purification.

Single crystal TiO_2

- single crystal TiO_2 substrates with (100) (rutile, Mateck, 1 cm x 1 cm x 1 mm)
- single crystal TiO_2 substrates with (110) (rutile, Mateck, 1 cm x 1 cm x 1 mm)
- single crystal TiO_2 substrates with (111) (rutile, Mateck, 1 cm x 1 cm x 1 mm)

Ultra flat glass used as an inert substrate

- Ultra-flat quartz coated glasses (Ossila)

Chemicals used for the preparation of NiO hole transfer layer

- nickel sulfate hexahydrate (SigmaAldrich, 99%)
- sodium acetate (anhydrous, Reanal, 99%)
- sodium sulfate (anhydrous, Alfa Aesar, 99%)

Chemicals used for the *preparation of the electrolyte*

- dichloromethane (DCM, Sigma Aldrich, anhydrous, ≥99.8%)
- tetrabutylammonium-hexafluorophosphate (Bu_4NPF_6, Sigma Aldrich, for

electrochemical analysis, ≥99.0%)

Dichloromethane was dried over 3Å molecular sieves overnight. Tetrabutylammonium-hexafluorophosphate was dried in a vacuum oven at 160 °C for more than 6 hours before use.

3.2 Thin film preparation methods

Preparation of $FA_{0.83}Cs_{0.17}Pb(I_{0.83}Br_{0.17})_3$ thin films

The precursor solutions were mixed by adding chemicals in a stoichiometric ratio (0.1713 g FAI, 0.0530 g CsI, 0.4121g PbI_2, and 0.1123 g $PbBr_2$) in 1 mL DMF and DMSO mixture solution (volume ratio 7:3) to form 1.0 M solution. Before spin coating, the solution was placed on a hot plate (70 °C) with continuous stirring for more than 1 hour. Then it was filtered with a 0.2 μm PTFE filter. To achieve a thin perovskite film (~100 nm thickness), the solution was diluted to a final 0.3 M solution with pure DMF.

Preparation of $FA_{0.83}Cs_{0.17}PbI_3$ and $FA_{0.83}Cs_{0.17}Pb(I_{0.6}Br_{0.4})_3$ thin films

0.3 M concentration solution was directly prepared by mixing 0.0159 g CsI, 0.0514 g FAI, and 0.1660 g PbI_2 for $FA_{0.83}Cs_{0.17}PbI_3$ and 0.0159 g CsI, 0.0793 g $PbBr_2$, 0.0514 g FAI, and 0.0664 g PbI_2 for $FA_{0.83}Cs_{0.17}Pb(I_{0.6}Br_{0.4})_3$ in DMF and DMSO mixture solution (volume ratio 91:9). Identical heating, stirring and filtering procedure was carried out as $FA_{0.83}Cs_{0.17}Pb(I_{0.83}Br_{0.17})_3$ before spin coating for both compositions.

Spin coating of the perovskite thin films

Before spin coating, the substrates were subjected to UV ozone and oxygen plasma treatment for 20 min. For the first step, the perovskite precursor solution (50 μl) was uniformly spread on the substrate. The spin coating procedure contains two steps. In the first step, 1000 rpm spinning speed was used for 10 s (1000 rpm acceleration), and 4000 rpm spinning speed was used for 30 s (1200 rpm acceleration) in the second step. To assist crystallization, 100 μl of chlorobenzene was dynamically dispensed on the substrate at the last 10 seconds of the spin coating procedure. Afterwards, the sample was placed on a hot plate for 2 min to form the

perovskite phase. For the $FA_{0.83}Cs_{0.17}Pb(I_{0.83}Br_{0.17})_3$ and $FA_{0.83}Cs_{0.17}Pb(I_{0.6}Br_{0.4})_3$, 80 ºC of annealing temperature was used, while 120 ºC was needed for $FA_{0.83}Cs_{0.17}PbI_3$, as the composition without Br incorporation requires higher temperature to achieve α-phase. All preparation procedures were conducted in a glove box with a nitrogen atmosphere (<0.1 ppm H_2O, <10 ppm O_2). The obtained perovskite layers were also stored under the same conditions.

Preparation of mesoporous NiO HTLs

Mesoporous NiO HTLs were synthesized by galvanostatic electrodeposition.[130] Before electrodeposition, the ITO substrates were cleaned by surfactant, and were then subjected to a three-steps of cleaning in deionized (DI) water, acetone and isopropanol (15 min for each sonication). The electrolyte was prepared by dissolving 0.13 M nickel sulfate, 0.13 M sodium acetate and 0.10 M sodium sulfate in DI water. The electrolyte was continuously stirred during the electrodeposition process. 0.5 mA cm^{-2} of current density was applied. The layer thickness was controlled by varying the passed charges(30 mC cm^{-2}, 60 mC cm^{-2} and 120 mC cm^{-2}). To obtain NiO, the as prepared films were annealed at 300 ºC for one hour in air.

3.3 Characterization techniques

3.3.1 Optical measurements

Steady state and time resolved photoluminescence (TRPL)

Steady state and time resolved photoluminescence (TRPL) measurements were performed by Horiba DeltaPro with a 467 nm laser source. The applied laser pulse frequency during measurement was 500 kHz. This setup uses time-correlated single-photon counting (TCSPC) to record the TRPL decay curve. The mechanism of TCSPC is illustrated in **Figure 10**. A pulsed laser is used to excite the semiconductor material (sample). Upon excitation, the sample emit one photon. An electronic timer is designed to record the arrival time (Δt) of the emitted photon (**Figure 10A**). Importantly, only one photon can be counted in each cycle. By repeatedly recording the arrival time of the single photons, a PL decay histogram can be

recorded (**Figure 10B**). Due to the limitation of the detector and the electronics, there's an instrument "dead time" (usually in the range of several to tens of nanoseconds). This means that two consecutive photons should not be closer than this limitation. Otherwise, the obtained PL decay curve will be distorted. Therefore, the excitation/detection rate is always carefully optimized and kept lower than ~ 0.01 of the maximum detection rate. Additionally, the interval between two consecutive laser pulses should be kept 5 times longer than the PL decay time of the respective sample to make sure the detected photon is from the corresponding excitation pulse. When the PL decay time of the sample is similar to the instrument response function (IRF) of the detector and electronics, IRF correction should be carefully carried out to determine an accurate PL decay trend.

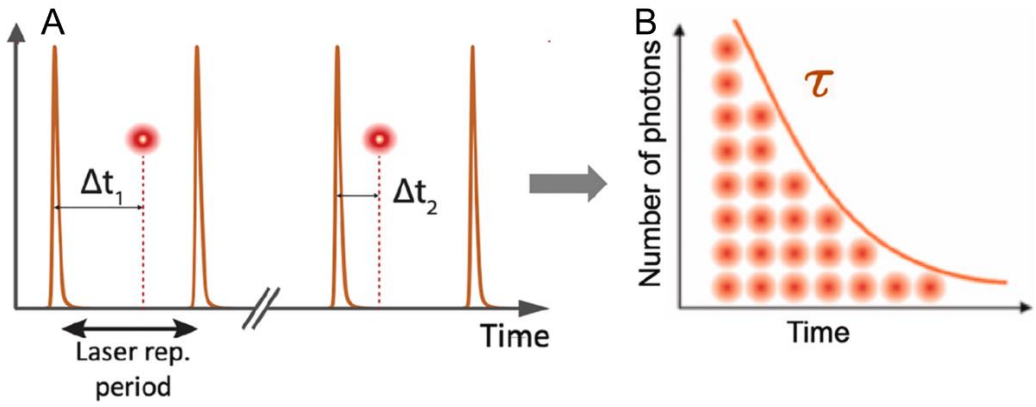

Figure 10. TCSPC working principle. (A) An illustration of excitation laser pulses and the arrival time of the detected single photon. The process of detection of a single photon is carried out repeatedly. (B) An illustration of photoluminescence decay histogram over time created from TCSPC method. Adapted from Ref[131].

Transient absorption spectroscopy (TA)

Transient absorption spectroscopy (TA) employs short laser pulses (6 fs in our case) and can resolute processes in the sub-picoseconds time range. TA is a pump-probe technique, which employs a pump pulse to excite the sample and a probe pulse to monitor the change in absorption of the sample before and after excitation (**Figure 11**). The pump and probe pulses are from the same laser source (fundamental beam, 1030 nm in our case) but split into two routes. The probe passes through a crystal, such as CaF_2, or DI water to generate a white light continuum. A delay stage, which is capable to accurately introduce a small distance variation between the two beam paths, is used to vary the arrival time of probe light relative

to pump pulse. In this way, we can track the kinetics of the absorption change of the sample after excitation. The length of the delay stage determines the probing time window of a TA set-up (1600 picosecond in our case). The probe beam needs to be spatially overlapped with the excited volume of the sample and smaller sized than the pump beam. Furthermore, it must not induce any additional changes to the sample. To probe the absorption without pump excitation, a mechanical chopper is introduced to remove certain pump pulses. The data collected equals the difference between the absorption with both the pump and probe and with only the probe:

$$\Delta A = A_{pumb+probe} - A_{probe} \quad (9)$$

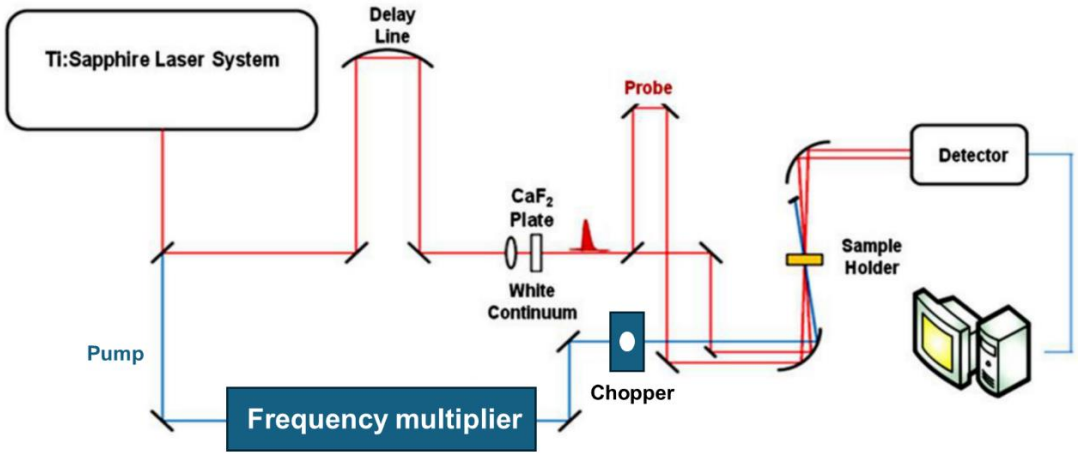

Figure 11. A scheme of typical TA set-up. Adapted from Ref [132].

Interpreting TA data is complicated as it can include signals from several different processes (**Figure 12**). With the excitation pulse, the transition from the ground state to excited state is achieved (**Figure 12A**), leading to less population in the ground state. This results in a smaller absorption signal in the wavelength of ground state absorption, thus a negative ground state bleaching (GSB) signal (**Figure 12B**) is observed. This signal decays over time indicating the recovery of the ground state. The probe pulse can also induce stimulated emission (SE) resulting in the emission of additional photons. This also leads to a negative signal, as the measured absorption becomes smaller with the emitted photons ($A_{pump+probe} < A_{probe}$). Similarly to the PL signal, a Stokes shift is present between the SE signal relative to GSB (**Figure 12B**). Induced absorption (IA) is the process when the excited

states absorb the photons in the probe pulse and are excited to an even higher energy level (if available). This leads to a positive signal as the photons in the probe pulse are absorbed and thus a higher $A_{pump+probe}$ is recorded (**Figure 12B**). Global analysis can be used to disentangle these complex processes, which fits the entire dataset to a kinetic model by assuming that the same kinetic processes govern the dynamics across all wavelengths. From this analysis, decay-associated spectra (DAS) can be obtained, representing the amplitude contributions of each exponential decay component across different wavelengths. DAS helps researchers to link specific spectral features to their corresponding kinetic processes.

Additionally, the high energy tail of the GSB signal in the early time scales (< 1ps) can be used to evaluate the relaxation (cooling) of hot carriers. Maxwell–Boltzmann distribution function can be used to fit the tail to extract the hot electron temperature:

$$\Delta A(E) = A_0 e^{-(E-E_f)/k_B T_c} \quad (10)$$

, where E_f is the quasi-Fermi level energy, and k_B is the Boltzmann constant.

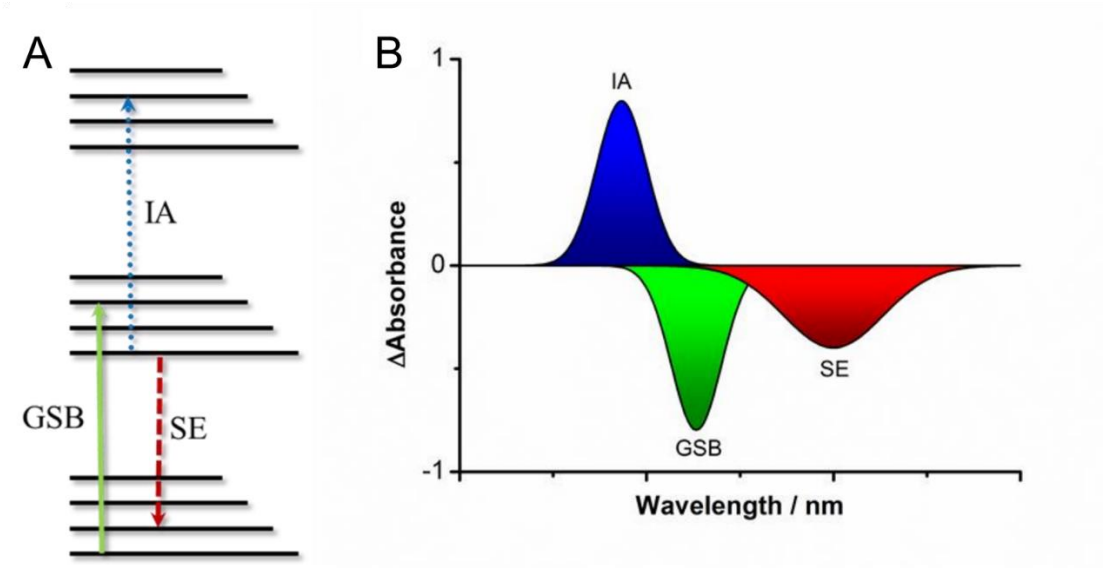

Figure 12. (A) Possible processes during TA measurement in a sample: ground state bleaching (GSB), induced absorption (IA) and stimulated emission (SE). (B) The corresponding typical spectra signals of the processes.

To evaluate the results more accurately, the incident pump fluence (P) can be converted into the excited carrier density (n) using the following equation:

$$n = \frac{P\lambda}{hcd}(1 - 10^{-A}) \quad (11)$$

Where λ is the wavelength of the pump pulse, h is plank constant, c is speed of light, d is the layer thickness of the sample, and A is the absorbance of the sample at the excitation wavelength.

UV-vis absorption spectroscopy

Steady state UV-vis absorption spectra of the prepared perovskite layers on various substrates were measured by an Agilent 8453 UV–vis spectrophotometer. All measurements were carried out in a sealed cell under a nitrogen atmosphere. By performing Tauc analysis on the obtained UV-vis absorption spectra, band gap of the material can be determined. For a given material, the absorption coefficient (α) and photon energy (hν) follow:

$$(\alpha h\upsilon)^n = A(h\upsilon - E_g) \quad (12)$$

where n is determined by transition type of the material. When the material has an indirect bandgap, $n = \frac{1}{2}$. When the material has a direct bandgap, $n = 2$. A is material dependent constant and E_g is the bandgap of the material.

Contact potential difference (CPD)

Contact potential difference (CPD) measurements were conducted by KP Technology APS04. This technique was used to study the Fermi level and work function of a material. A vibrating gold tip, which has a constant Fermi level of −4.78 eV, is used to form a capacitor with a grounded sample for contactless measurement of the potential difference between the two. The Fermi level of the sample can be determined by the following equation:

$$E_f(\text{sample}) = E_f(\text{gold tip}) + \text{CPD} \quad (13)$$

Surface photovoltage spectroscopy (SPS)

Surface photovoltage spectroscopy (SPS) measurements were also conducted by KP Technology APS04. A monochromatic light illumination, with wavelength scanning from 1000 to 400 nm, was used during the measurement. When the illuminated photon energy exceeded the bandgap of the sample, electrons and holes were generated. These photo-generated charge carriers can be separated, with electrons driven towards one direction and

holes to another, according to the internal electric fields of the sample. This can cause changes in surface potential of the sample, which is the origin of surface photovoltage. Surface photovoltage can be determined by taking the difference between the recorded CPD values in the dark and under illumination. This technique can reveal the electronic bandgap energy of the examined material, which is at the photon energy where surface photovoltage starts to increase. The surface photovoltage can also indicate how the photo-generated electrons and holes are distributed. Additionally, by investigating the kinetics of surface photovoltage signal the surface states influencing the charge dynamics (e.g. trapping and recombination) can be revealed.

Ambient-pressure photoemission spectroscopy (APS)

Ambient-pressure photoemission spectroscopy (APS) was conducted by the same KP Technology APS04 instrument, but with a stationary gold tip. The grounded semiconductor sample was illuminated by a variable deep UV light source to liberate the electrons from the VB. The liberated electrons interact with the gas molecules in the atmosphere and form a cloud of negative ions. These negative ions have a much longer mean free path than the electrons. With an applied voltage, they can be collected by the sensor as a photocurrent. The onset photon energy of illuminated UV light can be determined as the VB position of the sample. However, VB signals are usually week due to photoelectrons scattering with ambient gas. Cube root of photoemission is usually plotted to enhance the weak features.

Ultraviolet photoelectron spectroscopy (UPS)

Ultraviolet photoelectron spectroscopy (UPS) was carried out by a He (I) photon source with an energy of 21.22 eV. Due to the low energy of applied photons, UPS is sensitive to the surface of the sample. This technique is conducted in ultra-high vacuum condition, where a 10 V of electric bias was applied to collect secondary electrons. The kinetic energy of collected electrons will be recorded to determine the Fermi level and the VB position of the sample.

3.3.2 Spectroelectrochemistry measurements

Spectroelectrochemistry

Spectroelectrochemistry is a powerful tool to track electrochemistry-induced processes that are accompanied by a color change. This color change can occur both in the electrolyte and on the surface of a transparent electrode. Simultaneously performing cyclic voltammetry (CV) and monitoring the sample absorption can be used to investigate the stability window of a perovskite electrode. A sealed three-electrode cell was used, with a perovskite layer as the working electrode, Pt wire as the counter electrode and a Ag/AgCl wire as a pseudo-reference electrode. The used electrolyte was 0.01 M Bu_4NPF_6 DCM solution. CV was carried out by a Biologic VMP-300 potentiostat/galvanostat. Absorption measurement was carried out by an Agilent 8453 UV–visible spectrophotometer.

In-situ transient spectroelectrochemistry

The same three-electrode system and electrolyte were used for the in situ transient spectroelectrochemistry measurements. Potentiostatic measurements, carried out by a Metrohm Autolab PGSTAT302 type potentiostat–galvanostat, was used to tune the Fermi level of NiO beneath the perovskite layer.

3.3.3 Materials characterization

Atomic force microscopy (AFM)

Atomic force microscopy (AFM) images were recorded using a NT-MDT Solver AFM microscope to analyze the surface roughness of the single crystal TiO_2 substrates.

Scanning electron microscopic (SEM)

Scanning electron microscopic (SEM) images were measured by a FEI Helios NanoLab DualBeam instrument to record the morphology and grain size distribution of perovskite layers.

X-ray diffraction (XRD)

X-ray diffraction (XRD) patterns were measured with a Bruker D8 Advance instrument to analyze the phase purity of the samples. Cu Kα (λ = 1.5418 Å) was used for X-ray source.

The measurement angle ranged from 10-80° for single crystal TiO_2 and 10-46° for perovskite layers. The scan speed was set to be 1° min^{-1}.

4. Results and discussion

4.1 Dispersion in the determined charge transfer rate constant

4.1.1 The role of the evaluation method

As discussed in Chapter 1, multiple different factors can contribute to the dispersion in the determined charge transfer lifetime through the CTL/perovskite interface. Different evaluation methods are available to interpret time-resolved data (TAS and TRPL) and extract the charge transfer rate constant, however, their role in the observed dispersion has not yet been explored. Therefore, we carried out different fitting and evaluation protocols on the same dataset, where the relaxation of the excited state of a TiO_2 (110)/perovskite sample was measured with TRPL and TA. In all cases the goodness of the fit was evaluated by the residual traces.

For the TRPL measurements, we adopted four different evaluation methods that follow widely used literature examples. In the first method, a biexponential function was used to fit the TRPL decay curves of both TiO_2 (110)/perovskite ($FA_{0.83}Cs_{0.17}Pb(I_{0.83}Br_{0.17})_3$) and glass/perovskite ($FA_{0.83}Cs_{0.17}Pb(I_{0.83}Br_{0.17})_3$) samples. $FA_{0.83}Cs_{0.17}Pb(I_{0.83}Br_{0.17})_3$ will be referred to as perovskite in the subsequent discussion. The glass/perovskite sample was included as a reference sample, where no charge transfer was expected (insulating glass substrate). From these measurements, the charge transfer equation (Equation 3) can be used to extract the charge transfer rate constant.[81] In the second method, the short lifetime component in the biexponential fitting was directly attributed to charge transfer lifetime.[98] The third method adopted a triexponential fitting function to the decay traces of the TiO_2 (110)/perovskite sample. Similarly, the shortest lifetime was used to determine the charge transfer lifetime.[133] A stretched exponential function was used in the fourth method to account for carrier diffusion processes within the perovskite films. [134] Similarly, glass/perovskite, where there was no charge transfer, was used as a reference sample to get starting fitting parameters. The parameter β includes spatial inhomogeneities in the perovskite films. An additional short lifetime component was added in TiO_2 (110)/perovskite sample, which was attributed to charge transfer lifetime.[134] The TRPL decay curves, together with the results of the different fitting protocols and residual curves, are shown in **Figure**

13. The residual curves can indicate whether further components are necessary to accurately describe the decay traces, which are rarely shown. All the fitting parameters are shown in Appendix **Table A1**. For the same set of TRPL decay curves, just by varying the applied evaluation method, a charge transfer lifetime between 3.4 to 26.3 ns was determined (**Table 4**), indicating a significant influence of the applied analysis method on the final extracted charge transfer lifetime.

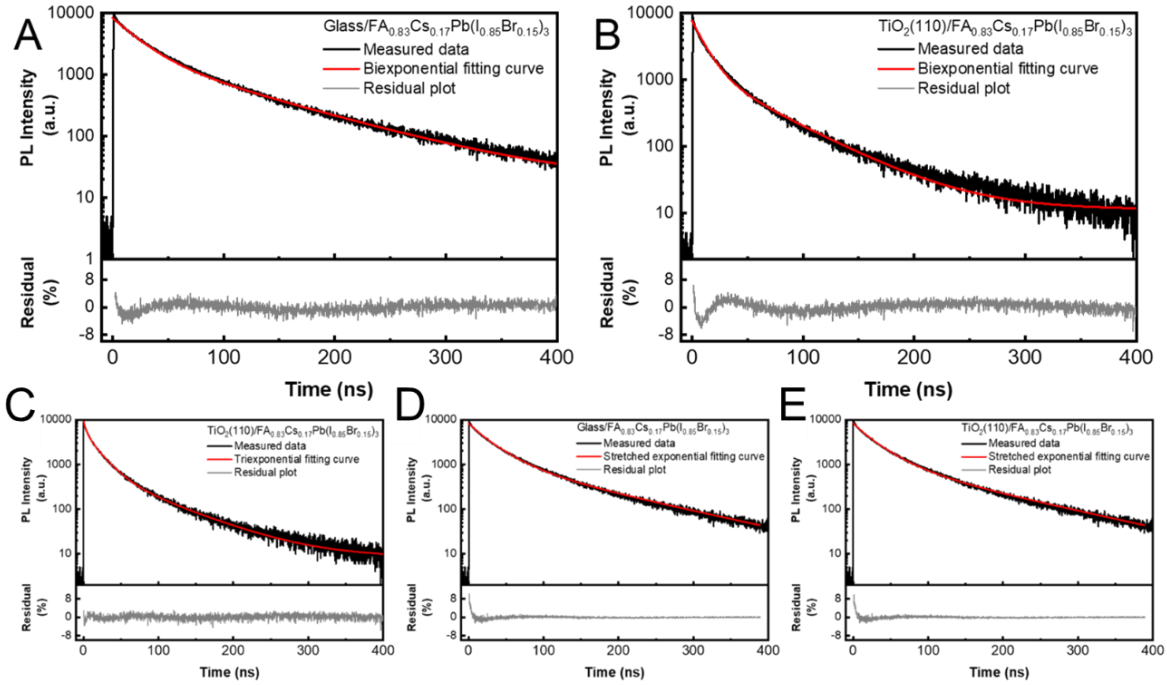

Figure 13. Representative TRPL decay curves, together with the fitting curves and the residuals. Biexponential fitting for (A) glass/perovskite ($FA_{0.83}Cs_{0.17}Pb(I_{0.83}Br_{0.17})_3$) and (B) TiO_2 (110)/perovskite ($FA_{0.83}Cs_{0.17}Pb(I_{0.83}Br_{0.17})_3$), triexponential fitting for (C) TiO_2 (110)/perovskite ($FA_{0.83}Cs_{0.17}Pb(I_{0.83}Br_{0.17})_3$), stretched exponential fitting for (D) glass/perovskite ($FA_{0.83}Cs_{0.17}Pb(I_{0.83}Br_{0.17})_3$) and (E) TiO_2 (110)/perovskite ($FA_{0.83}Cs_{0.17}Pb(I_{0.83}Br_{0.17})_3$). The excitation wavelength was 467 nm, and the decay traces were monitored at 750 nm. Extended data from ref[35].

Table 4. Summary of TRPL decay curve fitting and evaluation methods, and the respective extracted charge transfer lifetime, rate constant, and literature example for the method. Reproduced from ref[35]

Fitting protocol	τ_{CT} (ns)	Rate Constant (10^7 s^{-1})	Reference

Biexponential fitting for glass/perovskite and TiO_2 (110)/perovskite TRPL decay curves. Solving the charge transfer equation.	26.3	3.8	[81]
Biexponential fitting for TiO_2 (110)/perovskite TRPL decay curve. Attributing the short lifetime to charge transfer.	11.2	8.9	[98]
Triexponential fitting for TiO_2 (110)/perovskite TRPL decay curve. Attributing the shortest lifetime to charge transfer.	3.4	29.4	[133]
Using a stretched exponential function to describe carrier diffusion processes within the perovskite films. Attributing the shortest lifetime to charge transfer.	11.6	8.6	[134]

For TA measurements, five commonly used data evaluation approaches to extract the charge transfer lifetime from the same set of data. Similar as in TRPL evaluation, charge transfer equation method[19], shortest lifetime component extraction method from biexponential fitting [135], triexponential fitting [136] and stretched exponential fitting were applied [86]. Except for these four methods, the long lifetime component was attributed to charge transfer lifetime in the fifth method following one literature. The TA data together with various fitting results are shown in **Figure 14**. All the fitting parameters are shown in Appendix **Table A2**. For the same set of TA data, just by varying the applied evaluation methods, a dispersion of charge transfer lifetime from 0.2 to 14.1 ns can be observed (**Table 5**).

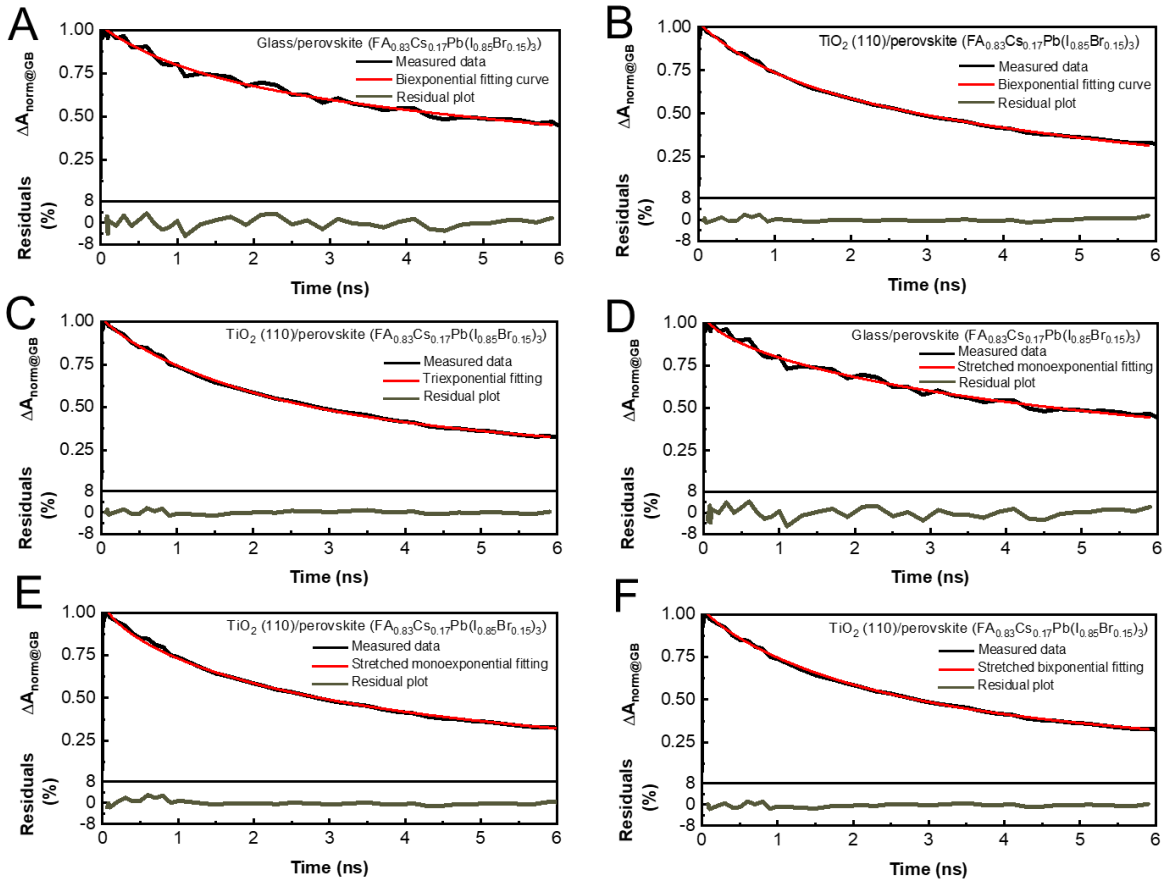

Figure 14. Representative TA decay traces graphed together with the fitting curves and the residuals. Biexponential fitting of (A) glass/perovskite ($FA_{0.83}Cs_{0.17}Pb(I_{0.83}Br_{0.17})_3$) and (B) TiO_2 (110)/perovskite ($FA_{0.83}Cs_{0.17}Pb(I_{0.83}Br_{0.17})_3$). (C) Triexponential fitting of TiO_2 (110)/perovskite ($FA_{0.83}Cs_{0.17}Pb(I_{0.83}Br_{0.17})_3$). Stretched mono-exponential fitting of (D) glass/perovskite ($FA_{0.83}Cs_{0.17}Pb(I_{0.83}Br_{0.17})_3$) and (E) TiO_2 (110)/perovskite ($FA_{0.83}Cs_{0.17}Pb(I_{0.83}Br_{0.17})_3$). (F) stretched biexponential fitting of TiO_2 (110)/perovskite ($FA_{0.83}Cs_{0.17}Pb(I_{0.83}Br_{0.17})_3$). The excitation wavelength was at 600 nm, with a fluence of 5.7 μJ cm^{-2}. The TA decay traces were extracted at 725 nm. Extended data from ref[35].

Table 5. Summary of TA data fitting and evaluation methods, and the respective extracted charge transfer lifetime, rate constant and literature example for the data treatment. Reproduced from ref[35].

Fitting protocol	τ_{CT} ns	Rate Constant (10^9 s^{-1})	Reference
Biexponential fitting for glass/perovskite and TiO_2 (110)/perovskite TA decay traces and solving the charge transfer equation.	14.1	0.07	[19]
Biexponential fitting for TiO_2 (110)/perovskite TA decay traces. Attributing the short lifetime to charge transfer.	0.9	1.11	[135]

Biexponential fitting for TiO_2 (110)/perovskite TA decay traces. Attributing the long lifetime to charge transfer.	6.4	0.16	[137]
Triexponential fitting for TiO_2 (110)/perovskite TA decay traces. Attributing the shortest lifetime to charge transfer.	0.2	5.00	[136]
Using a stretched exponential function to describe carrier diffusion processes within the perovskite films. Attributing the shortest lifetime to charge transfer.	1.9	0.53	[86]

We can identify two major factors that contribute to the observed dispersion: (1) the number of exponents used for the fitting and (2) the arbitrary assignment of the components to charge transfer. Therefore, rigorous validation of evaluation methods, such as a physical charge transfer model, is essential to ensure that each component is associated with a physical process. Also, careful background and control measurements (e.g., the inclusion glass/perovskite reference sample) need to be considered to evaluate the contribution of trap states to the decay kinetics.

4.1.2 Proposed measurement protocols to minimize the dispersion

We can conclude that the estimate of charge transfer lifetime at the CTL/perovskite interface from both TRPL and TA measurements depends on various factors: (1) the detection limit of the measurement technique, (2) the perovskite sample properties, which includes layer thickness, trap state densities, back contact conditions, (3) the measurement parameters, including geometry of excitation, excitation wavelength, fluence, and measurement atmosphere, (4) the evaluation method employed to interpret the transient decay traces. This has resulted in a wide range of charge transfer rate constants being reported in the literature. Unfortunately, standardizing the measurement protocols globally is nearly impossible. Therefore, it is important to keep in mind that there are limitations of transient spectroscopy measurements and evaluation methods. To minimize the dispersion and to obtain comparable results, a list of protocols was recommended for the researchers in the field to adopt.

A. Clearly describe the sample preparation, including composition, grain size distribution, and the thickness of each layer (including interlayers/passivation layers).
B. Provide excitation conditions including geometry, fluence, excitation wavelength, and repetition rate.
C. Include the absorbance of the sample at the excitation wavelength and indicate whether the excitation is homogeneous throughout the sample.
D. A broader model to account for ultrafast (fs-ns) as well as slow (ns-μs) components responsible for charge transfer should be adopted and not just tailored to a specific detection time window.
E. A physical charge transfer model needs to be established first before attempting to analyze the kinetic traces. If possible, the reasons for ruling out other models need to be discussed.
F. While model is unsure, the average lifetime, which is model independent, can be analyzed to showcase charge transfer.[35]

4.2 Effect of single-crystal TiO_2 (SC TiO_2)/perovskite band alignment on the kinetics of electron transfer

To resolve the controversy regarding whether a large or small energy offset enhances charge transfer efficiency, we employ SC TiO_2 with three different facets, which display varying conduction band positions while retaining similar surface properties. This allows us to attribute the variations in charge transfer kinetics at the TiO_2/perovskite interface solely to differences in band alignment conditions.

4.2.1 Characterization of the perovskite layer properties

Following the protocols listed above, we first carefully characterized the properties of both the SC TiO_2 substrates and the perovskite layers ($FA_{0.83}Cs_{0.17}Pb(I_{0.83}Br_{0.17})_3$). Three different SC TiO_2 orientations were used. XRD measurements revealed that they were all rutile phase of (100), (110) and (111) orientation (**Figure 15)**.[138,139]

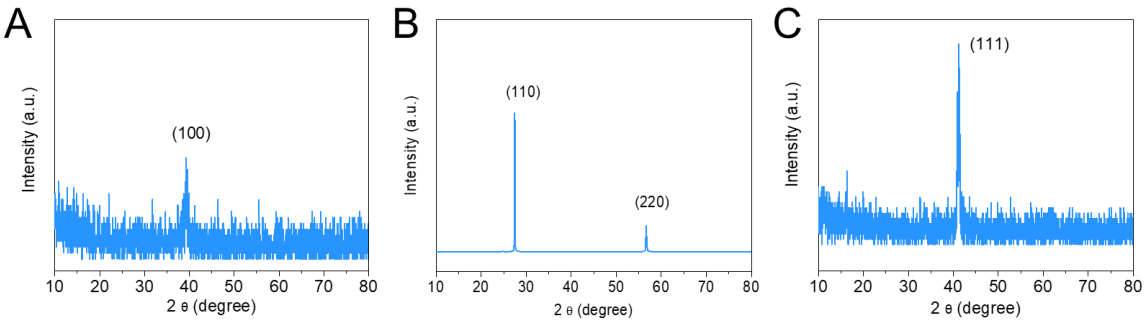

Figure 15. XRD results of the rutile SC TiO_2 substrates with three different orientations. (A) TiO_2 (100), (B) TiO_2 (110), and (C) TiO_2 (111). Reproduced from ref [12].

AFM measurements (**Figure 16**) were carried out to confirm the surface quality of SC substrates. A surface roughness of 0.1 nm for TiO_2 (100), 0.3 nm for TiO_2 (110), and 0.3 nm for TiO_2 (111) was determined, revealing smooth surfaces. These surfaces were used as the substrates for the perovskite thin films.

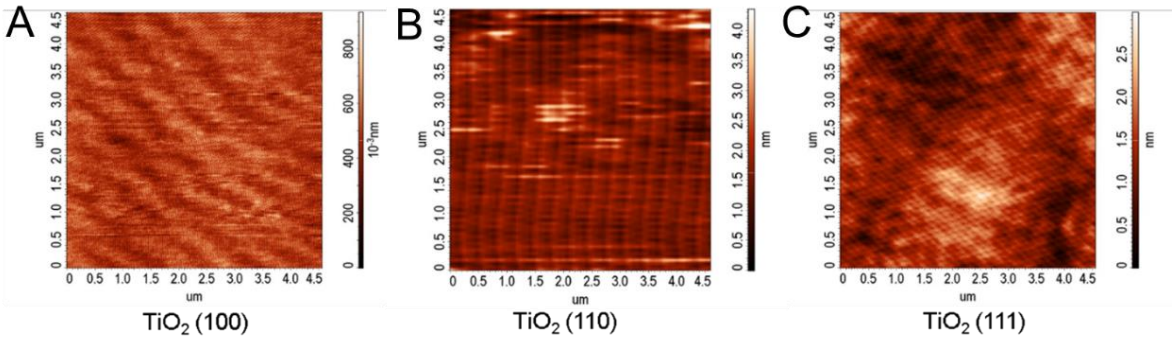

Figure 16. AFM images of the three single crystal TiO_2 substrates with different orientations. (A) TiO_2 (100), (B) TiO_2 (110) and (C) TiO_2 (111). Average surface roughness was revealed to be 0.1 nm for TiO_2 (100), 0.3 nm for TiO_2 (110), and 0.3 nm for TiO_2 (111). Reproduced from ref [12].

In a subsequent step, $FA_{0.83}Cs_{0.17}Pb(I_{0.83}Br_{0.17})_3$ thin films were spin-coated on the SC TiO_2 and also glass substrates (reference without charge transfer). Considering the sensitivity of perovskite layers to the employed substrates, ultra-flat quartz-coated glass was used. To achieve the same absorbance spectra of the perovskite layers on all substrates, the deposition process underwent thorough optimization (**Figure 17**). As we were aiming for thin (~ 100 nm thick) films to avoid the influence from carrier diffusion process, the optimization process turned out to be challenging. The optimized preparation procedures of the perovskite layers are described in the experimental part. In brief, the annealing condition is of vital

importance. The optimization included adjusting the employed annealing temperature, duration, and the number of steps to ensure that the desired perovskite phase was formed with no other impurity phases. We found that the composition of the used solution, such as the DMF/DMSO ratio, largely influenced the achieved phase composition and morphology of perovskite layers. Additionally, attention should also be given to the used antisolvent, such as its nature, volume, and the treatment time.

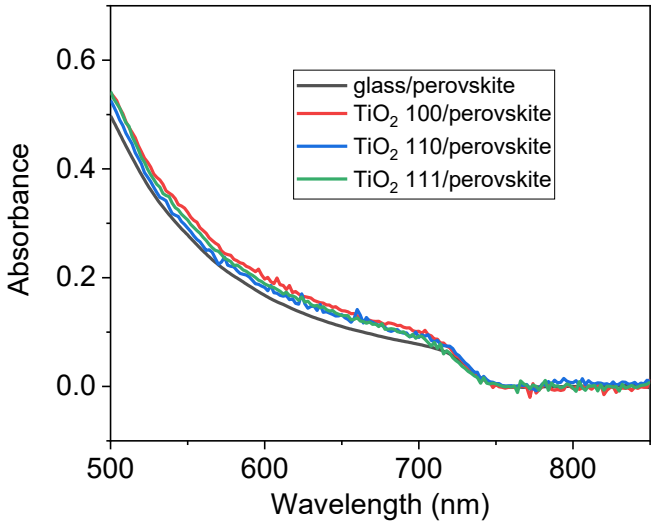

Figure 17. UV-vis spectra of perovskite layers prepared on glass and SC TiO_2 substrates. Reproduced from ref[12].

XRD measurements were carried out to examine the phase purity of the perovskite layers on all substrates. After the thorough optimization, the results (**Figure 18**) show that the desired perovskite phase was formed on all substrates. In alignment with previous reports, the position of diffraction peaks of $FA_{0.83}Cs_{0.17}Pb(I_{0.83}Br_{0.17})_3$[140] were slightly shifted in comparison to $FAPbI_3$. This is caused by the lattice shrinking due to the incorporation of Cs^+ and Br^- into the perovskite lattice.[141] No impurity phases were identified, revealing good layer quality of the prepared perovskite layers (additional diffraction peaks are from the TiO_2 substrates and the Al sample holder).

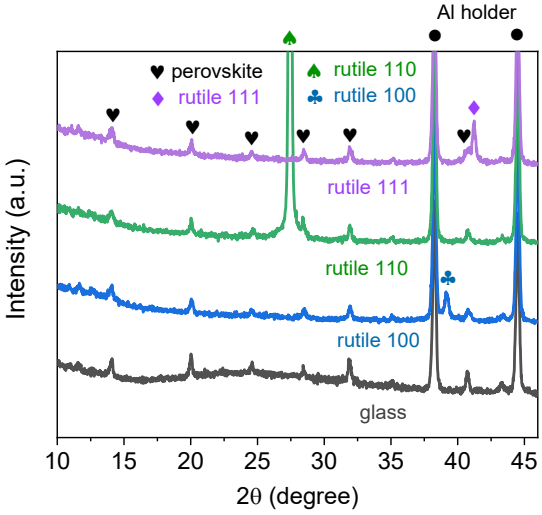

Figure 18. XRD results of perovskite layers prepared on glass and SC TiO_2 substrates. Reproduced from ref[12].

Ellipsometry measurements were carried out to determine the thickness of the prepared perovskite thin films (**Table 6**). The glass/perovskite sample has a layer thickness of 110 nm. Perovskite layers prepared on SC TiO_2 substrates all have thicknesses of 90 nm. Ellipsometry results also revealed a surface roughness of around 2 nm for perovskite layers on all substrates. This confirms that the prepared perovskite films with the optimized deposition protocol have a similar layer thickness and smooth surfaces on the different substrates.

Table 6. The thickness and surface roughness of perovskite films on glass and SC TiO_2 substrates revealed by ellipsometry results. Reproduced from ref[12].

Substrate	Thickness (nm)	Surface roughness (nm)
glass	111	3.5
TiO_2 (100)	86	2
TiO_2 (110)	87	2
TiO_2 (111)	89	2

SEM images showed similar morphology and grain size distribution of the perovskite layers on different substrates (**Figure 19**). An average grain size of 60 nm was identified for perovskite layers on all substrates. These results indicate that all parameters that can influence charge carrier dynamics, including layer thickness, absorbance, phase purity,

morphology and grain size, were carefully controlled.

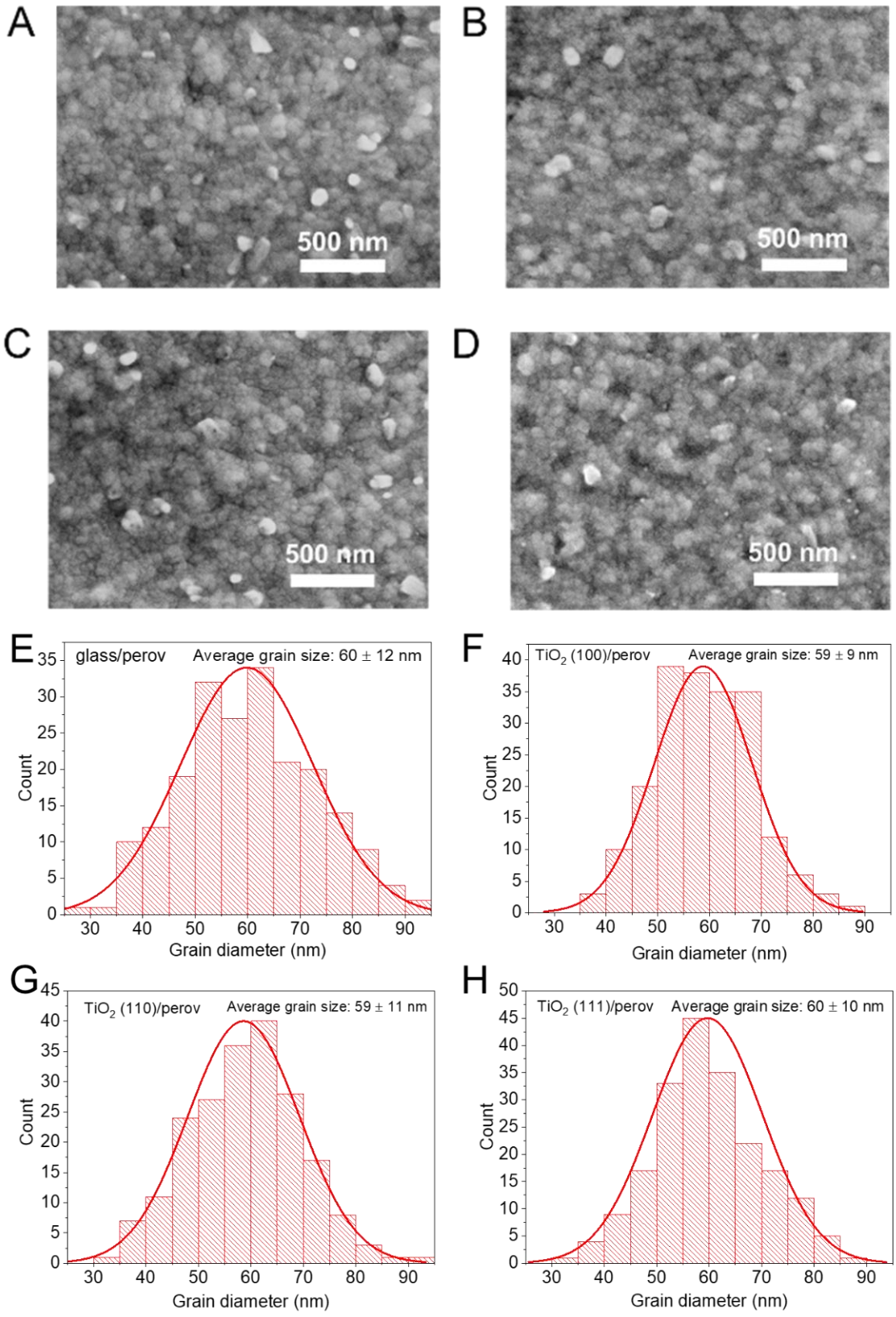

Figure 19. SEM images of perovskite films on (A) glass, (B) TiO_2 (100), (C) TiO_2 (110), and (D) TiO_2 (111) substrates. Grain size distribution of the perovskite layers on (E) glass, (F) TiO_2 (100),

(G) TiO_2 (110), and (H) TiO_2 (111) substrates. Reproduced from ref [12].

4.2.2 Band alignment at the SC TiO_2/perovskite interface

UPS measurements were employed to reveal the VB positions of TiO_2 single crystals. These measurements indicate a deep VB position for TiO_2 (100) and (111) facets (−7.8 eV vs. vacuum), and a shallower VB position for the TiO_2 (110) facet (−7.2 eV vs. vacuum) (**Figure 20** and **Table 7**).

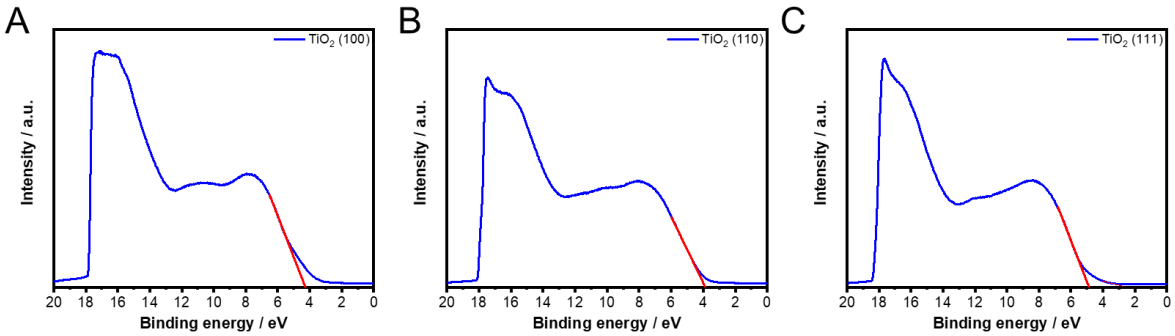

Figure 20. UPS results of single crystal TiO_2 (100) (A), TiO_2 (110) (B), and TiO_2 (111) (C). Reproduced from ref [12].

By performing Tauc analysis on the UV-vis spectra of the TiO_2 single crystals, their respective band gaps can be determined. These substrates were shown to have a direct bandgap of 3.0 eV for all three orientations (**Figure 21**). Then the CB position of these TiO_2 single crystals can be calculated accordingly, the results are shown in **Table 7**. Similarly, a deeper CB position was revealed for TiO_2 (100) and (111) facets (−4.8 eV vs. vacuum). TiO_2 (110) facet was shown to have a shallower CB position (−7.2 eV vs. vacuum).

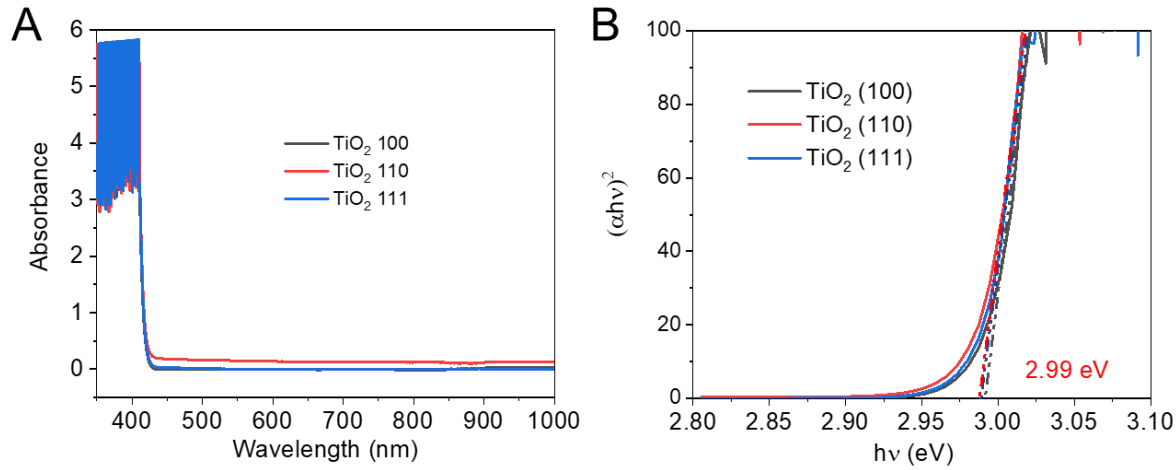

Figure 21. UV vis spectra (A) and Tauc plots for a direct transition (B) of SC TiO_2 substrates.

Reproduced from ref[12].

Table 7. VB and CB positions of SC TiO_2 substrates revealed by UPS measurements and Tauc analysis of the UV-vis spectra. Reproduced from ref[12].

Crystal orientation	E_{sec} / eV	E_{VB} / eV	E_{VB} vs. vacuum / eV	E_{CB} vs. vacuum / eV
(100)	17.81	4.37	−7.78	−4.78
(110)	18.04	3.97	−7.15	−4.15
(111)	18.36	4.94	−7.80	−4.80

APS measurements were employed to investigate the VB position of perovskite layers on the various substrates. The VB position of perovskite layers on all substrates was determined to be around −5.5 eV (**Figure 22**). This aligns well with the values reported in previous studies.[142] Similarly, we carried out Tauc analysis (**Figure 23**) of the UV-vis spectra of the perovskite layers to evaluate the bandgap and to subsequently calculate the CB position. A direct bandgap of 1.7 eV was determined in all cases. Consequently, the CB position of perovskite layers was found to be −3.8 eV in all cases.

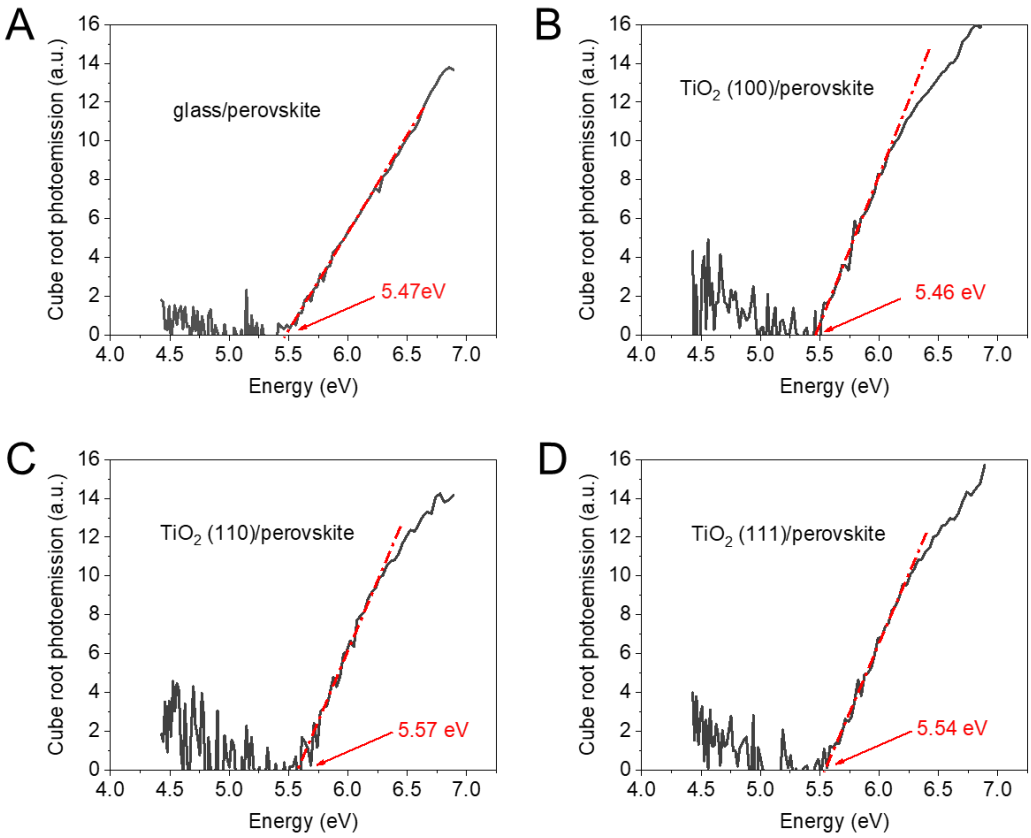

Figure 22. APS results of perovskite films on glass (A), TiO_2 (100) (B), TiO_2 (110) (C), and TiO_2 (111) (D). Reproduced from ref [12].

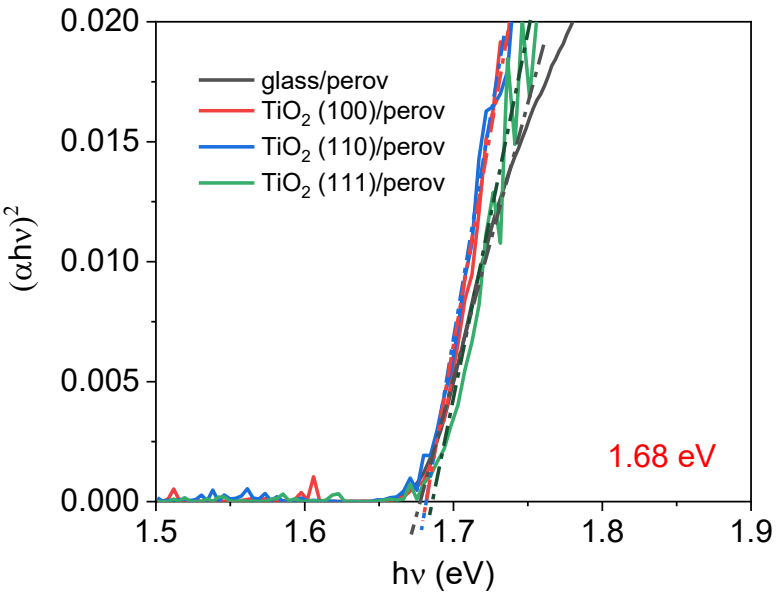

Figure 23. Tauc plots were determined for a direct transition of perovskite layers on glass and SC TiO_2 substrates. Reproduced from ref [12].

According to the obtained band positions of the SC TiO_2 and perovskite layers, the band alignment at the CTL/LHP can be visualized (**Figure 24**). The electron extraction process from the perovskite thin film will be influenced by the CB offset at TiO_2/perovskite interface. A larger CB offset (ΔE = 1.0) at the TiO_2 (100)/perovskite and TiO_2 (111)/perovskite interfaces can be observed compared to the offset at the TiO_2 (110)/perovskite interface (ΔE = 0.4). A larger CB offset can result in a greater thermodynamic driving force for the electron transfer in the two specific TiO_2 orientations.

We also employed CPD measurements to obtain the Fermi level of perovskite layers and the SC TiO_2 substrates. Fermi levels of -5.5 ± 0.06, -5.2 ± 0.07, and -5.4 ± 0.1 eV were determined for the (100), (110), and (111) orientations (**Figure 24**), respectively. This result aligns well with the n-type semiconducting nature of TiO_2. The Fermi level of perovskite thin films on glass substrates was determined to be -4.2 ± 0.1 eV. In the SC TiO_2/perovskite assemblies, the perovskite Fermi-level shifted to -5.2 ± 0.1 eV. This results from the larger depletion width (~300 nm) of the perovskite material than the employed thickness in this study (100 nm).[143] As a result, the depletion region stretches across the entire layer, which alters the surface Fermi level.[144]

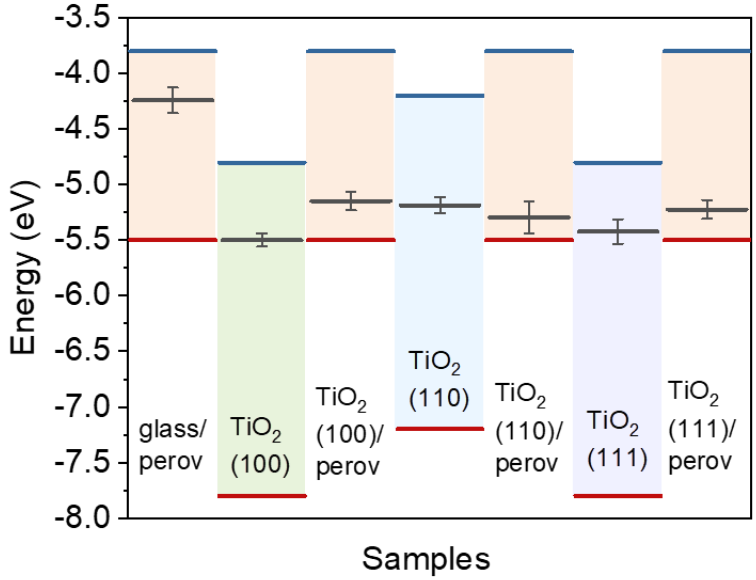

Figure 24. Band positions and Fermi levels of glass/perovskite and SC TiO_2/perovskite assemblies. Error bars are derived from measurements taken on three separate samples. Reproduced from ref [12].

4.2.3 Electron extraction process at SC TiO_2/perovskite interface

SPS measurement is an effective technique to investigate the alteration in charge distribution of sample surfaces after light excitation. As shown in the SPS spectra (**Figure 25**), the perovskite layers on glass substrates show a positive photovoltage. This indicates an electron buildup at the surface, either in the space charge region of the films or at defect/trap sites.[145,146] In contrast, negative photovoltages were obtained for TiO_2/perovskite assemblies in all TiO_2 orientations. This signals that the photo-generated electrons were efficiently extracted by the TiO_2 substrates, leaving the positive holes localized at the perovskite surface. These results show that the used rutile TiO_2 single crystals can serve as ETLs in PSCs. Additionally, the photon energy onset of the SPS spectra can be used to determine the electronic bandgap value of the perovskite layers. A lower bandgap value (1.44 eV) was obtained for the perovskite layer on both glass and TiO_2 single crystals, compared to the values from UV-vis spectra. This is an indication of the existence of defects and trap states at the surface of the perovskite layers.

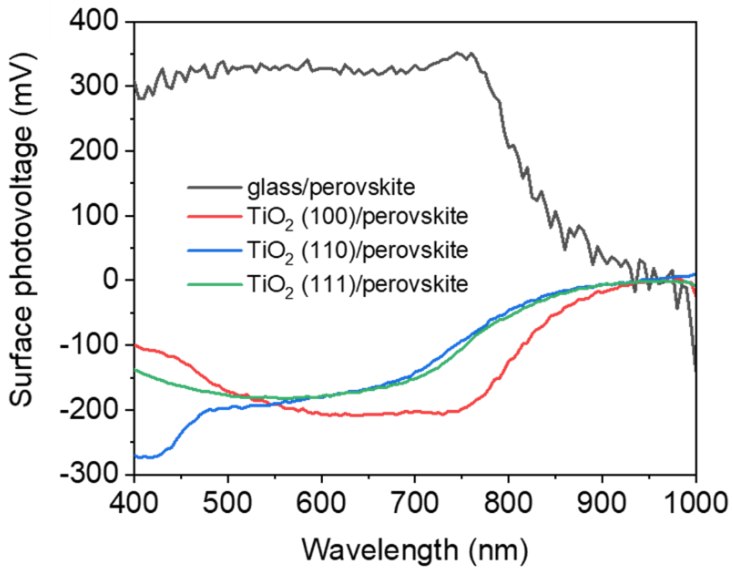

Figure 25. SPS spectra of perovskite layers on glass and SC TiO_2 substrates. Reproduced from ref[12].

To understand the kinetics of charge transfer at the different TiO_2/perovskite interfaces, both TRPL and TA measurements were carried out. As an initial step, we recorded the steady-state photoluminescence (PL) spectra of the samples (**Figure 26A**). Perovskite layers on all

substrates showed a PL peak at 750 nm, aligning well with literature values. The intensity of the PL peak of the perovskite layers on the SC TiO_2 substrates was smaller (29.4%, 44.3%, and 33.1% for TiO_2 (100), (110), and (111), respectively) than that recorded on the glass substrate (**Table 8**). This PL quenching phenomenon can also be the result of electron extraction by the TiO_2 substrate. Interestingly, a more pronounced quenching was observed for the interface with a larger CB offset, which can signal a more efficient electron transfer process. TRPL measurements, which monitor the radiative recombination of excited charge carriers, were performed to verify this notion (**Figure 26B**). Following the proposed evaluation protocols listed above, we adopted tri-exponential fitting and extracted the average lifetime, which is model independent, to analyze the TRPL decay curves. The details of the fitting parameters used and calculated average lifetimes are summarized in **Table 9**. Similar to the steady state PL results, shorter TRPL decay lifetimes were observed for perovskite layer on SC TiO_2 substrates (TiO_2 (100)/perovskite, τ_{avg}=8.8 ns; TiO_2 (110)/perovskite, τ_{avg}=16.7 ns; and TiO_2 (111)/perovskite, τ_{avg}=10.3 ns), compared with that on glass substrate (τ_{avg}=24.0 ns). As the perovskite layer qualities were identical on all substrates, the decreased average lifetime further supports electron extraction by the TiO_2 substrates. Additionally, for the TiO_2/perovskite interfaces with larger CB offsets (TiO_2 (100)/perovskite and TiO_2 (111)/perovskite), the average lifetimes were even shorter compared with the interface with a smaller CB offset (TiO_2 (110)/perovskite). The trend of average lifetime decreasing aligns well with the trend in the PL intensity quenching. In the fitting parameters, the longest component can be ascribed to direct band-to-band recombination (~100 ns).[93,133,147] The middle component to trap state assisted charge trapping processes (~30 ns), and the shortest component to a combination of charge trapping and electron transfer processes (<10 ns). The trend of the shortest components does not seem to align with the trend observed for the average lifetimes (**Table 9**). However, the relative amplitudes of these fast decay components exhibit a clear dependence on the TiO_2/perovskite CB offset (**Table 9**).

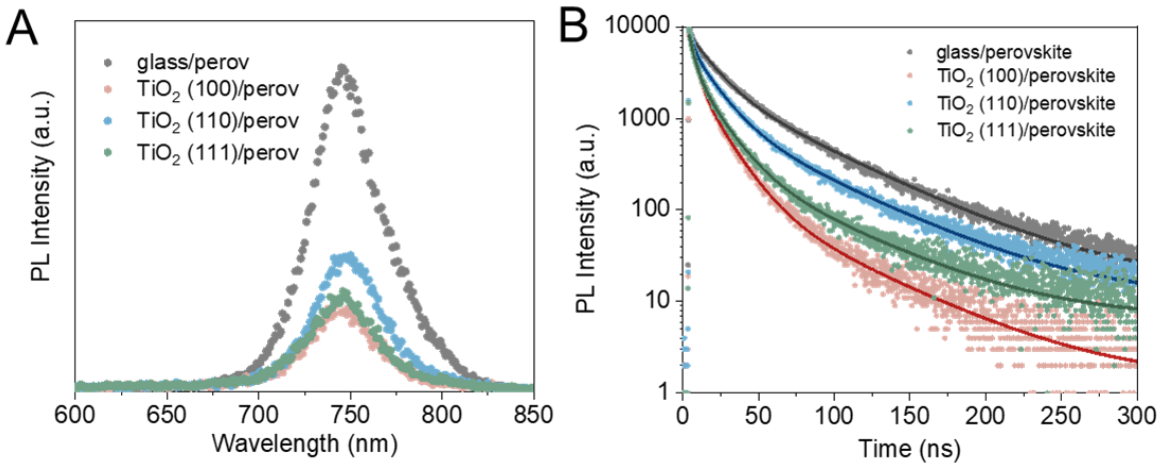

Figure 26. Steady state PL of perovskite layers on glass and single crystal TiO_2 substrates. (A) TRPL decay curves monitored at peak wavelength (750 nm). (B) Excitation wavelength: 467 nm. Excitation fluence: 29 nJ /cm^2. Reproduced from ref [12].

Table 8. PL quenching percentage of SC TiO_2/perovskite assemblies in comparison with glass/perovskite. Reproduced from ref [12].

Sample	PL intensity compared to glass/perovskite
Glass/perovskite	100%
TiO_2 (100)/perovskite	29.4%
TiO_2 (110)/perovskite	44.3%
TiO_2 (111)/perovskite	33.1%

Table 9. Used fitting parameters and calculated average lifetimes of perovskite layers on glass and SC TiO_2 substrates. Reproduced from ref [12].

	τ_1 (ns)	A_1	τ_2 (ns)	A_2	τ_3 (ns)	A_3	τ_{ave} (ns)
Glass/perovskite	6.9	0.43	29.9	0.51	97.2	0.06	24.0
TiO_2 (100)/perovskite	4.8	0.78	19.6	0.21	97.2	0.01	8.8
TiO_2 (110)/perovskite	5.5	0.55	23.9	0.41	97.2	0.04	16.7
TiO_2 (111)/perovskite	3.7	0.63	17.2	0.35	97.2	0.02	10.3

TRPL monitors the electron transfer process in a time scale of ~300 ns. TA measurements, are capable of probing sub-picosecond processes, were performed to investigate electron

transfer processes on the ultra-fast time scales. We employed global analysis for evaluating the TA spectra of perovskite layers on various substrates. The obtained decay-associated spectra (DAS) are presented in **Figure 27**. In all cases, the transient spectra can be deconvoluted by one constant and three exponential components. In these cases the shortest component represents the hot carrier cooling process, as its characteristic timescale (~0.2 ps) aligns with typical hot carrier relaxation dynamics.[90,148] This assignment is further supported by the DAS, which extends to the high-energy (short-wavelength) spectral region. The middle components were relatively small and were neglected in further analysis. The longest component describes the relaxation of the GSB signal, which can be monitored to reveal the recombination of the excited charge carriers. Consequently, we plotted the TA spectra at various delay times of perovskite layers on different substrates (**Figure 28**). The relaxation of the GSB peak is the result of the gradual recombination of excited carriers, being trapped in trap states or being extracted by a TiO_2 layer.

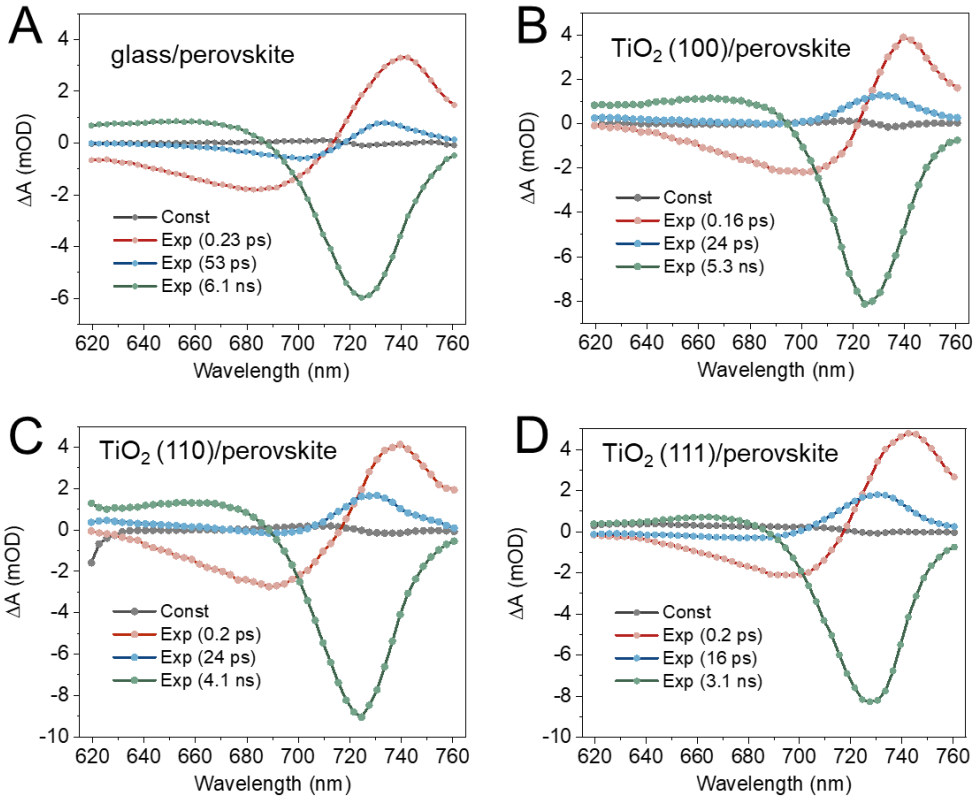

Figure 27. DAS obtained from the global analysis of the TA spectra of perovskite layers on glass and SC TiO_2 substrates. Excitation wavelength: 600 nm, excitation fluence: 5.7 μJ/cm^2. Adapted from ref[12].

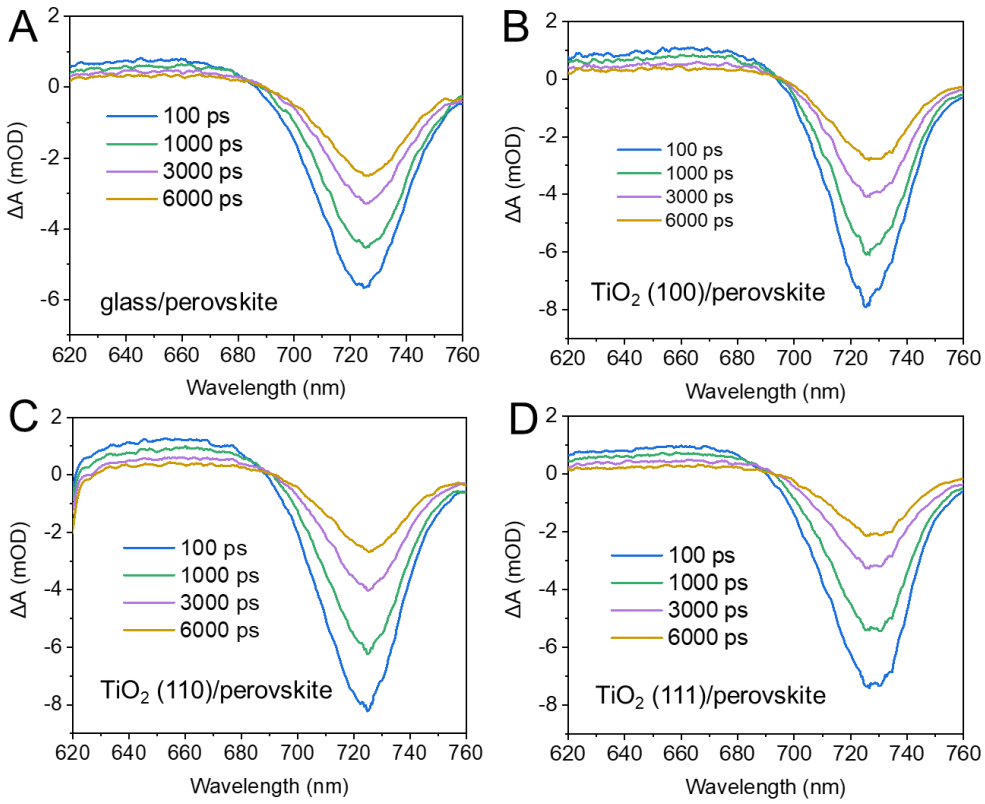

Figure 28. TA spectra recorded at various time delays of perovskite layers on glass and SC TiO_2 substrates. Excitation wavelength: 600 nm, excitation fluence: 5.7 μJ/cm^2. Adapted from ref [12].

The normalized decay traces of the GSB signal at 725 nm of perovskite layers on different substrates were plotted in **Figure 29**. The employed excitation fluence can influence the initial carrier concentration generated in the perovskite layers. To investigate how this influences the kinetics of the electron transfer process at the TiO_2/perovskite interface, we varied the excitation fluence. Notably, no difference was seen between the decay traces of perovskite layers on glass substrate and single crystal TiO_2 substrates at low excitation fluences of 0.7 μJ/cm^2 and 2.8 μJ/cm^2 (**Figure 29A** and **29B)**. This indicated that no charge transfer occurred in the probed time scale (several ns) at these two excitation fluences, even when perovskite layers were interfaced with the TiO_2 substrates. Differences between the glass/perovskite and TiO_2/perovskite samples were only observed when an excitation fluence of 5.7 μJ/cm^2 was applied (**Figure 29C**). Similarly to the TRPL results, an acceleration of the excited state relaxation in this case can be attributed to electron extraction. One potential explanation for the excitation fluence dependence of the electron extraction process can be the existence of an electric barrier at TiO_2/perovskite interface region.[89,149]

Electron accumulation at the CB of perovskite, which results from high excitation fluence, is needed to conquer this barrier. However, in the case of TRPL results, the electron extraction process was observed at lower excitation fluences (29 nJ/cm^2). This seeming contradiction can be rationalized by considering the higher excitation frequency used in the case of TRPL (1 MHz), compared to that employed in TA (1 kHz). In LHPs slow charge trapping and de-trapping processes (in the time scale of microseconds) were shown.[36] In the case of TRPL, due to the employed high frequency, the time interval between the two laser pulses is shorter than the charge de-trapping processes. This means that the measurements were conducted with the trap states filled. This "photodoping" effect can cause a similar charge accumulation that can assist the overcoming the electric barrier at the TiO_2/perovskite interface.

The decay traces under the highest excitation fluence were fitted to evaluate the electron transfer kinetics. A stretched exponential function was applied.[150,151] The details of used fitting parameters used can be found in **Table 10**. The perovskite layers on different substrates shared similar stretching parameters (β), allowing us to directly compare the four lifetime components. The lifetime (τ) followed the trend: τ (glass/perovskite, 6.1 ns) > τ (TiO_2 (100)/perovskite, 5.3 ns) > τ (TiO_2 (110)/perovskite, 4.1 ns) > τ (TiO_2 (111)/perovskite, 3.1 ns), indicating that all TiO_2 facets were effective in extracting electrons. The TiO_2 (111) substrate was the most efficient, and TiO_2 (100) was the least efficient, in the probed timescale (several ns). This result is inconsistent with the trend derived from the TRPL result (in the time scale of several hundreds of ns), where TiO_2 (100) was found to be the most efficient. Can this inconsistency come from the influence of processes at even earlier time scale? We decided to investigate the excited charge carrier dynamics within 1 ps to explore the hot carrier behaviours.

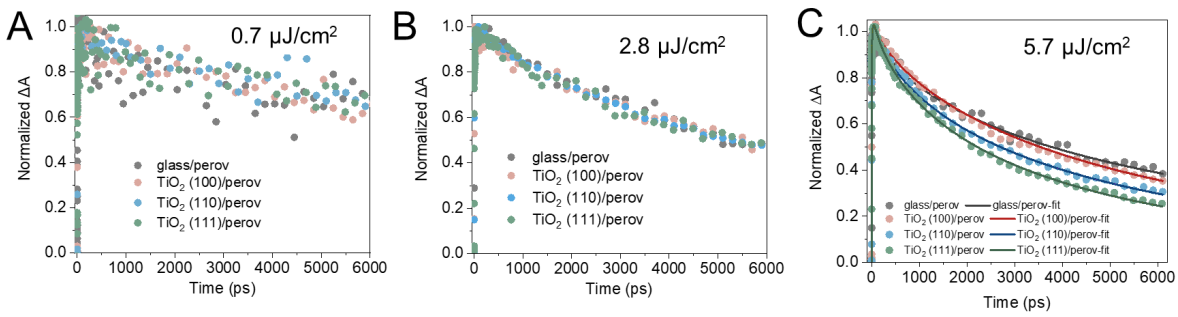

Figure 29. TA decay traces at 725 nm for perovskite layers on different substrates at the excitation fluence of (A) 0.7 μJ/cm^2, (B) 2.8 μJ/cm^2, and (C) 5.7 μJ/cm^2. Excitation wavelength: 600 nm. Adapted from ref [12].

Table 10. Fitting parameters for TA decay traces of perovskite layers on different substrates at an excitation fluence of 5.7 μJ/cm^2. Reproduced from ref [12].

Sample	τ (ns)	β
Glass/perovskite	6.1 ± 0.1	0.64 ± 0.02
TiO_2 (100)/perovskite	5.3 ± 0.1	0.70 ± 0.01
TiO_2 (110)/perovskite	4.1 ± 0.1	0.64 ± 0.1
TiO_2 (111)/perovsskite	3.1 ± 0.1	0.64 ± 0.2

We turned our attention to the TA spectra in the several picoseconds timescales, where the contribution of hot carriers can be evaluated. Hot carriers are generated by excitation energies that exceed the bandgap of the perovskite. These hot carriers thermalize to the CB of perovskite within 1 ps. [90,148] By fitting the GSB high energy tail with a Maxwell–Boltzmann distribution function, the hot electron temperature (T_c) can be extracted.[90,148] To reveal how the excitation fluence influences the hot carrier relaxation process, data recorded with two different excitation fluences were evaluated. The fitted high energy tails of the TA spectra at an excitation fluence of 5.7 μJ/cm^2 and 2.8 μJ/cm^2 are shown in **Figure 30** and **31**, respectively. The high energy tails of perovskite layers are wider in the case of 5.7 μJ/cm^2 compared to 2.8 μJ/cm^2, indicating that more hot carries were generated.

The extracted hot electron temperatures (T_c) were plotted at different times for all samples (**Figure 32**). As a baseline, the employed 600 nm wavelength excitation possesses a photon energy of 2.06 eV. Subtracting the perovskite bandgap energy (1.68 eV), an excess energy of 0.38 eV can be calculated, which corresponds to a Kelvin temperature of 4410 K. The

determined hot electron temperatures extracted from the fittings showed a ~1000 K starting value, which means that within 10 fs, the majority of the excess energy is lost (**Figure 32**). When the applied excitation fluence was at 2.8 μJ/cm^2, the cooling kinetics of hot electron temperatures of perovskite layers on all substrates were similar (**Figure 32A**). In contrast, the cooling kinetics of all TiO_2/perovskite samples were observed to be faster than the glass/perovskite one, suggesting that portions of hot electrons that were close to the TiO_2/perovskite interface were extracted (**Figure 32B**). The hot electron extraction of TiO_2 (100) was the fastest, followed by TiO_2 (111) and (110). This trend aligns well with the CB position offset trend. This fast hot electron extraction of the TiO_2 (100) substrate can cause a rapid electron accumulation at the TiO_2 side after 1ps. These accumulated electrons in the CB of TiO_2 can suppress the lateral electron extraction process, as shown in the slow TA decay traces (at the time scale of several ns). The extraction of electrons accelerates only after the accumulated electrons are depleted, either through diffusion or recombination with holes in the perovskite.[152,153] This delayed acceleration in extraction dynamics is evidenced by the TRPL decay traces, which occurs on a timescale of several hundred nanoseconds.

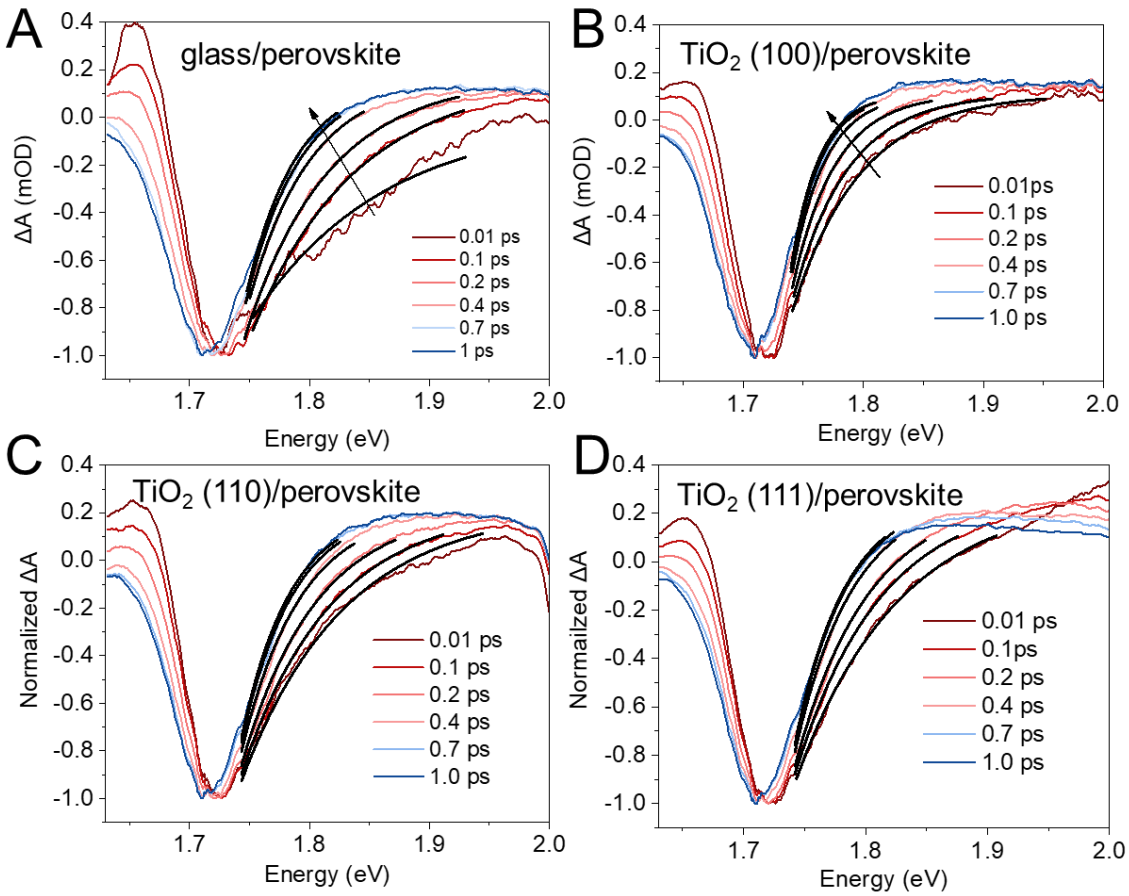

Figure 30. Normalized TA spectra with fitting results of perovskite layers on different substrates, measured at various delay times within 1 ps. (A) glass/perovskite, (B) TiO_2 (100)/perovskite, (C) TiO_2 (110)/perovskite, and (D) TiO_2 (111)/perovskite. The x-axis is presented in energy units. Excitation fluence: 5.7 μJ/cm^2, excitation wavelength: 600 nm. Reproduced from ref[12].

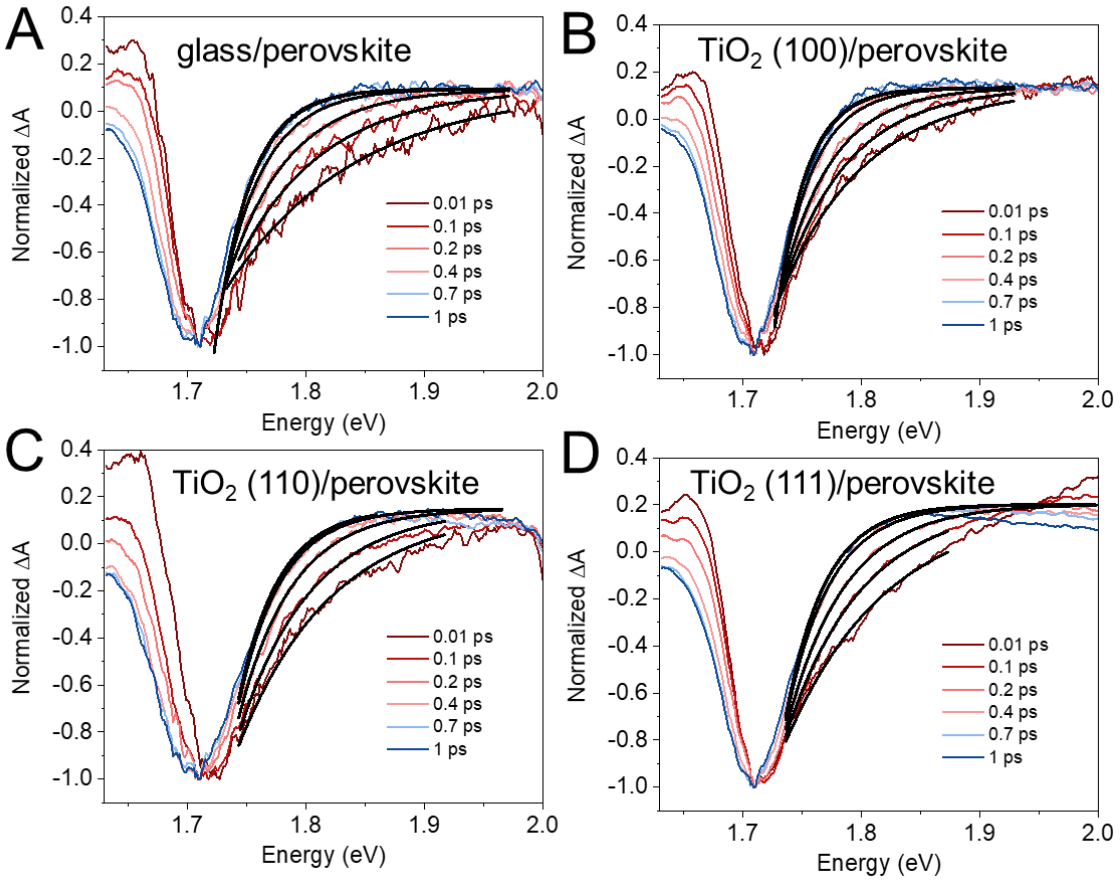

Figure 31. Normalized TA spectra with fitting results of perovskite layers on different substrates, measured at various delay times within 1 ps. (A) glass/perovskite, (B) TiO_2 (100)/perovskite, (C) TiO_2 (110)/perovskite, and (D) TiO_2 (111)/perovskite. The x-axis is presented in energy units. Excitation fluence: 2.8 μJ/cm^2, excitation wavelength: 600 nm. Reproduced from ref[12].

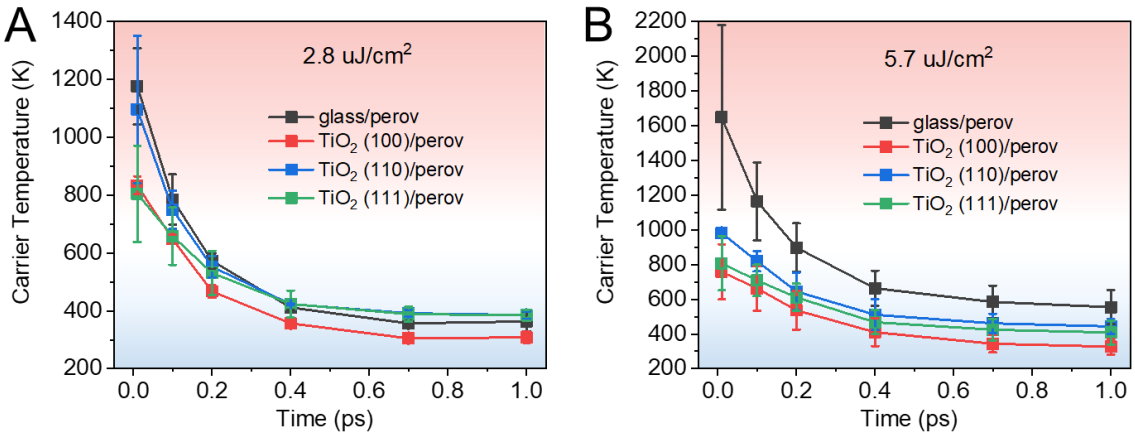

Figure 32. Hot electron cooling profiles of perovskite layers on different substrates at the excitation fluence of (A) 2.8 μJ/cm^2 and (B) 5.7 μJ/cm^2. Excitation wavelength: 600 nm. Adapted from ref[12].

The effect of excitation fluence on the charge transfer processes is often overlooked. **Figure 33** summarizes the effect of excitation fluence on both hot electron and band-edge electron transfer processes. With a high excitation fluence, more hot electrons are generated. In this case, the chance of these hot electrons being extracted by the TiO_2 is higher. In the band-edge electron extraction process, electron accumulation is required at the CB position of TiO_2 to overcome the electric barrier and initiate electron transfer. This also requires a high excitation fluence to generate more excited charge carriers in the perovskite layer.

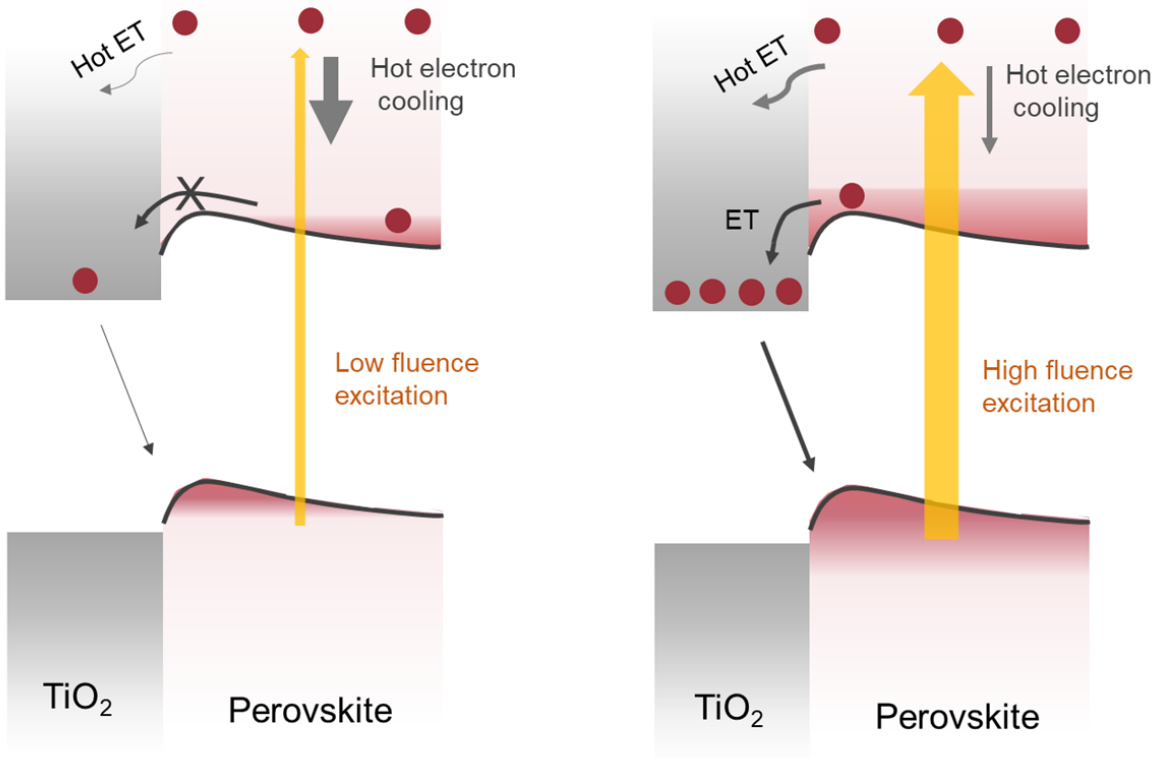

Figure 33. Mechanistic insights on how the employed excitation fluence influences hot electron and band-edge electron extraction processes at TiO_2/perovskite interface. Reproduced from ref[12].

4.3 The Effect of Valence Band Offset on the Kinetics of Hole Extraction in mp-NiO/Perovskite assemblies

4.3.1 Characterization of mp-NiO/perovskite layers

As an initial step, we prepared mesoporous-NiO (mp-NiO) layers with galvanostatic electrodeposition. By varying the amount of passed charge (30 mC cm^{-2}, 60 mC cm^{-2} and 120 mC cm^{-2}) the thickness of the produced mp-NiO layer can be tuned. SEM images show that the mp-NiO layers have a porous morphology (**Figure 34**), and the walls of the interconnected nano-flakes grow larger as the passed charges increases.

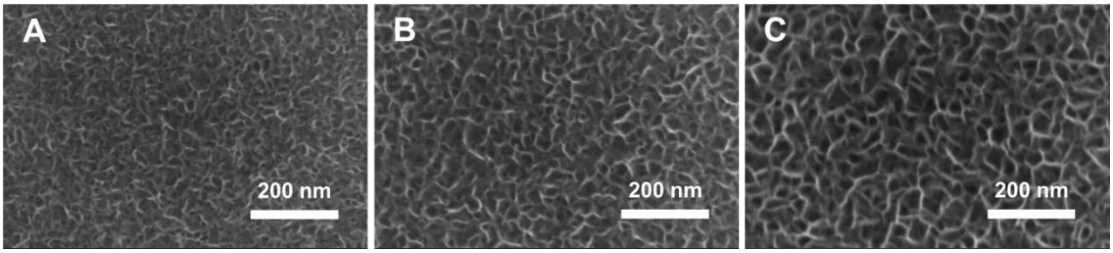

Figure 34. Top-down SEM images of the prepared mp-NiO layers with galvanostatic electrodeposition with passed charges of 30 mC cm^{-2} (A), 60 mC cm^{-2} (B) and 120 mC cm^{-2} (C) on ITO substrates. Reproduced from ref[154].

Perovskite layers of 3 different compositions ($FA_{0.83}Cs_{0.17}PbI_3$, $FA_{0.83}Cs_{0.17}Pb(I_{0.83}Br_{0.17})_3$, and $FA_{0.83}Cs_{0.17}Pb(I_{0.6}Br_{0.4})_3$) were prepared by spin coating method on top of the thickest mp-NiO layers to avoid short circuit contact. To separate charge transfer and charge trapping processes by TA measurements, control over the perovskite layer properties (e.g., crystallinity, grain size, film thickness) are needed.[35] The XRD patterns (**Figure 35**) of perovskite layers of three compositions revealed the formation of desired phases in all cases. The position of the (100) plane shifts toward higher diffraction angles as more bromide is incorporated into the lattice that causes lattice shrinking .[141,142]

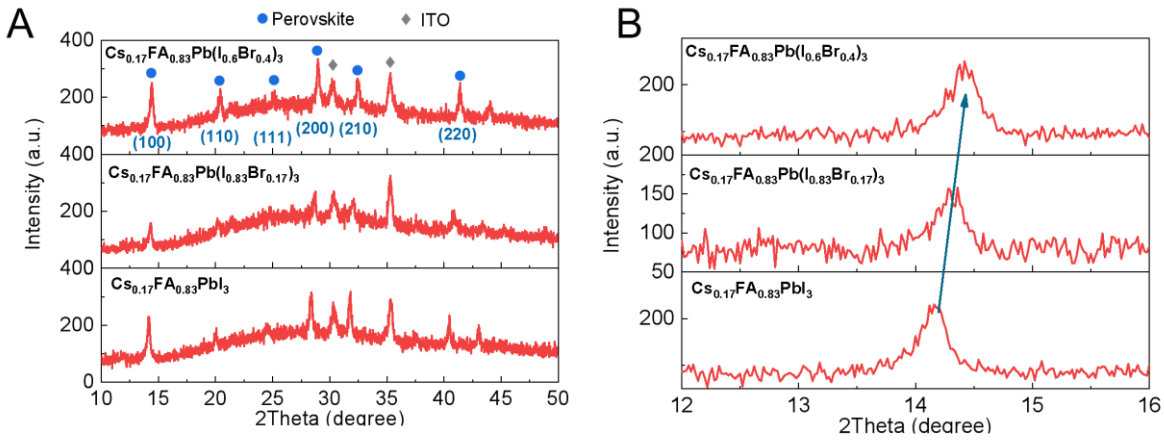

Figure 35. Full-range (A) and magnified region of the XRD patterns (B) of the three different perovskite compositions. Reproduced from ref[154].

To check the grain size of perovskite films with different compositions, SEM images were recorded (**Figure 36**). Grain size distribution show that the $FA_{0.83}Cs_{0.17}PbI_3$ composition has an average grain diameter of 116 ± 47 nm, while the other two compositions have smaller grain diameters (95 ± 31 nm). This can be caused by bromide incorporation into the lattice.[155]

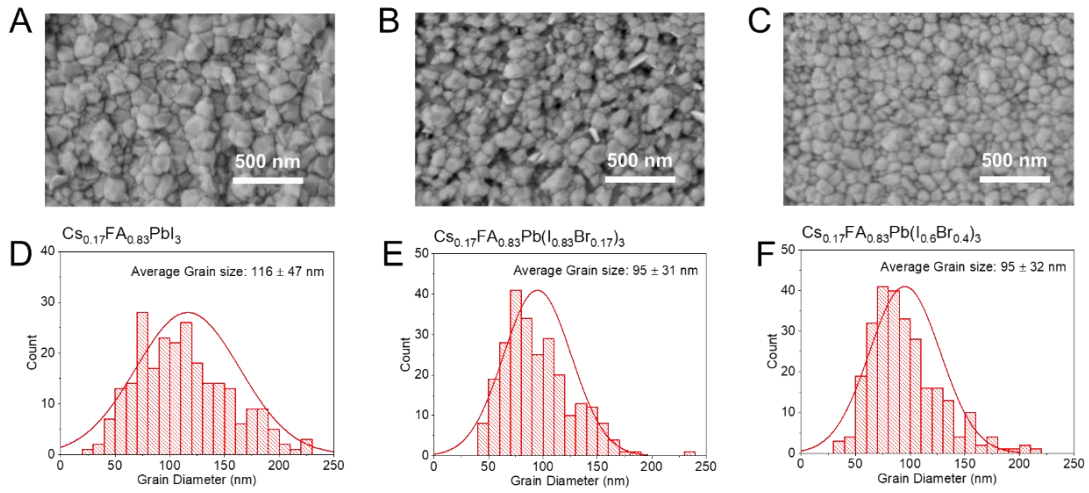

Figure 36. Top-down SEM images and grain size distribution of $FA_{0.83}Cs_{0.17}PbI_3$ (A, D), $FA_{0.83}Cs_{0.17}Pb(I_{0.83}Br_{0.17})_3$ (B, E), and $FA_{0.83}Cs_{0.17}Pb(I_{0.6}Br_{0.4})_3$ (C, F) prepared on ITO/mp-NiO substrates. Reproduced from ref[154].

To ensure there is no contact between ITO and perovskite through mp-NiO layer, SPS measurements were carried out (**Figure 37A**). The intermediate bromide composition was chosen to optimize the layer thickness. When this perovskite was directly deposited on the ITO substrate, negative SPV was detected, indicating a decreased number of electrons at the surface. This reveals that electrons can be transferred to the ITO substrate, while holes can

accumulate on the surface. When we deposited the perovskite layer on the thinnest (30 mC cm^{-2}) mp-NiO substrates, the obtained SPV remained negative, indicating there is still direct contact between the perovskite layer and the ITO substrate. This behavior changed when thicker (60 mC cm^{-2}) mp-NiO substrates were used as the SPV became positive at shorter excitation wavelength. This suggests an electron build-up at the surface of the perovskite layers, while holes are extracted by the mp-NiO layer. However, at this mp-NiO thickness, the cut-off of the positive SPV signal was seen at slightly shorter wavelengths compared to the expected bandgap of this compositions. This means separation between ITO and perovskite layer was not fully achieved and a mixed behavior can be observed. The complete separation could only be achieved by depositing thick (120 mC cm^{-2}) mp-NiO layers. These showed positive SPV at all excitation wavelengths and were used with all three perovskite compositions.

SPS of other two perovskite compositions were also measured (**Figure 37B**), positive values were detected at all wavelengths in both cases, indicating effective hole extraction from the perovskite layer by the mp-NiO layer. The onset wavelengths of all three perovskite compositions reveals a lower band gap (1.4 eV for $FA_{0.83}Cs_{0.17}PbI_3$; 1.5 eV for $FA_{0.83}Cs_{0.17}Pb(I_{0.83}Br_{0.17})_3$; and 1.55 eV for $FA_{0.83}Cs_{0.17}Pb(I_{0.6}Br_{0.4})_3$) than from optical measurement, which is a sign of the existence of surface trap states.[12]

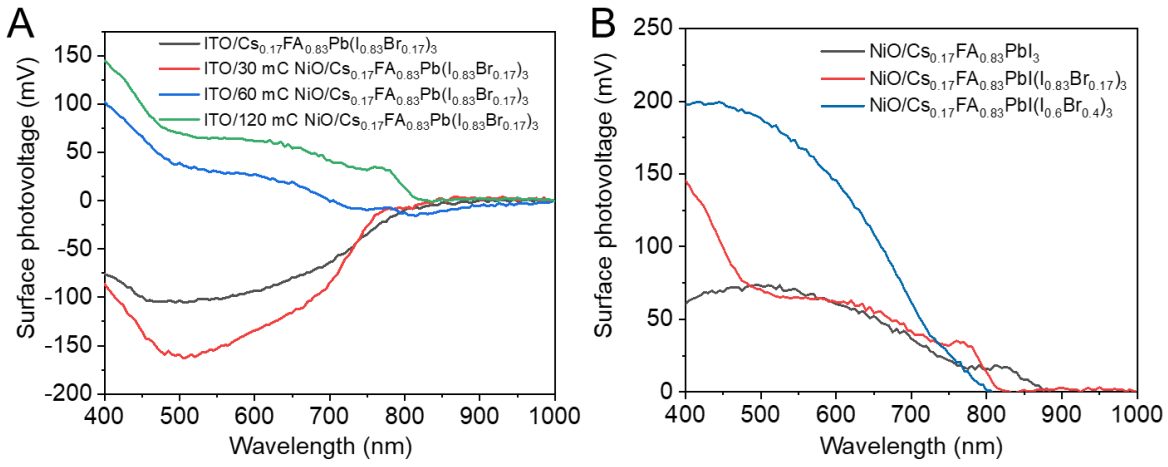

Figure 37. Surface photovoltage measurements of perovskite layer ($FA_{0.83}Cs_{0.17}Pb(I_{0.83}Br_{0.17})_3$) on ITO and ITO/mp-NiO substrates (A). Surface photovoltage results of perovskite layer of three

compositions on ITO/mp-NiO substrates (B). Reproduced from ref[154].

4.3.2 Band alignment at the mp-NiO/perovskite interface

To characterize the optical and electronic properties of the perovskite layers, UV-vis spectra were recorded (**Figure 38A**). The absorption edge shifted to shorter wavelengths as more bromide was incorporated into the lattice ($FA_{0.83}Cs_{0.17}PbI_3$, 800 nm; $FA_{0.83}Cs_{0.17}Pb(I_{0.83}Br_{0.17})_3$, 750 nm; $FA_{0.83}Cs_{0.17}Pb(I_{0.6}Br_{0.4})_3$, 700 nm). As a result, Tauc-analysis (**Figure 38B**) reveals a smaller direct band gap for $FA_{0.83}Cs_{0.17}PbI_3$ (1.5 eV), compared to bromide richer compositions (1.6 eV for $FA_{0.83}Cs_{0.17}Pb(I_{0.83}Br_{0.17})_3$; and 1.8 eV for $FA_{0.83}Cs_{0.17}Pb(I_{0.6}Br_{0.4})_3$). Based on the molar absorption coefficient of perovskites [12], a layer thickness of ~150 nm can be estimated.

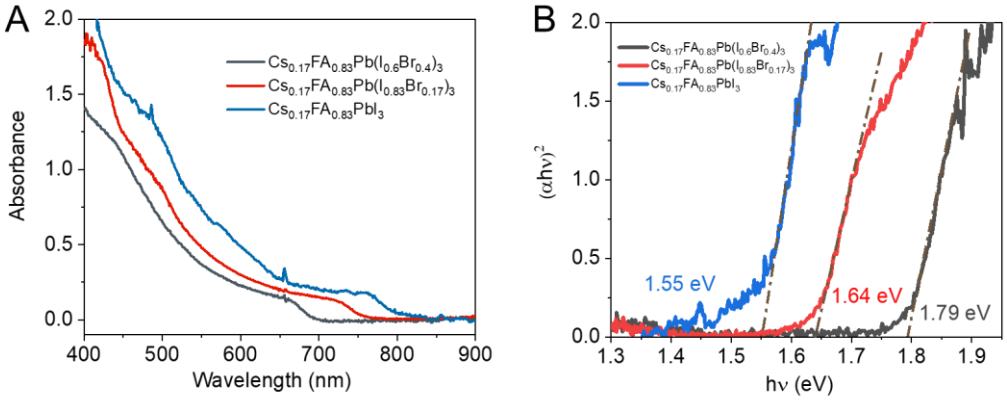

Figure 38. UV-vis absorption spectra of the three perovskite compositions on ITO/mp-NiO substrates. Reproduced from ref[154].

APS was used to characterize the VB position of both mp-NiO and the three perovskite compositions (**Figure 39 A-D**). The results revealed that mp-NiO has a VB position of -5.2 eV. For the perovskite layers a more negative VB position was determined in all three cases, which thermodynamically allows the hole extraction process from perovskite layer to mp-NiO layer. Among all, $FA_{0.83}Cs_{0.17}PbI_3$ has the most positive VB position (-5.4 eV), followed by -5.5 eV for $FA_{0.83}Cs_{0.17}Pb(I_{0.83}Br_{0.17})_3$ and -5.6 eV for $FA_{0.83}Cs_{0.17}Pb(I_{0.6}Br_{0.4})_3$. Therefore, mp-NiO/ $FA_{0.83}Cs_{0.17}PbI_3$ has the smallest VB position difference at the interface (0.2 eV), followed by mp-NiO/$FA_{0.83}Cs_{0.17}Pb(I_{0.83}Br_{0.17})_3$ (0.3 eV) and mp-NiO/$FA_{0.83}Cs_{0.17}Pb(I_{0.6}Br_{0.4})_3$ (0.4 eV). Together with the previously determined band gaps,

the CB positions can be calculated accordingly. The band alignment condition of mp-NiO and perovskite with three compositions are summarized in **Figure 39E**.

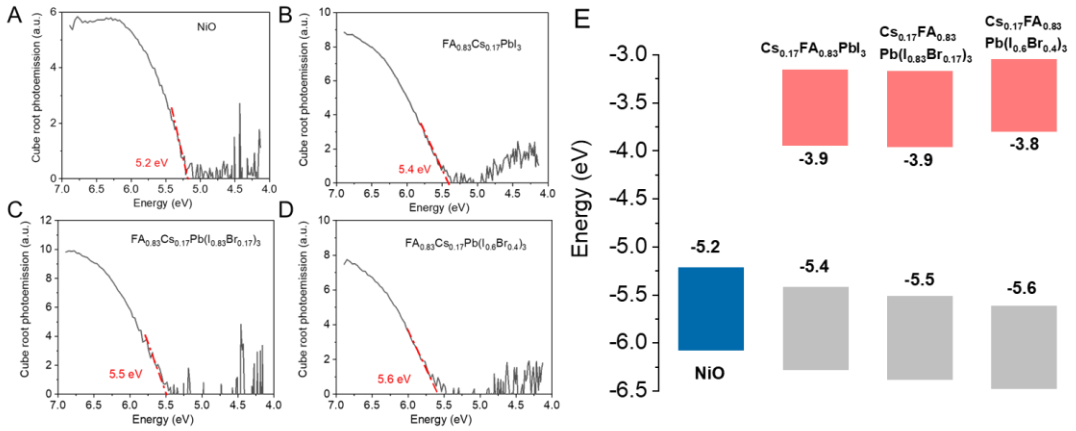

Figure 39. Ambient-pressure photoemission spectroscopy (APS) results of mp-NiO (A), $FA_{0.83}Cs_{0.17}PbI_3$ (B), $FA_{0.83}Cs_{0.17}Pb(I_{0.83}Br_{0.17})_3$ (C), and $FA_{0.83}Cs_{0.17}Pb(I_{0.6}Br_{0.4})_3$ (D). Schematic representation of the band alignment of mp-NiO layer and perovskite layers of three compositions (E). Adapted from ref[154].

4.3.3 Hole extraction process at mp-NiO/perovskite interface

To ensure sample stability to laser exposure and confirm the validity of the results, multiple measurements on the same spot and perovskite layer homogeneity check were carried out. The obtained GSB positions depend on perovskite composition, with bromide-rich compositions exhibiting GSB at shorter wavelengths (**Figure 40 A, C, E**). This negative GSB peak decreased over time caused by recombination, trapping, or extraction of holes by the mp-NiO layer. For mp-NiO/$FA_{0.83}Cs_{0.17}PbI_3$ and mp-NiO/$FA_{0.83}Cs_{0.17}Pb(I_{0.83}Br_{0.17})_3$ samples, the obtained GSB intensities and decay kinetics show no obvious difference even after three consecutive measurements (**Figure 40 A-D**), indicating good sample stability as it being exposed to laser. However, for the mp-NiO/$FA_{0.83}Cs_{0.17}Pb(I_{0.6}Br_{0.4})_3$ sample, the GSB peak shifted towards longer wavelengths by ~ 9nm even within one measurement (**Figure 40E** and **40C**), suggesting slight phase segregation. To trace the decay kinetic precisely, we plot the decay traces at each GSB maximum at every time delay, no obvious difference was observed from three measurements (**Figure 40F**). TA measurements were carried out on three different spots on mp-NiO/perovskite of three compositions samples to check the sample homogeneity. All three compositions samples showed good sample

homogeneity in terms of both GSB intensities and decay kinetics, except mp-NiO/$FA_{0.83}Cs_{0.17}Pb(I_{0.6}Br_{0.4})_3$ shows the same segregation problem (**Figure 41**).

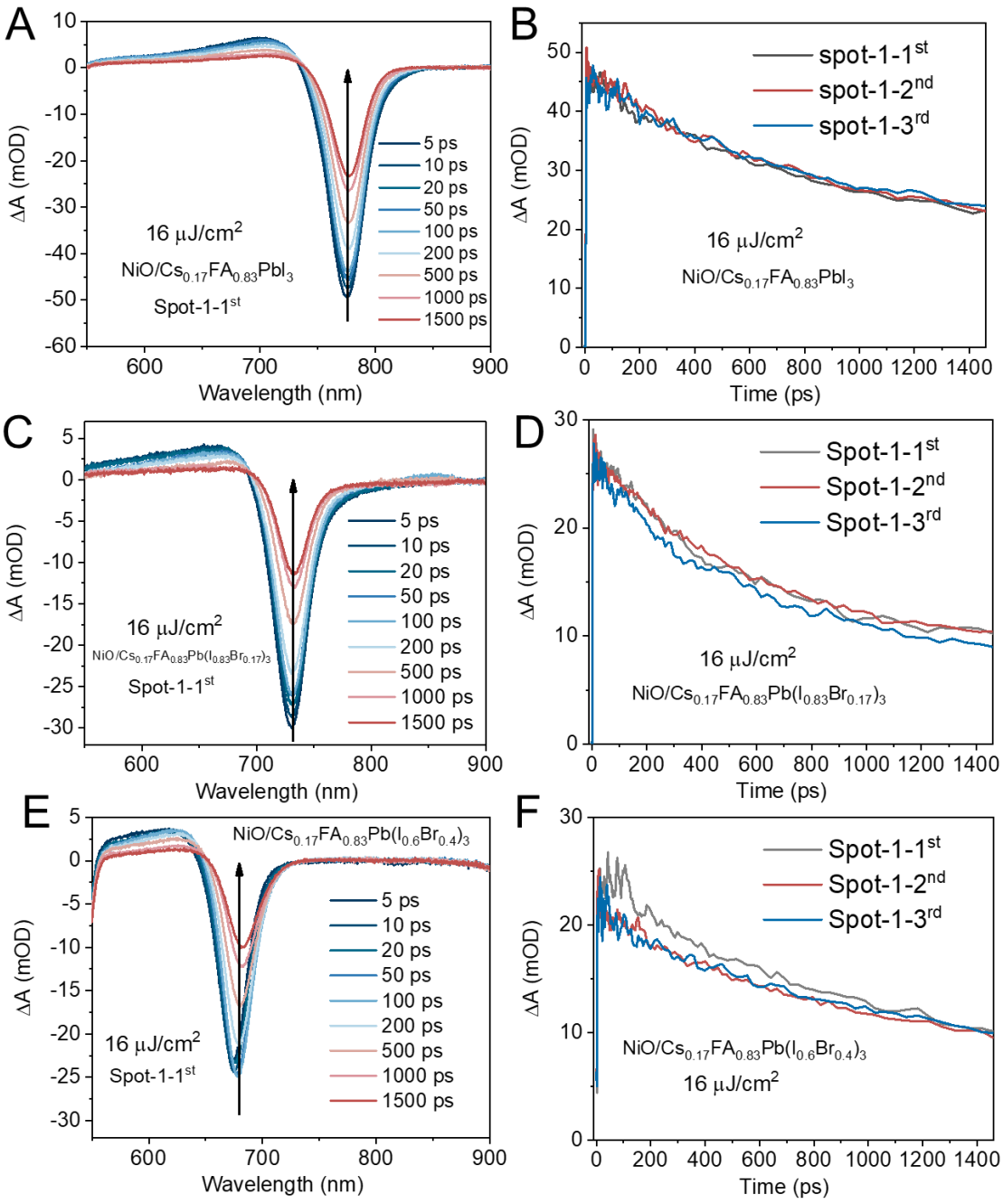

Figure 40. TA measurements were conducted on the same spot of mp-NiO/$FA_{0.83}Cs_{0.17}PbI_3$, mp-NiO/$FA_{0.83}Cs_{0.17}Pb(I_{0.83}Br_{0.17})_3$ and mp-NiO/$FA_{0.83}Cs_{0.17}Pb(I_{0.6}Br_{0.4})_3$ for three times. TA spectra of mp-NiO/$FA_{0.83}Cs_{0.17}PbI_3$ (A), mp-NiO/$FA_{0.83}Cs_{0.17}Pb(I_{0.83}Br_{0.17})_3$ (C) and mp-NiO/$FA_{0.83}Cs_{0.17}Pb(I_{0.6}Br_{0.4})_3$ (E) at various delay times of first measurement, decay traces at GSB maximum of mp-NiO/$FA_{0.83}Cs_{0.17}PbI_3$ (B), mp-NiO/$FA_{0.83}Cs_{0.17}Pb(I_{0.83}Br_{0.17})_3$ (D) and mp-NiO/$FA_{0.83}Cs_{0.17}Pb(I_{0.6}Br_{0.4})_3$ (F) at the same spot for three times. Excitation wavelength: 515 nm, excitation fluence: 16 μJ/cm^2. Adapted from ref[154].

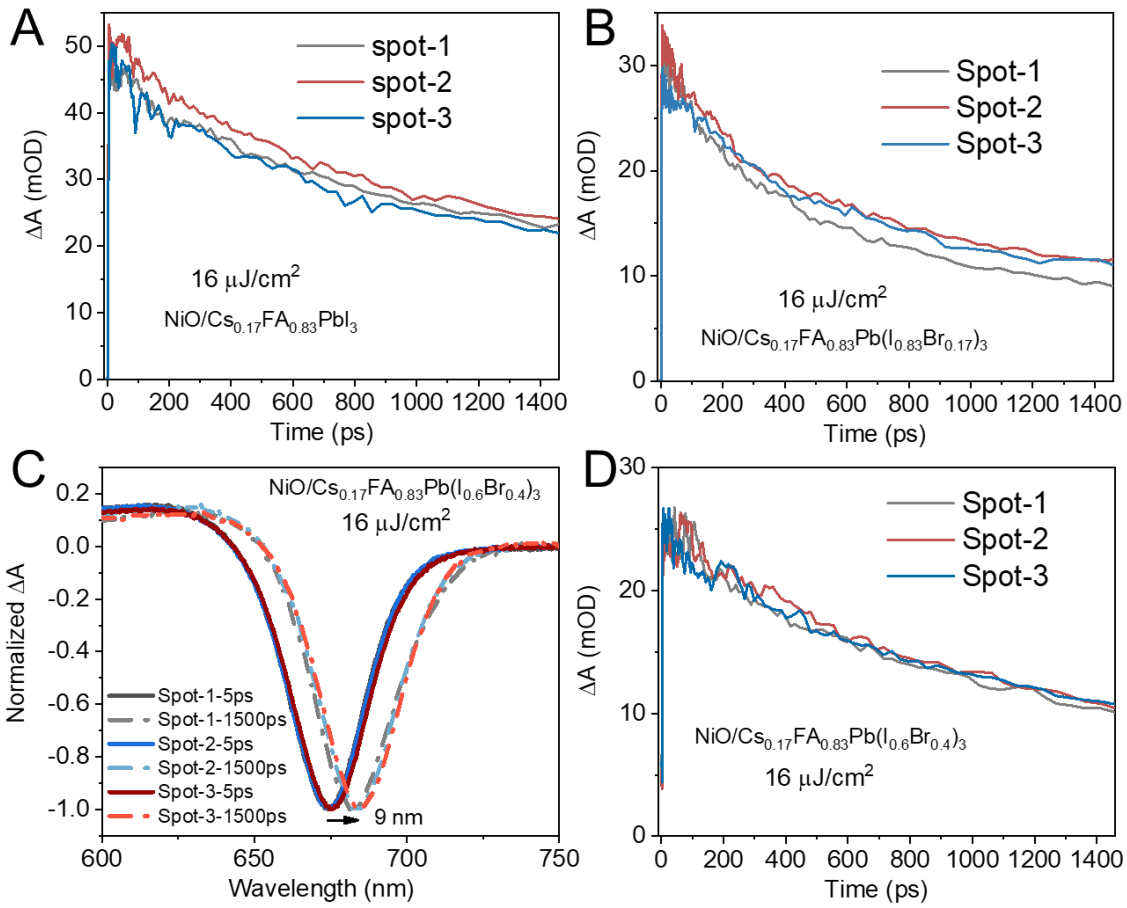

Figure 41. TA measurements were carried out at three different spots on mp-NiO/perovskite layers. Decay traces at GSB maximum of mp-NiO/$FA_{0.83}Cs_{0.17}PbI_3$ (A), mp-NiO/$FA_{0.83}Cs_{0.17}Pb(I_{0.83}Br_{0.17})_3$ (B) and mp-NiO/$FA_{0.83}Cs_{0.17}Pb(I_{0.6}Br_{0.4})_3$ (D). TA spectra at 5 ps and 1500 ps at 3 different spots of mp-NiO/$FA_{0.83}Cs_{0.17}Pb(I_{0.6}Br_{0.4})_3$ sample (C). Excitation wavelength: 515 nm, excitation fluence: 16 μJ/cm^2. Adapted from ref[154].

To evaluate the kinetics of hole transfer from the perovskite layers to mp-NiO, TA measurements were conducted. As the initial carrier concentration influences the photophysical processes[12,35], we varied the excitation fluence. As we increased the excitation fluence from 3 to 48 μJ/cm^2, higher ground state bleach (GSB) peak was recorded (see **Figure 42A**, **and 42B**). This is the result of an increased number of excited charge carriers generated at higher excitation fluences. The ΔA recorded at the GSB maximum for each perovskite compositions shows a linear trend in the 3-32 μJ/cm^2 excitation fluence range (excited carrier concentration: 0-5 × 10^{18} cm^{-3}, **Figure 42B**), indicating the samples were

not oversaturated. At higher excitation fluences (excited carrier concentration > 5 × 10^{18} cm^{-3}), slight saturation was seen which can signal the prevalence of higher order recombination processes.[156] Due to the band filling effect[110], higher excited charge carrier concentration can also cause charge accumulation at higher energy levels of the CB, leading to GSB peak (bandgap) widening (**Figure 42C**). The FWHM of the GSB peak of each perovskite composition was plotted versus the excitation fluence (**Figure 42D**). Linear trends were seen in all cases. Due to a slight phase segregation, narrower band broadening was observed in mp-NiO/$FA_{0.83}Cs_{0.17}Pb(I_{0.6}Br_{0.4})_3$ sample, compared to that with mp-NiO/$FA_{0.83}Cs_{0.17}PbI_3$ and mp-NiO/$FA_{0.83}Cs_{0.17}Pb(I_{0.83}Br_{0.17})_3$ samples.

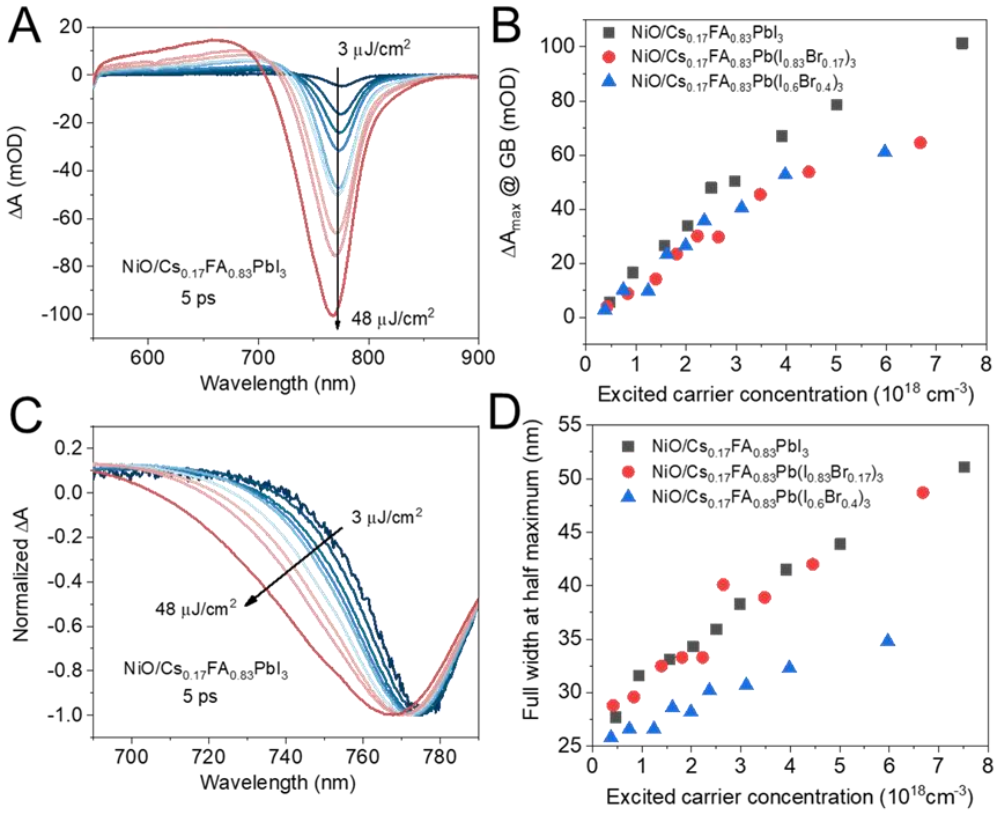

Figure 42. TA spectra measured at various excitation fluences at 5 ps for mp-NiO/$FA_{0.83}Cs_{0.17}PbI_3$ samples (A). GSB ΔAmax for all three perovskite compositions at various excitation fluences (B). Normalized TA spectra at 5 ps at different excitation fluences for mp-NiO/$FA_{0.83}Cs_{0.17}PbI_3$ samples (C), and the FWHM of the GSB for all three perovskite compositions (D). Employed excitation wavelength: 515 nm. Reproduced from ref[154].

TA spectra of mp-NiO/$FA_{0.83}Cs_{0.17}PbI_3$ recorded at a fluence of 16 μJ/cm^2 at various delay

times are shown in **Figure 43A**. This negative GSB peak decreased over time caused by recombination, trapping, or extraction of carriers by the mp-NiO layer. The decay kinetics at GSB peak were plotted at each excitation fluence (**Figure 43B**). At low excitation fluences a slow recovery of the excited state can be observed. The recovery was accelerated as the excitation fluence was increased due to acceleration of carrier recombination and hole extraction (**Figure 43B**). To assess the decay kinetics and to separate first order (carrier trapping and hole extraction) and second order (charge carrier recombination) processes, the decay traces were normalized and fitted by a multi-exponential function (**Figure 43C**). The analysis was conducted only in 3-32 μJ/cm^2 range to avoid the influence of higher order recombination processes. **Figure 44** presents the decay traces and fitting results for the remaining two perovskite compositions. A summary of all fitting parameters, along with the determined average lifetime and the apparent rate constant ($k=1/\tau_{ave}$), is provided in Appendix **Tables A3**, **A4**, **and A5**.

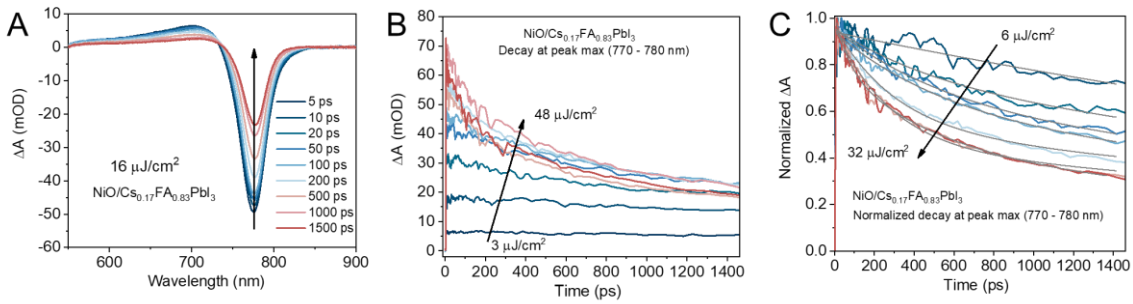

Figure 43. TA spectra at various delay times for mp-NiO/$FA_{0.83}Cs_{0.17}PbI_3$ sample (A), decay traces (B) and normalized decay traces (C) at the GSB maximum for mp-NiO/$FA_{0.83}Cs_{0.17}PbI_3$ samples. Excitation wavelength: 515 nm. Adapted from ref[154].

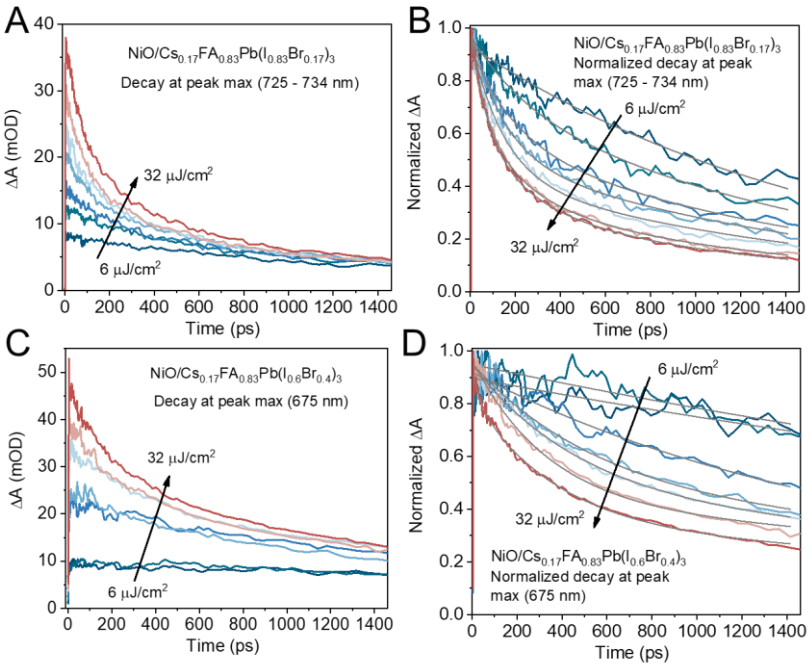

Figure 44. Decay traces (A) and normalized decay traces (B) at the GSB maximum for mp-NiO/$FA_{0.83}Cs_{0.17}Pb(I_{0.83}Br_{0.17})_3$ samples. Decay traces (C) and normalized decay traces (D) at the GSB maximum for mp-NiO/$FA_{0.83}Cs_{0.17}Pb(I_{0.6}Br_{0.4})_3$ samples. Excitation wavelength: 515 nm. Adapted from ref[154].

For further analysis, the apparent rate constant (k) was plotted versus excitation concentrations (N) (**Figure 45**). Linear relationships were found in all cases, in agreement with a previous report.[94] This result is another support that higher order recombination is not prevalent in the studied excitation fluence range. Thus, the obtained k-N trend can be fitted by function:

$$k=k_1+k_2N \quad (14)$$

The intercept k_1 is the rate constant of first order processes, which includes charge trapping and hole extraction processes. While k_2 is the rate constant of second order recombination (band to band recombination) process. A summary of fitting details for all three perovskite compositions are shown in **Table 11**. The first order process is primarily governed by charge extraction in mesoporous CTLs/perovskite assemblies.[94] Therefore, k_1 can be related to the hole extraction process. The trend k_1(mp-NiO/$FA_{0.83}Cs_{0.17}Pb(I_{0.83}Br_{0.17})_3$) > k_1(mp-NiO/$FA_{0.83}Cs_{0.17}PbI_3$) > k_1(mp-NiO/$FA_{0.83}Cs_{0.17}Pb(I_{0.6}Br_{0.4})_3$) indicates hole extraction from perovskite to mp-NiO is the most efficient in the case of mp-NiO/$FA_{0.83}Cs_{0.17}Pb(I_{0.83}Br_{0.17})_3$.

This can be explained by its large VB offset at the interface compared to mp-NiO/$FA_{0.83}Cs_{0.17}PbI_3$. Although mp-NiO/$FA_{0.83}Cs_{0.17}Pb(I_{0.6}Br_{0.4})_3$ has the largest VB offset, phase segregation can lead to hole trapping in iodide-rich regions, thus hindering hole extraction to mp-NiO.[157] Similarly, mp-NiO/$FA_{0.83}Cs_{0.17}Pb(I_{0.83}Br_{0.17})_3$ also has the highest band to band recombination rate constant (largest k_2). This result aligns with earlier reports, which indicate that the inclusion of bromide largely reduces the PL lifetime.[158] In a similar fashion, mp-NiO/$FA_{0.83}Cs_{0.17}Pb(I_{0.6}Br_{0.4})_3$ has a largest bromide ratio though, the segregated iodide-rich region causes additional charge trappings and recombination, leading to a smaller k_2.[157] These results suggest that, when phase segregation is properly controlled, a larger VB offset at mp-NiO/perovskite interface is beneficial for assisting hole extraction.

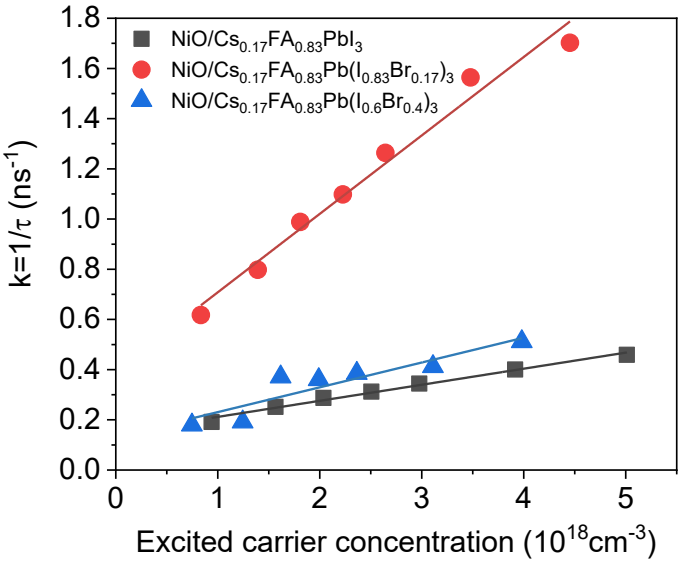

Figure 45. The relationship between excited carrier concentration and the apparent rate constant (k) for three samples. Adapted from ref[154].

Table 11. Fitting results of average rate constant (k) versus excitation concentration (N) linear

relationship. Reproduced from ref[154].

	k_1 (ns^{-1})	t_1 (ns)	k_2 (ns^{-1})	t_2 (ns)
$Cs_{0.17}FA_{0.83}PbI_3$	0.15	6.67	0.06	16.67
$Cs_{0.17}FA_{0.83}Pb(I_{0.83}Br_{0.17})_3$	0.40	2.50	0.31	3.23
$Cs_{0.17}FA_{0.83}Pb(I_{0.6}Br_{0.4})_3$	0.13	7.69	0.10	10

4.4 The effect of electrical bias on the kinetics of hole extraction in mp-NiO/perovskite bilayers

4.4.1 Establishing the electrochemical stability window

The previous sections focused on a "static interface", in which charge extraction takes place without the application of an external electrical bias. To monitor the effect of electrical bias on the charge extraction process, in-situ transient spectroelectrochemistry[118,126] measurements were carried out. As the first step, the stability window of mp-NiO/$FA_{0.83}Cs_{0.17}PbI_3$ and mp-NiO/$FA_{0.83}Cs_{0.17}Pb(I_{0.83}Br_{0.17})_3$ samples was established by spectroelectrochemical measurements (**Figure 46 and 47)**. The mp-NiO/$FA_{0.83}Cs_{0.17}Pb(I_{0.6}Br_{0.4})_3$ sample was not included in this section because of its segregation even without the use of an electrolyte. Both samples exhibited three redox waves in the anodic scan, agree with previous results (**Figure 46A and 46C**).[125] The first oxidative waves (+0.63 V vs Ag/AgCl for mp-NiO/$FA_{0.83}Cs_{0.17}PbI_3$, and +0.73 V vs Ag/AgCl for mp-NiO/$FA_{0.83}Cs_{0.17}Pb(I_{0.83}Br_{0.17})_3$) are attributed to hole trapping and iodide ion movement inside the perovskite lattice. The second oxidative waves (+1.05 V vs Ag/AgCl for mp-NiO/$FA_{0.83}Cs_{0.17}PbI_3$, and +1.18 V vs Ag/AgCl mp-NiO/$FA_{0.83}Cs_{0.17}Pb(I_{0.83}Br_{0.17})_3$) are the result of direct hole injection into the VB of the perovskite. This process causes iodide expulsion from the lattice and leads to absorbance loss (**Figure 46B and 46D**). Therefore, the position of this oxidative wave indicates VB position.[125] A 0.13 V shift in the second oxidative wave from mp-NiO/$FA_{0.83}Cs_{0.17}PbI_3$ to mp-NiO/$FA_{0.83}Cs_{0.17}Pb(I_{0.83}Br_{0.17})_3$ matches well with the APS results. The only reductive wave (−1.50 V vs Ag/AgCl for both mp-NiO/$FA_{0.83}Cs_{0.17}PbI_3$ and mp-NiO/$FA_{0.83}Cs_{0.17}Pb(I_{0.83}Br_{0.17})_3$) in cathodic scan is

attributed to the reduction of Pb^{2+} to Pb (**Figure 47A and 47C**), accompanied by an absorbance loss (**Figure 47B and 47D**).[125] For both perovskite composition samples, a stability potential window of −0.5 to 0.5 V vs Ag/AgCl was determined.

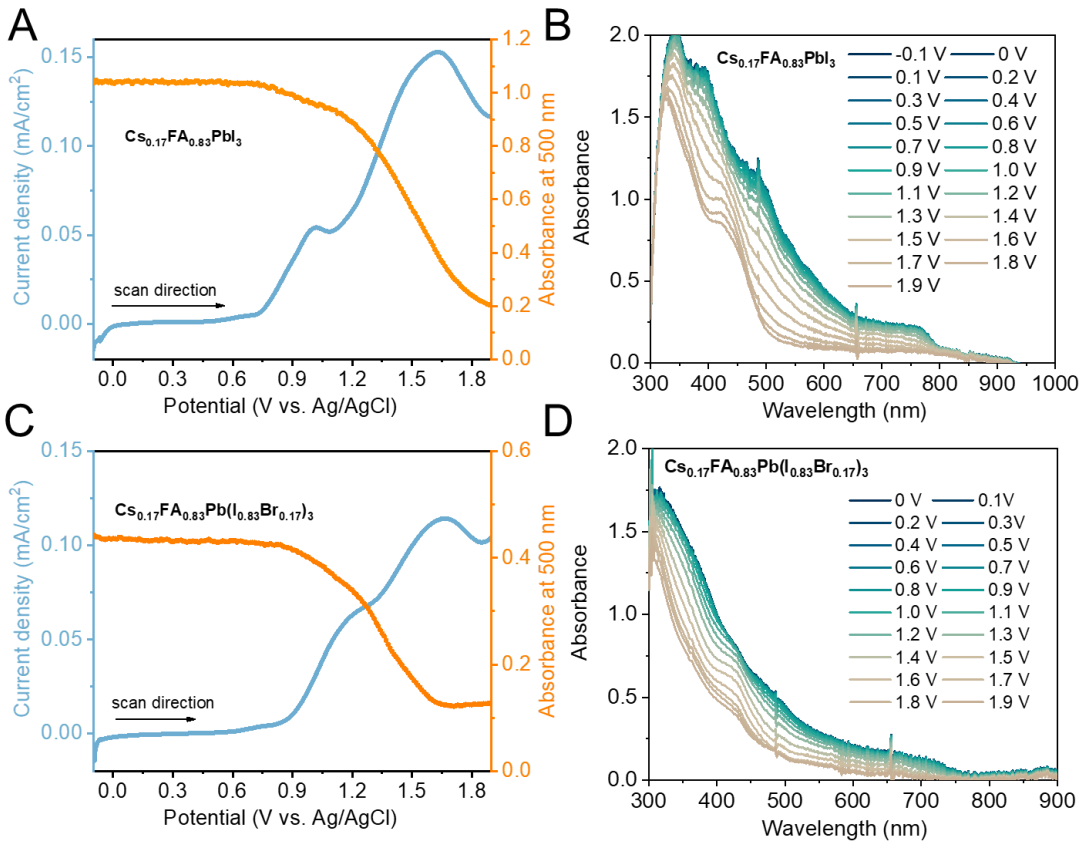

Figure 46. Spectroelectrochemical measurement, where the electrochemical traces are shown together with the absorbance change monitored at 500 nm during the anodic scan for mp-$NiO/FA_{0.83}Cs_{0.17}PbI_3$ (A) and mp-$NiO/FA_{0.83}Cs_{0.17}Pb(I_{0.83}Br_{0.17})_3$ (C) samples. Absorption spectra of mp-$NiO/FA_{0.83}Cs_{0.17}PbI_3$ (B) and mp-$NiO/FA_{0.83}Cs_{0.17}Pb(I_{0.83}Br_{0.17})_3$ (D) at electrochemical anodic scan at various potentials. Electrolyte: 0.01 M Bu_4NPF_6/dichloromethane, sweep rate: 10 mV s^{-1}. Adapted from ref[154].

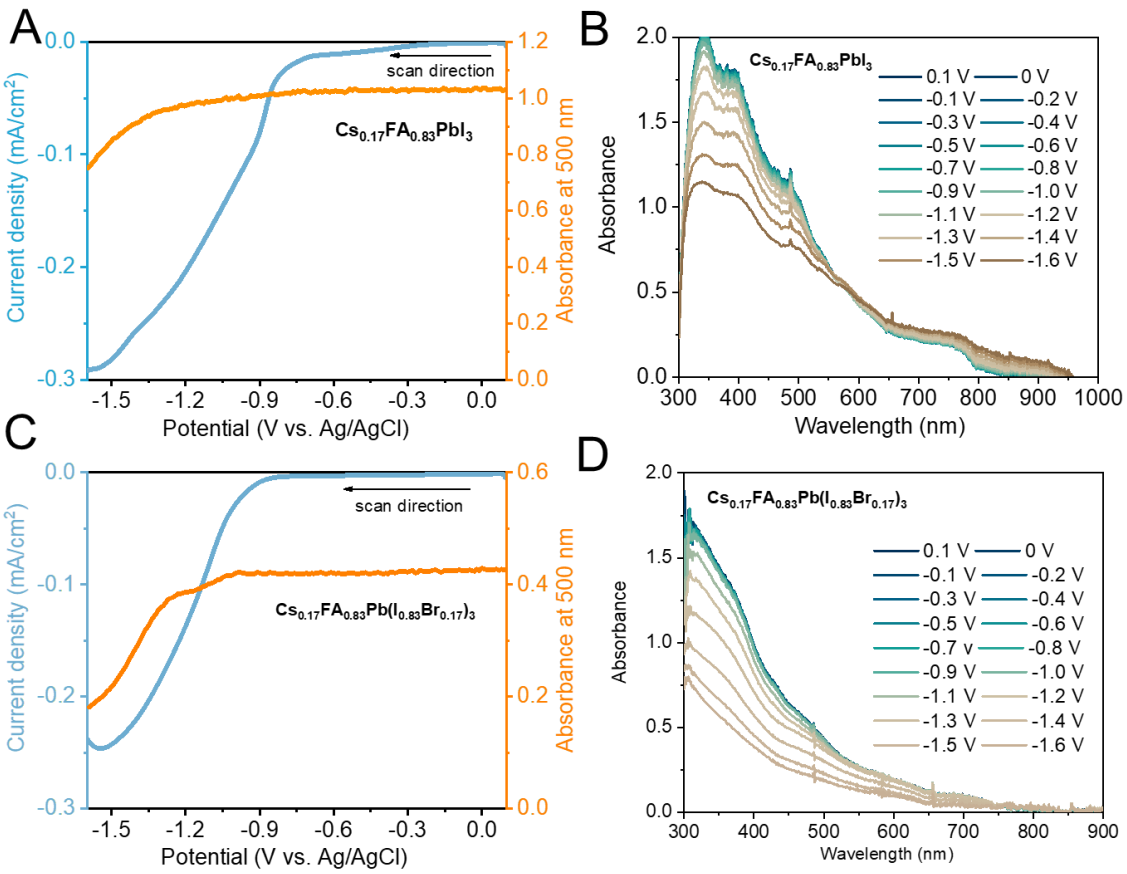

Figure 47. Spectroelectrochemical measurement, where the electrochemical traces are shown together with the absorbance change monitored at 500 nm during the cathodic scan for mp-NiO/$FA_{0.83}Cs_{0.17}PbI_3$ (A) and mp-NiO/$FA_{0.83}Cs_{0.17}Pb(I_{0.83}Br_{0.17})_3$ (C) samples. Absorption spectra of mp-NiO/$FA_{0.83}Cs_{0.17}PbI_3$ (B) and mp-NiO/$FA_{0.83}Cs_{0.17}Pb(I_{0.83}Br_{0.17})_3$ (D) at electrochemical cathodic scan at various potentials. Electrolyte: 0.01 M Bu_4NPF_6/dichloromethane, sweep rate: 10 mV s^{-1}. Adapted from ref[154].

To examine the long-term stability of the samples, further spectroelectrochemistry measurements were carried out inside the stability window, where the samples were subjected to constant potential cycling for 4000s with 10 mV s^{-1}. No obvious current and absorbance change were seen for both mp-NiO/$FA_{0.83}Cs_{0.17}PbI_3$ and mp-NiO/$FA_{0.83}Cs_{0.17}Pb(I_{0.83}Br_{0.17})_3$ samples during the whole process, indicating good stability (**Figure 48**).

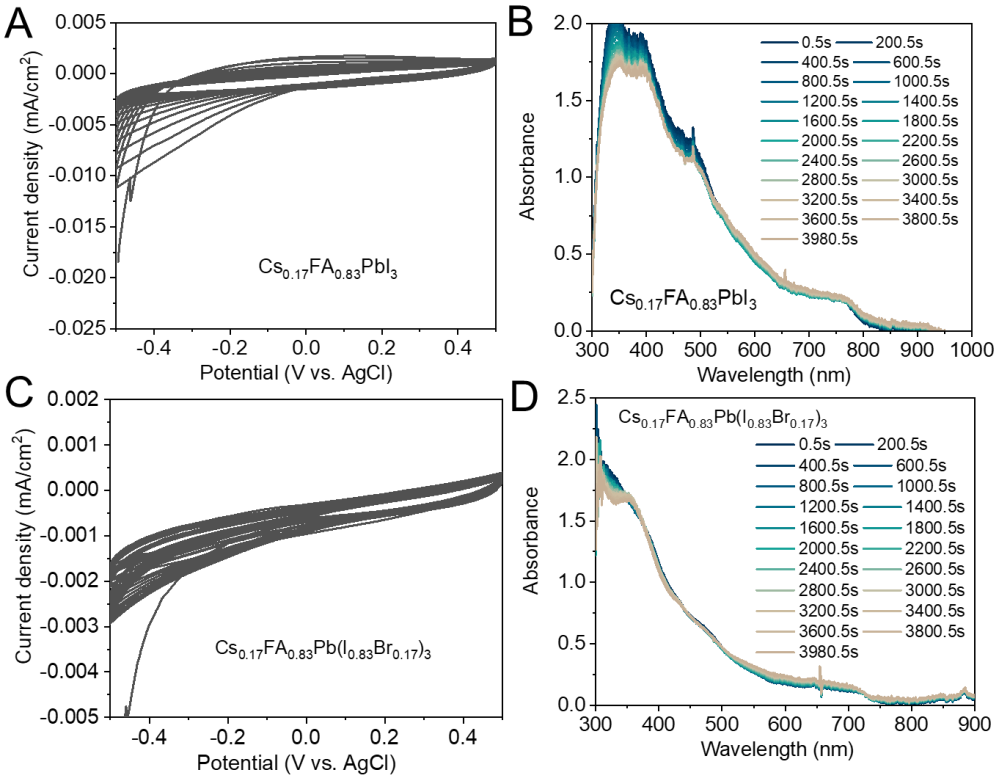

Figure 48. Spectroelectrochemical stability tests for both mp-NiO/perovskite samples inside the proposed stability window. Cyclic voltammetries (CVs) (A) and absorption spectra during CV measurements (B) for mp-NiO/$FA_{0.83}Cs_{0.17}PbI_3$. CVs (C) and absorption spectra during CV measurements (D) for mp-NiO/$FA_{0.83}Cs_{0.17}Pb(I_{0.83}Br_{0.17})_3$. Electrolyte: 0.01 M Bu_4NPF_6/dichloromethane, scan rate: 10 mV s^{-1}. Adapted from ref[154].

Furthermore, to assess the role of mp-NiO in the spectroelectrochemical results, we also conducted measurements for bare mp-NiO samples (**Figure 49**). The resulting current density and absorbance changes were lower compared to those of the mp-NiO/perovskite layers, which confirm that the redox peaks observed in **Figure 46 and 47** are mainly related to the electrochemical alterations of the perovskite layers.

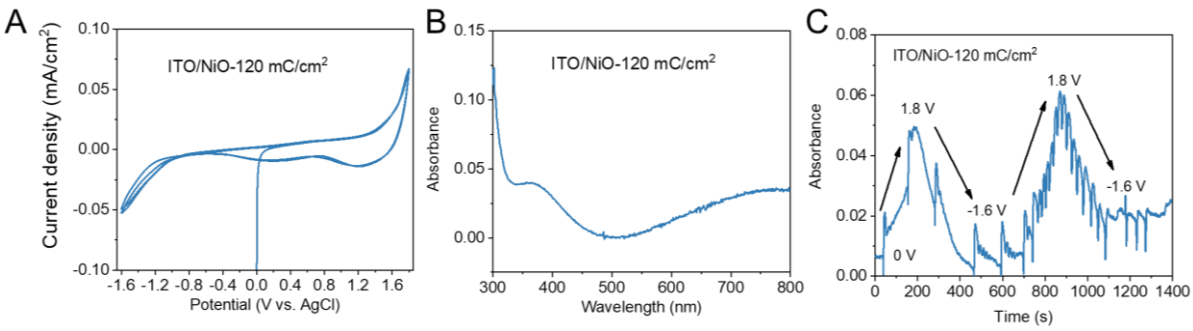

Figure 49. CVs (A), absorption spectra (B) and absorbance change at 500 nm during CV

measurements (C) for pure ITO/mp-NiO. Electrolyte: 0.01 M Bu_4NPF_6/DCM, scan rate: 10 mV s^{-1}. Adapted from ref[154].

4.4.2 Effect of electrochemical bias on the hole extraction process in mp-NiO/perovskite bilayers

To investigate the influence of the electrochemical bias on the hole extraction process, in-situ transient spectroelectrochemical measurements were performed within the electrochemical stability window. As the first step, the reproducibility of the excited state recovery of the samples was determined at the same spot at the open circuit potential (515 nm excitation, laser fluence: 16 μJ/cm^2) with three consecutive measurements (**Figure 50 A** and **C**). For both samples, the three decay traces were almost identical (**Figure 50 B** and **D**). Compared to the decay traces measured without electrolyte, slightly faster decay kinetic was observed for both samples when immersed in the electrolyte (**Figure 50B** and **50D**) as the result of the formation of the electrical double layer on the sample surface (accelerates charge recombination).

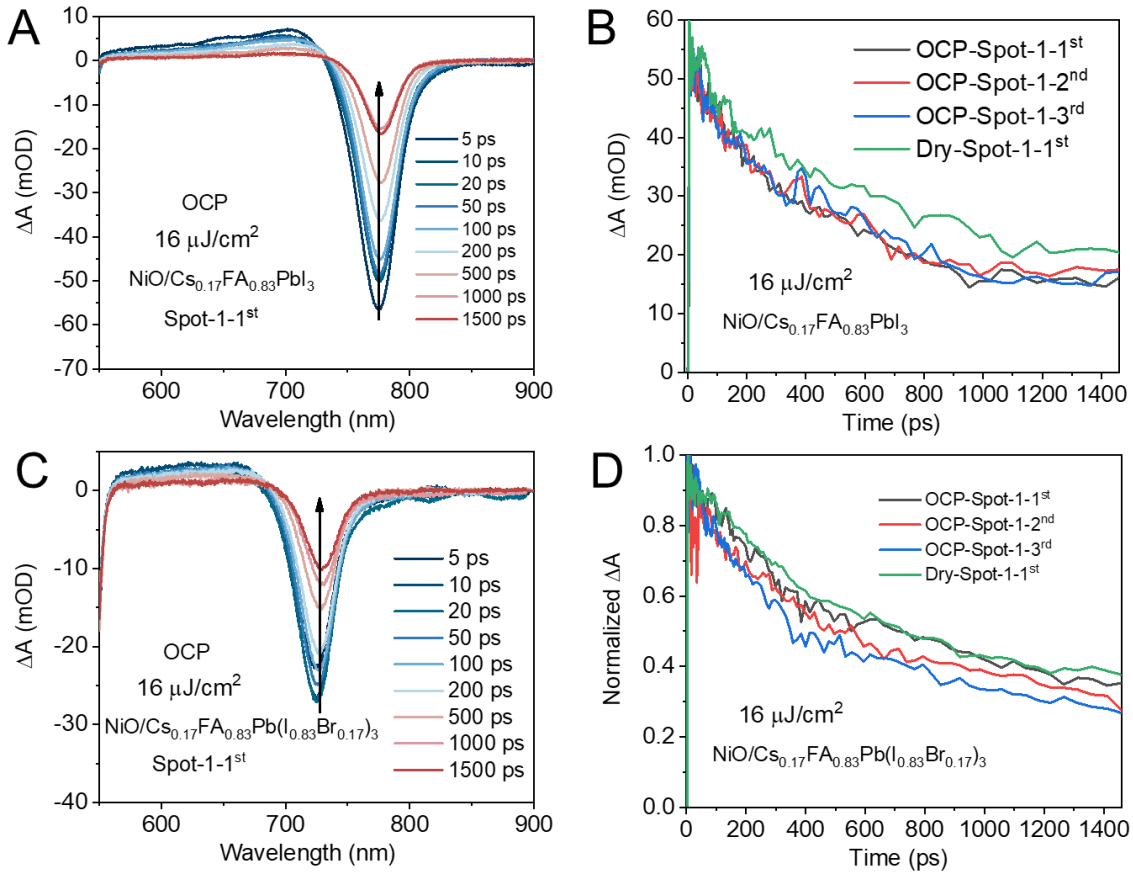

Figure 50. TA measurements of mp-NiO/$FA_{0.83}Cs_{0.17}PbI_3$ and mp-NiO/$FA_{0.83}Cs_{0.17}Pb(I_{0.83}Br_{0.17})_3$ with electrolyte at open circuit potential (0.3 V vs. Ag/AgCl) were carried out three times at the same spot. TA spectra at various delay times at open circuit potential for mp-NiO/$FA_{0.83}Cs_{0.17}PbI_3$ (A) and mp-NiO/$FA_{0.83}Cs_{0.17}Pb(I_{0.83}Br_{0.17})_3$ (C) (first measurement). Decay kinetics at GSB maximum of the three measurements at open circuit potential compared to that measured without electrolyte for mp-NiO/$FA_{0.83}Cs_{0.17}PbI_3$ (B) and mp-NiO/$FA_{0.83}Cs_{0.17}Pb(I_{0.83}Br_{0.17})_3$ (D). Electrolyte: 0.01 M Bu_4NPF_6/DCM, laser fluence: 16 μJ/cm^2. Adapted from ref[154].

As the next step, electrochemical bias inside the stability window was added during transient spectroelectrochemical measurements. To check the reversibility of the influence of applied bias to charge dynamics, the GSB decay traces were monitored at 0.4 to −0.4 and then back to 0.4 V vs Ag/AgCl at the excitation fluence of 19 μJ/cm^2 (**Figure 51A** and **Figure 52A**). To investigate the influence of excitation fluence on the effect of applied bias, GSB decay traces were also recorded at potentials of −0.4, 0 and +0.4 V vs Ag/AgCl at various excitation fluences for both samples (**Figure 51B-D** and **Figure 52B-D**). Similarly, all decay traces were fitted by multi exponential functions, and the fitting details, calculated average lifetime and apparent rate constant (k) were summarized in **Appendix Tables A6, A7, A8, A9, A10,**

A11, A12, and A13.

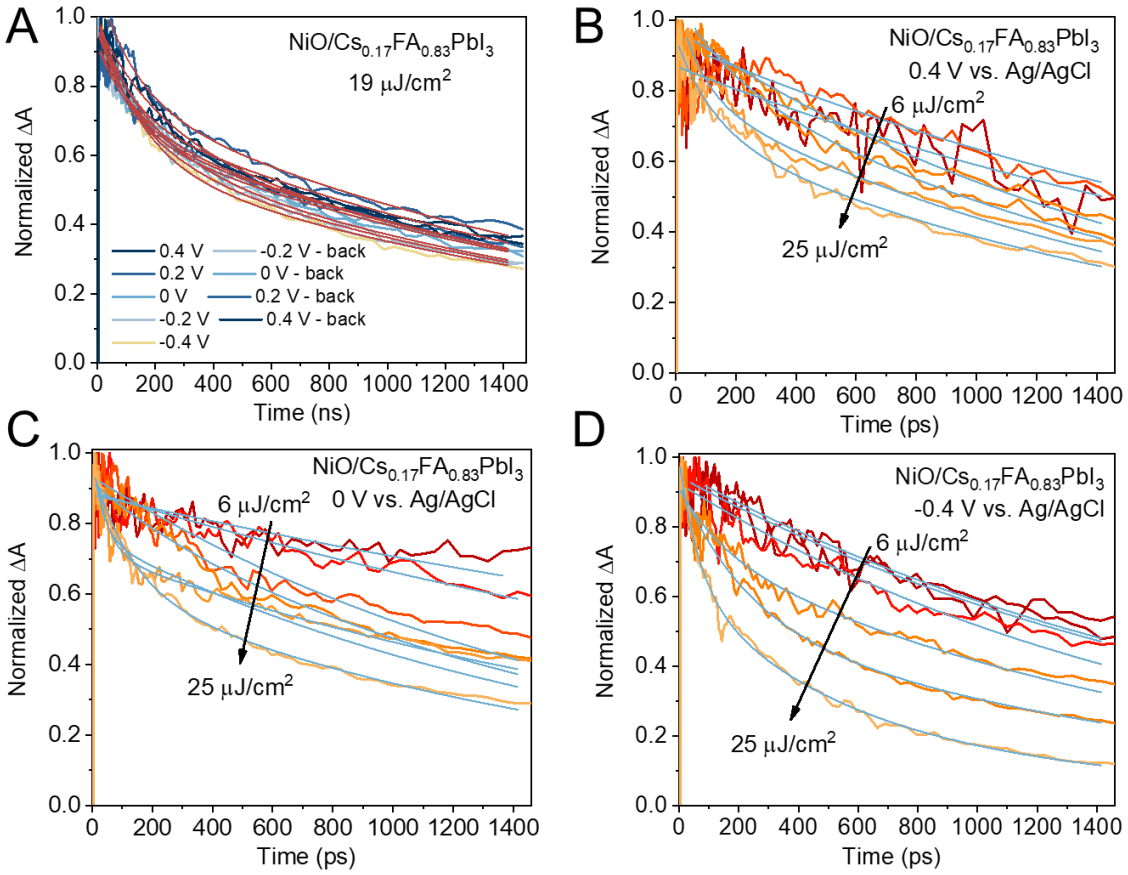

Figure 51. Normalized decay kinetics of mp-NiO/$FA_{0.83}Cs_{0.17}PbI_3$ at GSB maximum from 0.4 V vs. Ag/AgCl to -0.4 V vs. Ag/AgCl and back to 0.4 V vs. Ag/AgCl at excitation fluence of 19 μJ/cm^2 to check reversibility (A). Normalized decay kinetics of mp-NiO/$FA_{0.83}Cs_{0.17}PbI_3$ at GSB maximum at applied potential of 0.4 V vs. Ag/AgCl (B), 0 V vs. Ag/AgCl (C), and -0.4 V vs. Ag/AgCl (D) at various excitation fluence. Electrolyte: 0.01 M Bu_4NPF_6/dichloromethane, excitation wavelength: 515 nm. Adapted from ref[154].

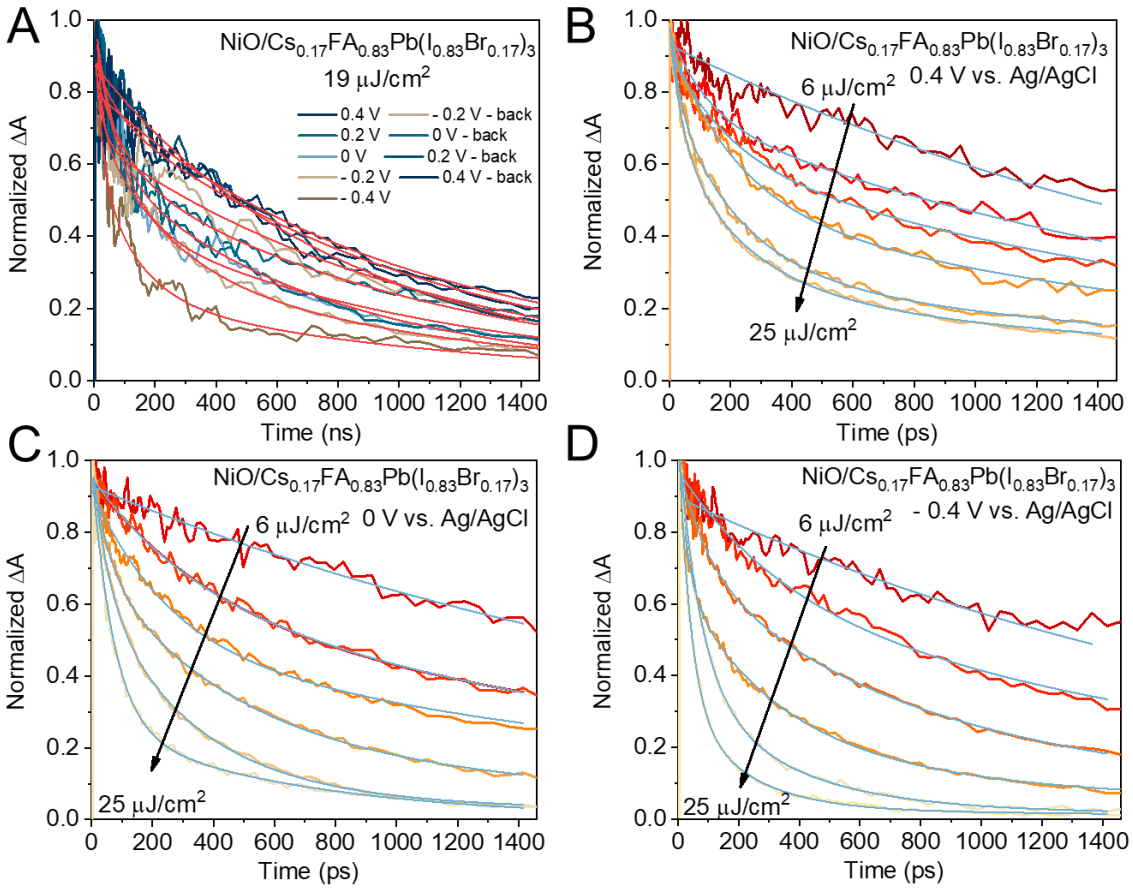

Figure 52. Normalized decay kinetics of mp-NiO/$FA_{0.83}Cs_{0.17}Pb(I_{0.83}Br_{0.17})_3$ at GSB maximum from 0.4 V vs. Ag/AgCl to -0.4 V vs. Ag/AgCl and back to 0.4 V vs. Ag/AgCl at excitation fluence of 19 μJ/cm^2 to check reversibility (A). Normalized decay kinetics of mp-NiO/$FA_{0.83}Cs_{0.17}Pb(I_{0.83}Br_{0.17})_3$ at GSB maximum at applied potential of 0.4 V vs. Ag/AgCl (B), 0 V vs. Ag/AgCl (C), and -0.4 V vs. Ag/AgCl (D) at various excitation fluence. Electrolyte: 0.01 M Bu_4NPF_6/dichloromethane, excitation wavelength: 515 nm. Adapted from ref[154].

The determined k values were plotted versus different excited carrier concentrations at all applied potentials (**Figure 53A** and **53B**). Notably, by applying a negative potential, the GSB relaxation kinetics can be accelerated (larger k). The applied bias alters the Fermi level of the materials, thereby affecting the hole extraction process from the perovskite to the mp-NiO.[118] However, this acceleration was only observed at high carrier concentrations and only negligible effects were observed at low carrier concentrations. Due to this non-linear dependence on carrier concentration, the previous used separation method for the first and the second order processes were not applicable. These results also indicate that the built-in potential at mp-NiO/perovskite interface is sufficient to assist hole transfer at low excited

carrier concentrations. On the contrary, when high excitation fluence was applied, higher carrier concentration was generated, the applied negative potential became effective in accelerating hole transfer at the interface. Interestingly, this effect of the negative bias in accelerating the GSB decay kinetics was more pronounced for mp-NiO/$FA_{0.83}Cs_{0.17}Pb(I_{0.83}Br_{0.17})_3$ (~6 times), compared to that for mp-NiO/$FA_{0.83}Cs_{0.17}PbI_3$ (~1.5 times). This suggests that the electrochemical bias has a more significant impact on the interfaces which have a larger band offset. To confirm that no chemical changes took place during the measurements, reversibility tests at the excitation fluence of 19 μJ/cm^2 was conducted (**Figure 53C** and **53D**). Both samples demonstrated good reversibility with an accelerated GSB decay kinetic at negative potentials.

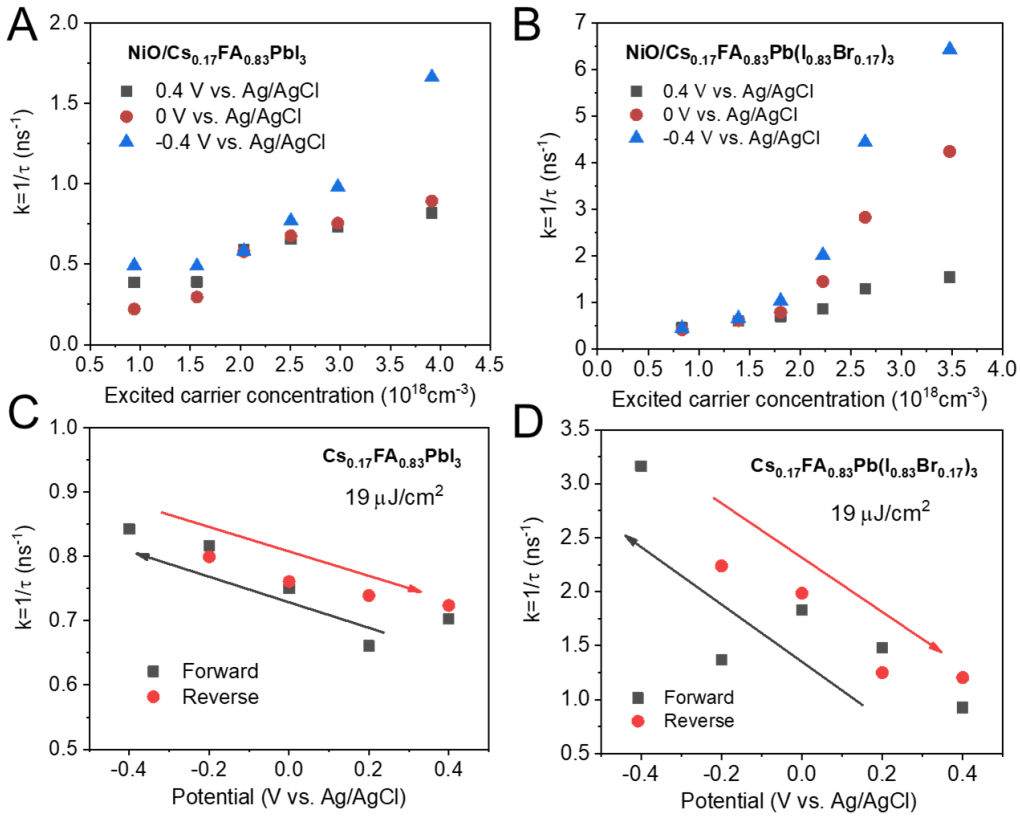

Figure 53. The effect of electrochemical bias on the apparent rate constant of mp-NiO/$FA_{0.83}Cs_{0.17}PbI_3$ (A) and mp-NiO/$FA_{0.83}Cs_{0.17}Pb(I_{0.83}Br_{0.17})_3$ (B) at different excited carrier concentrations. Reversibility test of the apparent rate constant of mp-NiO/$FA_{0.83}Cs_{0.17}PbI_3$ (C) and mp-NiO/$FA_{0.83}Cs_{0.17}Pb(I_{0.83}Br_{0.17})_3$ (D) at the excitation fluence of 19 μJ/cm^2. Electrolyte: 0.01 M Bu_4NPF_6/dichloromethane, excitation wavelength: 515 nm. Reproduced from ref[154].

To check if the applied bias has an influence on band broadening, the normalized FWHM was examined at 0.4 ps, 5 ps and 1 ns (**Figure 54**). No notable differences were seen on the normalized FWHM at different applied potentials. This result suggests that the applied bias does not affect carrier distribution and band renormalization processes.

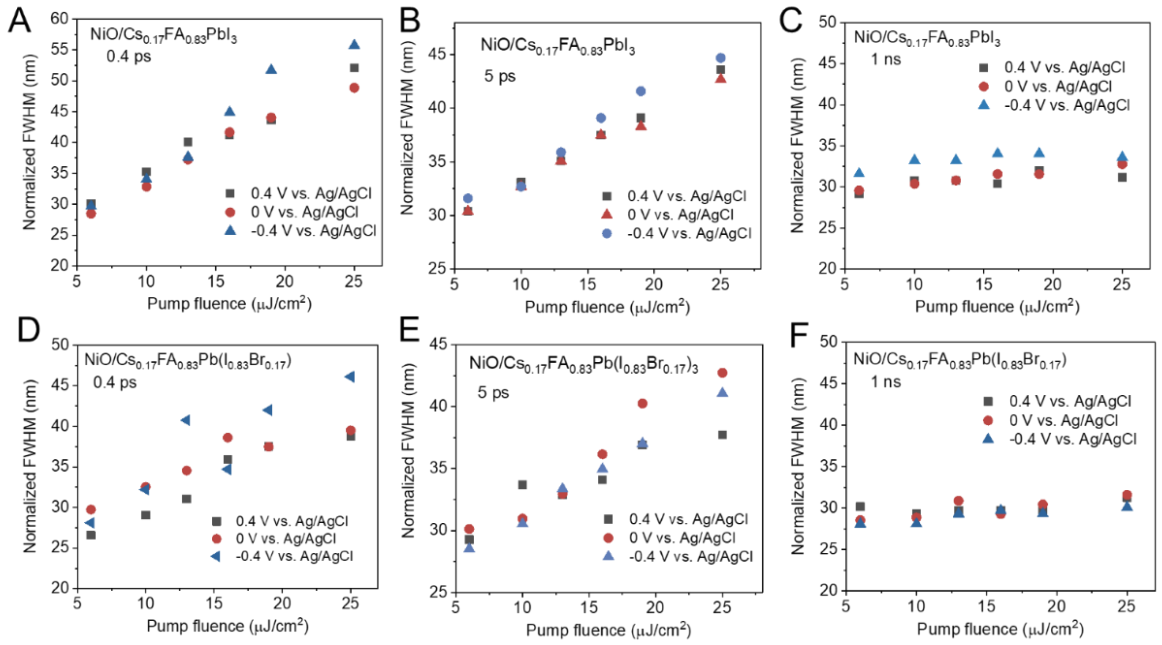

Figure 54. The normalized FWHM of the GSB spectra at 0.4 ps (A), 5 ps (B) and 1 ns (C) at various excitation fluences for mp-NiO/$FA_{0.83}Cs_{0.17}PbI_3$. The normalized FWHM of the GSB spectra at 0.4 ps (D), 5 ps (E) and 1 ns (F) at various excitation fluences for mp-NiO/$FA_{0.83}Cs_{0.17}Pb(I_{0.83}Br_{0.17})_3$. Reproduced from ref[154].

From the previous measurements a schematic energy diagram was summarized to help understand the impact of the applied electrochemical bias on the hole transfer process at the mp-NiO/perovskite interface (**Figure 55**). Applying a positive bias injects holes into the mp-NiO (lowering the Fermi level). This process suppresses hole transfer from the perovskite layer to mp-NiO (**Figure 55A, C**). In this case, band-to-band recombination is dominant in dictating the charge carrier dynamics of these systems. On the contrary, applying a negative bias depletes holes in the mp-NiO layer (elevating the Fermi-level), which assists hole transfer from perovskite to mp-NiO (**Figure 55B, D**). In this case, hole transfer dominates the charge carrier decay kinetics, resulting in a large k value. Comparing the two perovskite compositions can illustrate the role of VB offset in the effect of applied bias on hole transfer

processes. When the VB offset at the interface is large, the effect of applied potential is more significant on hole transfer processes (**Figure 55D**). Conversely, when a smaller VB offset is present, the applied potential still plays a role in assisting hole transfer, but with a much weaker effect (**Figure 55B)**.

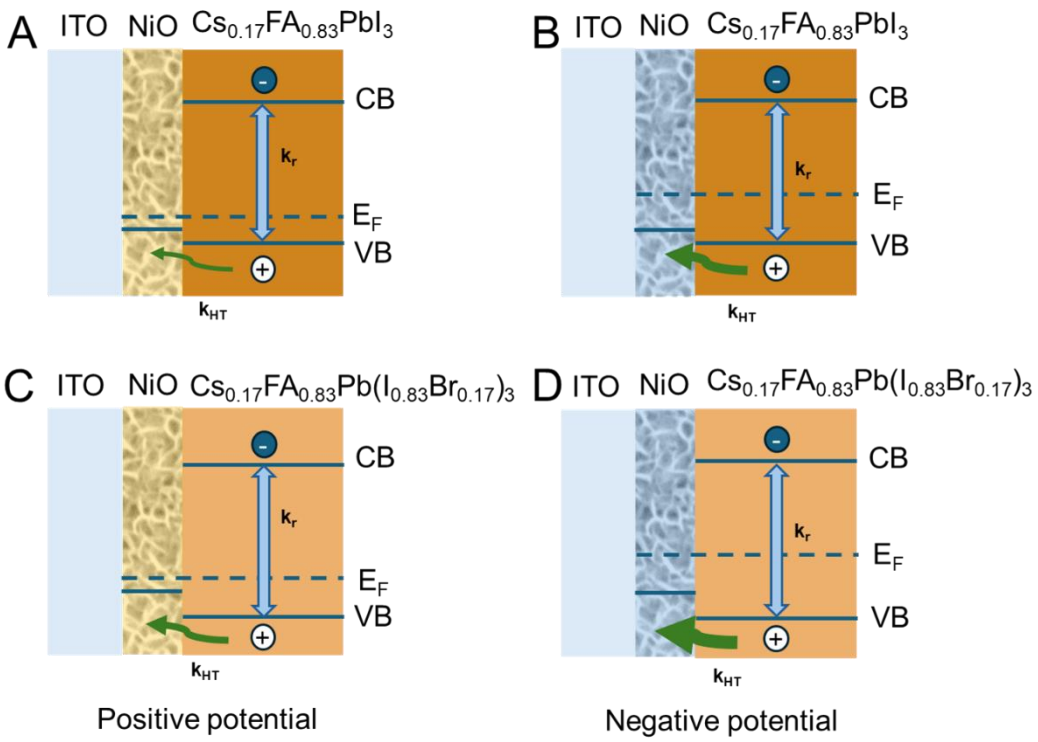

Figure 55. Schematic diagram showing how band offset (A, C) and electrochemical bias (A-B and C-D respectively) affect charge carrier dynamics at mp-NiO/perovskite interface, where k_{HT} represents hole transfer process and k_r represents band-to-band recombination process. Reproduced from ref[154].

5. Summary

Ultrafast spectroscopic techniques (e.g. TA and TRPL) can be powerful tools to monitor the charge dynamics in PSCs. However, many different aspects, such as sample properties, measurement parameters, and evaluation protocols, can lead to large variation in the obtained results. We proposed guidelines for such measurements to minimize the variation and facilitate comparable results. Following these guidelines, we investigated how different energy offsets at the interfaces of CTL/perovskite influence charge transfer dynamics. TiO_2 single crystal of different orientations, which exhibiting different CB levels, were employed as ETL. The effect of the employed excitation fluence on the electron transfer process revealed a convoluted photophysical picture where charge accumulation processes also played a role. Using mp-NiO as a HTL, we also monitored the hole transfer process while varying the composition of perovskite. To reveal the effect of electric bias on charge dynamics, in-situ transient spectroelectrochemistry was carried out.

The key findings of the dissertation are outlined as follows:

1. Different sample properties and measurement parameters lead to a large dispersion (from 0.8 ps to 100 ns) of the reported charge transfer rates (determined by time-resolved techniques) in the literature for various charge transfer layer/perovskite interfaces (e.g. TiO_2/perovskite). We summarized reported charge transfer rates at different charge transfer layer/perovskite interfaces according to the used time-resolved techniques (TA or TRPL), used electron transfer layers (TiO_2, PCBM) and used hole transfer layers (Spiro). We concluded that this is influenced not only by the sample properties (e.g., the type of ETL and HTL) but also by other factors, including perovskite layer thickness, excitation wavelength and fluence, and the evaluation methods used.
2. Apart from sample properties and the specific measurement conditions, the kinetic analysis used to interpret the transient decay has a large contribution in the observed dispersion of charge transfer rates. Different methods which are used frequently in the literature, were evaluated on the same dataset for both TA and TRPL measurements. After multiexponential fitting of the decay traces the charge transfer rate constant was extracted from (i) as one of the exponents from the multi-exponential fits, (ii) by solving

the charge transfer equation or (iii) as the exponent of a stretched exponential fits. By using these methods different charge extraction rate constanst were obtained (0.2- 14.1 ns), that we could link to be one of the causes behind the dispersion in the literature.

3. The energy offset at the interface between SC TiO_2 (with specific orientations) and lead-halide perovskite significantly influences the electron extraction rate from the perovskite to TiO_2. While TiO_2 single crystals of different orientations exhibit distinct CB energy levels, their surface properties remain similar. UPS and APS measurements were employed to determine the VB position of single crystal TiO_2 and perovskite. UV vis absorbance spectra and Tauc analysis revealed the bandgap of single crystal TiO_2 and perovskite, allowing us to calculate the corresponding CB positions. A larger CB offset (ΔE = 1.0) at the TiO_2 (100)/perovskite and TiO_2 (111)/perovskite interfaces can be observed compared to the offset at the TiO_2 (110)/perovskite interface (ΔE = 0.4) Time resolved photoluminescence results reveal electron extraction kinetic is faster at the single crystal TiO_2/perovskite interface with larger CB offset ((100) and (111)), and it is slower at the interface with smaller band offset (110).
4. We demonstrated the presence of an electrical barrier at the interface of TiO_2/perovskite, which can be overcome by increasing the excitation fluence. At low excitation fluence (0.7, 2.8 $\mu J/cm^2$), the decay kinetics of all three single crystal TiO_2/perovskite are the same with that of glass/perovskite sample, indicating the absence of charge transfer. When the excitation fluence is increased to 5.7 $\mu J/cm^2$, the recovery of the excited state of single crystal TiO_2/perovskite start to deviate from that of glass/perovskite samples, indicating electron accumulation at the interface that can overcome the electrical barrier and initiate electron transfer.
5. The overall kinetics of the electron extraction (ns timescale – free charge carriers) at the TiO_2/perovskite interface strongly depends on the early extraction processes (ps timescale - hot-carriers). TA spectroscopy data (ps range) reveals hot carrier extraction is faster at interfaces with a larger band offset (100). This results in a relatively high concentration of electrons in the CB of TiO_2 (100) after 1 ps, which can bottleneck longer timescale electron extraction, leading to slow electron extraction in the time range of 1-

6 ns at this TiO_2 orientation (TA results). In longer timescales (TRPL results (in the time range of ~300 ns)), when the electrons can be removed from the CB of TiO_2 efficient band edge electron extraction can be achieved by the TiO_2 (100) facet again.

6. The VB energy offset affects the hole transfer process at mp-NiO/perovskite interface. By incorporating different ratio of bromide into $FA_{0.83}Cs_{0.17}PbI_3$ ($FA_{0.83}Cs_{0.17}Pb(I_{0.83}Br_{0.17})_3$ and $FA_{0.83}Cs_{0.17}Pb(I_{0.6}Br_{0.4})_3$), the VB of perovskite can be lowered, creating a larger VB offset at mp-NiO/perovskite interface. Excitation fluence dependent TA measurements revealed that a larger VB offset can accelerate hole transfer process when segregation was kept under control.
7. The electrochemical stability window of lead-halide perovskites ($FA_{0.83}Cs_{0.17}PbI_3$ and $FA_{0.83}Cs_{0.17}Pb(I_{0.83}Br_{0.17})_3$) was determined by spectroelectrochemical measurements. Results revealed multiple redox events coupled to distinct absorbance changes of the layers outside the stability window. Ultimately, a stability window of −0.5 V – +0.5 V vs Ag/AgCl was determined for both $FA_{0.83}Cs_{0.17}PbI_3$ and $FA_{0.83}Cs_{0.17}Pb(I_{0.83}Br_{0.17})_3$, in which the material can stay stable for more than 4000 seconds under continuous cycling.
8. Transient spectroelectrochemical measurements were used to probe the dependence of applied electrochemical bias on the rate of hole transfer at the mp-NiO/perovskite interface. Results revealed that applying a negative electrochemical bias can accelerate hole transfer process from perovskite layer to mp-NiO, by depleting the holes in mp-NiO layer (i.e. increase the Fermi level). In contrast, applying a positive bias injects holes into mp-NiO (i.e. lowering the Fermi level), thus suppresses hole transfer process at the interface. Furthermore, this effect of electrochemical bias was observed to be more pronounced at the mp-NiO/pervskite interface with a larger VB offset.

References

(1) Noman, M.; Khan, Z.; Jan, S. T. A Comprehensive Review on the Advancements and Challenges in Perovskite Solar Cell Technology. *RSC Adv.* **2024**, *14* (8), 5085–5131. https://doi.org/10.1039/D3RA07518D.

(2) Li, G.; Su, Z.; Canil, L.; Hughes, D.; Aldamasy, M. H.; Dagar, J.; Trofimov, S.; Wang, L.; Zuo, W.; Jerónimo-Rendon, J. J.; Byranvand, M. M.; Wang, C.; Zhu, R.; Zhang, Z.; Yang, F.; Nasti, G.; Naydenov, B.; Tsoi, W. C.; Li, Z.; Gao, X.; Wang, Z.; Jia, Y.; Unger, E.; Saliba, M.; Li, M.; Abate, A. Highly Efficient P-i-n Perovskite Solar Cells That Endure Temperature Variations. *Science* **2023**, *379* (6630), 399–403. https://doi.org/10.1126/science.add7331.

(3) Cho, H.; Jeong, S.-H.; Park, M.-H.; Kim, Y.-H.; Wolf, C.; Lee, C.-L.; Heo, J. H.; Sadhanala, A.; Myoung, N.; Yoo, S.; Im, S. H.; Friend, R. H.; Lee, T.-W. Overcoming the Electroluminescence Efficiency Limitations of Perovskite Light-Emitting Diodes. *Science* **2015**, *350* (6265), 1222–1225. https://doi.org/10.1126/science.aad1818.

(4) Liu, C.; Tai, Q.; Wang, N.; Tang, G.; Loi, H.; Yan, F. Sn-Based Perovskite for Highly Sensitive Photodetectors. *Adv. Sci.* **2019**, *6* (17). https://doi.org/10.1002/advs.201900751.

(5) Moon, J.; Mehta, Y.; Gundogdu, K.; So, F.; Gu, Q. Metal-Halide Perovskite Lasers: Cavity Formation and Emission Characteristics. *Adv. Mater.* **2024**, *36* (20). https://doi.org/10.1002/adma.202211284.

(6) Zheng, Y.; Li, Y.; Zhuang, R.; Wu, X.; Tian, C.; Sun, A.; Chen, C.; Guo, Y.; Hua, Y.; Meng, K.; Wu, K.; Chen, C.-C. Towards 26% Efficiency in Inverted Perovskite Solar Cells *via* Interfacial Flipped Band Bending and Suppressed Deep-Level Traps. *Energy Environ. Sci.* **2024**, *17* (3), 1153–1162. https://doi.org/10.1039/D3EE03435F.

(7) Brinkmann, K. O.; Wang, P.; Lang, F.; Li, W.; Guo, X.; Zimmermann, F.; Olthof, S.; Neher, D.; Hou, Y.; Stolterfoht, M.; Wang, T.; Djurišić, A. B.; Riedl, T. Perovskite–Organic Tandem Solar Cells. *Nat. Rev. Mater.* **2024**, *9* (3), 202–217. https://doi.org/10.1038/s41578-023-00642-1.

(8) Tian, R.; Zhou, S.; Meng, Y.; Liu, C.; Ge, Z. Material and Device Design of Flexible Perovskite Solar Cells for Next-Generation Power Supplies. *Adv. Mater.* **2024**, *36* (37). https://doi.org/10.1002/adma.202311473.

(9) NREL. *Best Research-Cell Efficiency Chart*. https://www.nrel.gov/pv/cell-efficiency.html.

(10) Xu, W.; Hart, L. J. F.; Moss, B.; Caprioglio, P.; Macdonald, T. J.; Furlan, F.; Panidi, J.; Oliver, R. D. J.; Pacalaj, R. A.; Heeney, M.; Gasparini, N.; Snaith, H. J.; Barnes, P. R. F.; Durrant, J. R. Impact of Interface Energetic Alignment and Mobile Ions on Charge Carrier Accumulation and Extraction in P-i-n Perovskite Solar Cells. *Adv. Energy Mater.* **2023**, *13* (36). https://doi.org/10.1002/aenm.202301102.

(11) Kim, M.; Choi, I. woo; Choi, S. J.; Song, J. W.; Mo, S. I.; An, J. H.; Jo, Y.; Ahn, S. J.; Ahn, S. K.; Kim, G. H.; Kim, D. S. Enhanced Electrical Properties of Li-Salts Doped Mesoporous TiO2 in Perovskite Solar Cells. *Joule* **2021**, *5* (3), 659–672. https://doi.org/10.1016/j.joule.2021.02.007.

(12) Chen, X.; Pasanen, H. P.; Khan, R.; Tkachenko, N. V.; Janáky, C.; Samu, G. F. Effect of Single-Crystal TiO_2 /Perovskite Band Alignment on the Kinetics of Electron Extraction. *J. Phys. Chem. Lett.* **2024**, *15* (7), 2057–2065. https://doi.org/10.1021/acs.jpclett.3c03536.

(13) Cao, F.; Cheng, F.; Huang, X.; Dai, X.; Tang, Z.; Nie, S.; Yin, J.; Li, J.; Zheng, N.; Wu, B. Synergistic Effect between NiO_x and P3HT Enabling Efficient and Stable Hole Transport Pathways for Regular Perovskite Photovoltaics. *Adv. Funct. Mater.* **2022**, *32* (31).

https://doi.org/10.1002/adfm.202201423.

(14) Tan, C.; Xu, W.; Huan, Y.; Wu, B.; Qin, T.; Gao, D. Increasing Stability of SnO_2 -Based Perovskite Solar Cells by Introducing an Anionic Conjugated Polyelectrolyte for Interfacial Adjustment. *ACS Appl. Mater. Interfaces* **2021**, *13* (21), 24575–24581. https://doi.org/10.1021/acsami.1c00410.

(15) Zhu, W.; Zhang, Z.; Chai, W.; Zhang, Q.; Chen, D.; Lin, Z.; Chang, J.; Zhang, J.; Zhang, C.; Hao, Y. Band Alignment Engineering Towards High Efficiency Carbon-Based Inorganic Planar $CsPbIBr_2$ Perovskite Solar Cells. *ChemSusChem* **2019**, *12* (10), 2318–2325. https://doi.org/10.1002/cssc.201900611.

(16) Ou, Q.; Bao, X.; Zhang, Y.; Shao, H.; Xing, G.; Li, X.; Shao, L.; Bao, Q. Band Structure Engineering in Metal Halide Perovskite Nanostructures for Optoelectronic Applications. *Nano Materials Science* **2019**, *1* (4), 268–287. https://doi.org/10.1016/j.nanoms.2019.10.004.

(17) Bu, T.; Liu, X.; Zhou, Y.; Yi, J.; Huang, X.; Luo, L.; Xiao, J.; Ku, Z.; Peng, Y.; Huang, F.; Cheng, Y.-B.; Zhong, J. A Novel Quadruple-Cation Absorber for Universal Hysteresis Elimination for High Efficiency and Stable Perovskite Solar Cells. *Energy Environ. Sci.* **2017**, *10* (12), 2509–2515. https://doi.org/10.1039/C7EE02634J.

(18) Kojima, A.; Teshima, K.; Shirai, Y.; Miyasaka, T. Organometal Halide Perovskites as Visible-Light Sensitizers for Photovoltaic Cells. *J. Am. Chem. Soc.* **2009**, *131* (17), 6050–6051. https://doi.org/10.1021/ja809598r.

(19) Burschka, J.; Pellet, N.; Moon, S.-J.; Humphry-Baker, R.; Gao, P.; Nazeeruddin, M. K.; Grätzel, M. Sequential Deposition as a Route to High-Performance Perovskite-Sensitized Solar Cells. *Nature* **2013**, *499* (7458), 316–319. https://doi.org/10.1038/nature12340.

(20) Kim, H.-S.; Lee, C.-R.; Im, J.-H.; Lee, K.-B.; Moehl, T.; Marchioro, A.; Moon, S.-J.; Humphry-Baker, R.; Yum, J.-H.; Moser, J. E.; Grätzel, M.; Park, N.-G. Lead Iodide Perovskite Sensitized All-Solid-State Submicron Thin Film Mesoscopic Solar Cell with Efficiency Exceeding 9%. *Sci. Rep.* **2012**, *2* (1), 591. https://doi.org/10.1038/srep00591.

(21) Lee, M. M.; Teuscher, J.; Miyasaka, T.; Murakami, T. N.; Snaith, H. J. Efficient Hybrid Solar Cells Based on Meso-Superstructured Organometal Halide Perovskites. *Science* **2012**, *338* (6107), 643–647. https://doi.org/10.1126/science.1228604.

(22) Ball, J. M.; Lee, M. M.; Hey, A.; Snaith, H. J. Low-Temperature Processed Meso-Superstructured to Thin-Film Perovskite Solar Cells. *Energy Environ. Sci.* **2013**, *6* (6), 1739. https://doi.org/10.1039/c3ee40810h.

(23) Etgar, L.; Gao, P.; Xue, Z.; Peng, Q.; Chandiran, A. K.; Liu, B.; Nazeeruddin, Md. K.; Grätzel, M. Mesoscopic $CH_3NH_3PbI_3/TiO_2$ Heterojunction Solar Cells. *J. Am. Chem. Soc.* **2012**, *134* (42), 17396–17399. https://doi.org/10.1021/ja307789s.

(24) Sum, T. C.; Mathews, N. Advancements in Perovskite Solar Cells: Photophysics behind the Photovoltaics. *Energy Environ. Sci.* **2014**, *7* (8), 2518–2534. https://doi.org/10.1039/C4EE00673A.

(25) Padture, N. P. The Promise of Metal-Halide-Perovskite Solar Photovoltaics: A Brief Review. *MRS Bull* **2023**, *48* (10), 983–998. https://doi.org/10.1557/s43577-023-00585-6.

(26) Salim, T.; Sun, S.; Abe, Y.; Krishna, A.; Grimsdale, A. C.; Lam, Y. M. Perovskite-Based Solar Cells: Impact of Morphology and Device Architecture on Device Performance. *J. Mater. Chem. A Mater* **2015**, *3* (17), 8943–8969. https://doi.org/10.1039/C4TA05226A.

(27) Liu, S.; Biju, V. P.; Qi, Y.; Chen, W.; Liu, Z. Recent Progress in the Development of High-Efficiency Inverted Perovskite Solar Cells. *NPG Asia Mater.* **2023**, *15* (1), 27.

https://doi.org/10.1038/s41427-023-00474-z.

(28) Warby, J.; Shah, S.; Thiesbrummel, J.; Gutierrez-Partida, E.; Lai, H.; Alebachew, B.; Grischek, M.; Yang, F.; Lang, F.; Albrecht, S.; Fu, F.; Neher, D.; Stolterfoht, M. Mismatch of Quasi–Fermi Level Splitting and V_{oc} in Perovskite Solar Cells. *Adv Energy Mater* **2023**, *13* (48). https://doi.org/10.1002/aenm.202303135.

(29) Cho, A.-N.; Park, N.-G. Impact of Interfacial Layers in Perovskite Solar Cells. *ChemSusChem* **2017**, *10* (19), 3687–3704. https://doi.org/10.1002/cssc.201701095.

(30) Xiang, W.; Liu, S. (Frank); Tress, W. Interfaces and Interfacial Layers in Inorganic Perovskite Solar Cells. *Angewandte Chemie International Edition* **2021**, *60* (51), 26440–26453. https://doi.org/10.1002/anie.202108800.

(31) Stolterfoht, M.; Wolff, C. M.; Márquez, J. A.; Zhang, S.; Hages, C. J.; Rothhardt, D.; Albrecht, S.; Burn, P. L.; Meredith, P.; Unold, T.; Neher, D. Visualization and Suppression of Interfacial Recombination for High-Efficiency Large-Area Pin Perovskite Solar Cells. *Nat Energy* **2018**, *3* (10), 847–854. https://doi.org/10.1038/s41560-018-0219-8.

(32) Richter, J. M.; Branchi, F.; Valduga de Almeida Camargo, F.; Zhao, B.; Friend, R. H.; Cerullo, G.; Deschler, F. Ultrafast Carrier Thermalization in Lead Iodide Perovskite Probed with Two-Dimensional Electronic Spectroscopy. *Nat Commun* **2017**, *8* (1), 376. https://doi.org/10.1038/s41467-017-00546-z.

(33) Li, M.; Fu, J.; Xu, Q.; Sum, T. C. Slow Hot-Carrier Cooling in Halide Perovskites: Prospects for Hot-Carrier Solar Cells. *Advanced Materials* **2019**, *31* (47), 1802486. https://doi.org/10.1002/adma.201802486.

(34) Lin, W.; Canton, S. E.; Zheng, K.; Pullerits, T. Carrier Cooling in Lead Halide Perovskites: A Perspective on Hot Carrier Solar Cells. *ACS Energy Lett* **2024**, *9* (1), 298–307. https://doi.org/10.1021/acsenergylett.3c02359.

(35) Chen, X.; Kamat, P. V.; Janáky, C.; Samu, G. F. Charge Transfer Kinetics in Halide Perovskites: On the Constraints of Time-Resolved Spectroscopy Measurements. *ACS Energy Lett* **2024**, *9* (6), 3187–3203. https://doi.org/10.1021/acsenergylett.4c00736.

(36) Kiligaridis, A.; Frantsuzov, P. A.; Yangui, A.; Seth, S.; Li, J.; An, Q.; Vaynzof, Y.; Scheblykin, I. G. Are Shockley-Read-Hall and ABC Models Valid for Lead Halide Perovskites? *Nat Commun* **2021**, *12* (1), 3329. https://doi.org/10.1038/s41467-021-23275-w.

(37) van Gorkom, B. T.; van der Pol, T. P. A.; Datta, K.; Wienk, M. M.; Janssen, R. A. J. Revealing Defective Interfaces in Perovskite Solar Cells from Highly Sensitive Sub-Bandgap Photocurrent Spectroscopy Using Optical Cavities. *Nat Commun* **2022**, *13* (1), 349. https://doi.org/10.1038/s41467-021-27560-6.

(38) Wang, K.; Zheng, L.; Hou, Y.; Nozariasbmarz, A.; Poudel, B.; Yoon, J.; Ye, T.; Yang, D.; Pogrebnyakov, A. V.; Gopalan, V.; Priya, S. Overcoming Shockley-Queisser Limit Using Halide Perovskite Platform? *Joule* **2022**, *6* (4), 756–771. https://doi.org/10.1016/j.joule.2022.01.009.

(39) Jin, H.; Debroye, E.; Keshavarz, M.; Scheblykin, I. G.; Roeffaers, M. B. J.; Hofkens, J.; Steele, J. A. It's a Trap! On the Nature of Localised States and Charge Trapping in Lead Halide Perovskites. *Mater Horiz* **2020**, *7* (2), 397–410. https://doi.org/10.1039/C9MH00500E.

(40) Bi, D.; Yi, C.; Luo, J.; Décoppet, J.-D.; Zhang, F.; Zakeeruddin, S. M.; Li, X.; Hagfeldt, A.; Grätzel, M. Polymer-Templated Nucleation and Crystal Growth of Perovskite Films for Solar Cells with Efficiency Greater than 21%. *Nat Energy* **2016**, *1* (10), 16142. https://doi.org/10.1038/nenergy.2016.142.

(41) Yang, W. S.; Noh, J. H.; Jeon, N. J.; Kim, Y. C.; Ryu, S.; Seo, J.; Seok, S. Il. High-Performance Photovoltaic Perovskite Layers Fabricated through Intramolecular Exchange. *Science (1979)* **2015**, *348* (6240), 1234–1237. https://doi.org/10.1126/science.aaa9272.

(42) Zhang, W.; Guo, X.; Cui, Z.; Yuan, H.; Li, Y.; Li, W.; Li, X.; Fang, J. Strategies for Improving Efficiency and Stability of Inverted Perovskite Solar Cells. *Advanced Materials* **2024**. https://doi.org/10.1002/adma.202311025.

(43) Saliba, M.; Matsui, T.; Seo, J.-Y.; Domanski, K.; Correa-Baena, J.-P.; Nazeeruddin, M. K.; Zakeeruddin, S. M.; Tress, W.; Abate, A.; Hagfeldt, A.; Grätzel, M. Cesium-Containing Triple Cation Perovskite Solar Cells: Improved Stability, Reproducibility and High Efficiency. *Energy Environ Sci* **2016**, *9* (6), 1989–1997. https://doi.org/10.1039/C5EE03874J.

(44) Chen, Y.; Meng, Q.; Xiao, Y.; Zhang, X.; Sun, J.; Han, C. B.; Gao, H.; Zhang, Y.; Lu, Y.; Yan, H. Mechanism of PbI_2 in Situ Passivated Perovskite Films for Enhancing the Performance of Perovskite Solar Cells. *ACS Appl Mater Interfaces* **2019**, *11* (47), 44101–44108. https://doi.org/10.1021/acsami.9b13648.

(45) Park, B.; Kedem, N.; Kulbak, M.; Lee, D. Y.; Yang, W. S.; Jeon, N. J.; Seo, J.; Kim, G.; Kim, K. J.; Shin, T. J.; Hodes, G.; Cahen, D.; Seok, S. Il. Understanding How Excess Lead Iodide Precursor Improves Halide Perovskite Solar Cell Performance. *Nat Commun* **2018**, *9* (1), 3301. https://doi.org/10.1038/s41467-018-05583-w.

(46) Jiang, Q.; Zhao, Y.; Zhang, X.; Yang, X.; Chen, Y.; Chu, Z.; Ye, Q.; Li, X.; Yin, Z.; You, J. Surface Passivation of Perovskite Film for Efficient Solar Cells. *Nat Photonics* **2019**, *13* (7), 460–466. https://doi.org/10.1038/s41566-019-0398-2.

(47) Peng, J.; Khan, J. I.; Liu, W.; Ugur, E.; Duong, T.; Wu, Y.; Shen, H.; Wang, K.; Dang, H.; Aydin, E.; Yang, X.; Wan, Y.; Weber, K. J.; Catchpole, K. R.; Laquai, F.; De Wolf, S.; White, T. P. A Universal Double-Side Passivation for High Open-Circuit Voltage in Perovskite Solar Cells: Role of Carbonyl Groups in Poly(Methyl Methacrylate). *Adv Energy Mater* **2018**, *8* (30). https://doi.org/10.1002/aenm.201801208.

(48) Yang, L.; Liu, Z.; Zheng, T.; Li, P.; Ma, J.; Zhang, X.; Wang, X.-F.; Liu, Y. Facilitating Charge Transfer and Band Alignment in Perovskite Solar Cells *via* Interfacial Regulation with a Nb_2CT_x MXene Oxidized Derivative. *J Mater Chem A Mater* **2024**. https://doi.org/10.1039/D4TA03699A.

(49) Wu, B.; Fu, K.; Yantara, N.; Xing, G.; Sun, S.; Sum, T. C.; Mathews, N. Charge Accumulation and Hysteresis in Perovskite-Based Solar Cells: An Electro-Optical Analysis. *Adv Energy Mater* **2015**, *5* (19), 1500829. https://doi.org/10.1002/aenm.201500829.

(50) Bergmann, V. W.; Weber, S. A. L.; Javier Ramos, F.; Nazeeruddin, M. K.; Grätzel, M.; Li, D.; Domanski, A. L.; Lieberwirth, I.; Ahmad, S.; Berger, R. Real-Space Observation of Unbalanced Charge Distribution inside a Perovskite-Sensitized Solar Cell. *Nat Commun* **2014**, *5* (1), 5001. https://doi.org/10.1038/ncomms6001.

(51) Panigrahi, S.; Jana, S.; Calmeiro, T.; Nunes, D.; Martins, R.; Fortunato, E. Imaging the Anomalous Charge Distribution Inside $CsPbBr_3$ Perovskite Quantum Dots Sensitized Solar Cells. *ACS Nano* **2017**, *11* (10), 10214–10221. https://doi.org/10.1021/acsnano.7b04762.

(52) Song, J.-X.; Yin, X.-X.; Li, Z.-F.; Li, Y.-W. Low-Temperature-Processed Metal Oxide Electron Transport Layers for Efficient Planar Perovskite Solar Cells. *Rare Metals* **2021**, *40* (10), 2730–2746. https://doi.org/10.1007/s12598-020-01676-y.

(53) Sharma, D.; Mehra, R.; Raj, B. Comparative Study of Hole Transporting Layers Commonly Used

in High-Efficiency Perovskite Solar Cells. *J Mater Sci* **2022**, *57* (45), 21172–21191. https://doi.org/10.1007/s10853-022-07958-3.

(54) Hu, W.; Yang, S.; Yang, S. Surface Modification of TiO2 for Perovskite Solar Cells. *Trends Chem* **2020**, *2* (2), 148–162. https://doi.org/10.1016/j.trechm.2019.11.002.

(55) Che Halin, D. S.; Azhari, A. W.; Mohd Salleh, M. A. A.; Muhammad Nadzri, N. I.; Vizureanu, P.; Abdullah, M. M. A. B.; Wahab, J. A.; Sandu, A. V. Metal-Doped TiO2 Thin Film as an Electron Transfer Layer for Perovskite Solar Cells: A Review. *Coatings* **2022**, *13* (1), 4. https://doi.org/10.3390/coatings13010004.

(56) Leijtens, T.; Eperon, G. E.; Pathak, S.; Abate, A.; Lee, M. M.; Snaith, H. J. Overcoming Ultraviolet Light Instability of Sensitized TiO2 with Meso-Superstructured Organometal Tri-Halide Perovskite Solar Cells. *Nat Commun* **2013**, *4* (1), 2885. https://doi.org/10.1038/ncomms3885.

(57) Cojocaru, L.; Uchida, S.; Sanehira, Y.; Nakazaki, J.; Kubo, T.; Segawa, H. Surface Treatment of the Compact TiO $_2$ Layer for Efficient Planar Heterojunction Perovskite Solar Cells. *Chem Lett* **2015**, *44* (5), 674–676. https://doi.org/10.1246/cl.150068.

(58) Han, G. S.; Chung, H. S.; Kim, B. J.; Kim, D. H.; Lee, J. W.; Swain, B. S.; Mahmood, K.; Yoo, J. S.; Park, N.-G.; Lee, J. H.; Jung, H. S. Retarding Charge Recombination in Perovskite Solar Cells Using Ultrathin MgO-Coated TiO $_2$ Nanoparticulate Films. *J Mater Chem A Mater* **2015**, *3* (17), 9160–9164. https://doi.org/10.1039/C4TA03684K.

(59) Wang, S.; Liu, G.; Wang, L. Crystal Facet Engineering of Photoelectrodes for Photoelectrochemical Water Splitting. *Chem Rev* **2019**, *119* (8), 5192–5247. https://doi.org/10.1021/acs.chemrev.8b00584.

(60) Sun, S.; He, L.; Yang, M.; Cui, J.; Liang, S. Facet Junction Engineering for Photocatalysis: A Comprehensive Review on Elementary Knowledge, Facet-Synergistic Mechanisms, Functional Modifications, and Future Perspectives. *Adv Funct Mater* **2022**, *32* (1). https://doi.org/10.1002/adfm.202106982.

(61) Du, B.; Wei, Q.; Cai, Y.; Liu, T.; Wu, B.; Li, Y.; Chen, Y.; Xia, Y.; Xing, G.; Huang, W. Crystal Face Dependent Charge Carrier Extraction in TiO2/Perovskite Heterojunctions. *Nano Energy* **2020**, *67*, 104227. https://doi.org/10.1016/j.nanoen.2019.104227.

(62) Ding, Y.; Ding, B.; Kanda, H.; Usiobo, O. J.; Gallet, T.; Yang, Z.; Liu, Y.; Huang, H.; Sheng, J.; Liu, C.; Yang, Y.; Queloz, V. I. E.; Zhang, X.; Audinot, J. N.; Redinger, A.; Dang, W.; Mosconic, E.; Luo, W.; De Angelis, F.; Wang, M.; Dörflinger, P.; Armer, M.; Schmid, V.; Wang, R.; Brooks, K. G.; Wu, J.; Dyakonov, V.; Yang, G.; Dai, S.; Dyson, P. J.; Nazeeruddin, M. K. Single-Crystalline TiO2 Nanoparticles for Stable and Efficient Perovskite Modules. *Nat Nanotechnol* **2022**, *17* (6), 598–605. https://doi.org/10.1038/s41565-022-01108-1.

(63) Castillo-Saenz, J. R.; Nedev, N.; Valdez-Salas, B.; Bernechea, M.; Martínez-Guerra, E.; Mendivil-Palma, I.; Curiel-Alvarez, M.; Mateos, D.; Perez-Landeros, O. Effect of Oxidation Temperature on the Properties of NiOx Layers for Application in Optical Sensors. *Thin Solid Films* **2021**, *734*, 138849. https://doi.org/10.1016/j.tsf.2021.138849.

(64) Xu, L.; Chen, X.; Jin, J.; Liu, W.; Dong, B.; Bai, X.; Song, H.; Reiss, P. Inverted Perovskite Solar Cells Employing Doped NiO Hole Transport Layers: A Review. *Nano Energy* **2019**, *63*, 103860. https://doi.org/10.1016/j.nanoen.2019.103860.

(65) Yin, X.; Guo, Y.; Xie, H.; Que, W.; Kong, L. B. Nickel Oxide as Efficient Hole Transport Materials for Perovskite Solar Cells. *Solar RRL* **2019**, *3* (5). https://doi.org/10.1002/solr.201900001.

(66) Yao, K.; Li, F.; He, Q.; Wang, X.; Jiang, Y.; Huang, H.; Jen, A. K.-Y. A Copper-Doped Nickel

Oxide Bilayer for Enhancing Efficiency and Stability of Hysteresis-Free Inverted Mesoporous Perovskite Solar Cells. *Nano Energy* **2017**, *40*, 155–162. https://doi.org/10.1016/j.nanoen.2017.08.014.

(67) Qiu, Z.; Gong, H.; Zheng, G.; Yuan, S.; Zhang, H.; Zhu, X.; Zhou, H.; Cao, B. Enhanced Physical Properties of Pulsed Laser Deposited NiO Films via Annealing and Lithium Doping for Improving Perovskite Solar Cell Efficiency. *J Mater Chem C Mater* **2017**, *5* (28), 7084–7094. https://doi.org/10.1039/C7TC01224A.

(68) Li, G.; Jiang, Y.; Deng, S.; Tam, A.; Xu, P.; Wong, M.; Kwok, H. Overcoming the Limitations of Sputtered Nickel Oxide for High-Efficiency and Large-Area Perovskite Solar Cells. *Advanced Science* **2017**, *4* (12). https://doi.org/10.1002/advs.201700463.

(69) Zhou, P.; Li, B.; Fang, Z.; Zhou, W.; Zhang, M.; Hu, W.; Chen, T.; Xiao, Z.; Yang, S. Nitrogen-Doped Nickel Oxide as Hole Transport Layer for High-Efficiency Inverted Planar Perovskite Solar Cells. *Solar RRL* **2019**, *3* (10). https://doi.org/10.1002/solr.201900164.

(70) Hietzschold, S.; Hillebrandt, S.; Ullrich, F.; Bombsch, J.; Rohnacher, V.; Ma, S.; Liu, W.; Köhn, A.; Jaegermann, W.; Pucci, A.; Kowalsky, W.; Mankel, E.; Beck, S.; Lovrincic, R. Functionalized Nickel Oxide Hole Contact Layers: Work Function versus Conductivity. *ACS Appl Mater Interfaces* **2017**, *9* (45), 39821–39829. https://doi.org/10.1021/acsami.7b12784.

(71) Bai, Y.; Chen, H.; Xiao, S.; Xue, Q.; Zhang, T.; Zhu, Z.; Li, Q.; Hu, C.; Yang, Y.; Hu, Z.; Huang, F.; Wong, K. S.; Yip, H.; Yang, S. Effects of a Molecular Monolayer Modification of NiO Nanocrystal Layer Surfaces on Perovskite Crystallization and Interface Contact toward Faster Hole Extraction and Higher Photovoltaic Performance. *Adv Funct Mater* **2016**, *26* (17), 2950–2958. https://doi.org/10.1002/adfm.201505215.

(72) Hutter, E. M.; Hofman, J.-J.; Petrus, M. L.; Moes, M.; Abellón, R. D.; Docampo, P.; Savenije, T. J. Charge Transfer from Methylammonium Lead Iodide Perovskite to Organic Transport Materials: Efficiencies, Transfer Rates, and Interfacial Recombination. *Adv Energy Mater* **2017**, *7* (13), 1602349. https://doi.org/10.1002/aenm.201602349.

(73) Caselli, V. M.; Savenije, T. J. Quantifying Charge Carrier Recombination Losses in $MAPbI_3$/C60 and $MAPbI_3$/Spiro-OMeTAD with and without Bias Illumination. *J Phys Chem Lett* **2022**, *13* (32), 7523–7531. https://doi.org/10.1021/acs.jpclett.2c01728.

(74) Levine, I.; Al-Ashouri, A.; Musiienko, A.; Hempel, H.; Magomedov, A.; Drevilkauskaite, A.; Getautis, V.; Menzel, D.; Hinrichs, K.; Unold, T.; Albrecht, S.; Dittrich, T. Charge Transfer Rates and Electron Trapping at Buried Interfaces of Perovskite Solar Cells. *Joule* **2021**, *5* (11), 2915–2933. https://doi.org/10.1016/j.joule.2021.07.016.

(75) Péan, E. V.; Dimitrov, S.; De Castro, C. S.; Davies, M. L. Interpreting Time-Resolved Photoluminescence of Perovskite Materials. *Physical Chemistry Chemical Physics* **2020**, *22* (48), 28345–28358. https://doi.org/10.1039/D0CP04950F.

(76) Siebentritt, S.; Weiss, T. P.; Sood, M.; Wolter, M. H.; Lomuscio, A.; Ramirez, O. How Photoluminescence Can Predict the Efficiency of Solar Cells. *Journal of Physics: Materials* **2021**, *4* (4), 042010. https://doi.org/10.1088/2515-7639/ac266e.

(77) Yang, Y.; Yan, Y.; Yang, M.; Choi, S.; Zhu, K.; Luther, J. M.; Beard, M. C. Low Surface Recombination Velocity in Solution-Grown CH3NH3PbBr3 Perovskite Single Crystal. *Nat Commun* **2015**, *6* (1), 7961. https://doi.org/10.1038/ncomms8961.

(78) Dursun, I.; Maity, P.; Yin, J.; Turedi, B.; Zhumekenov, A. A.; Lee, K. J.; Mohammed, O. F.; Bakr, O. M. Why Are Hot Holes Easier to Extract than Hot Electrons from Methylammonium Lead

Iodide Perovskite? *Adv Energy Mater* **2019**, *9* (22), 1900084. https://doi.org/10.1002/aenm.201900084.

(79) Piatkowski, P.; Cohen, B.; Javier Ramos, F.; Di Nunzio, M.; Nazeeruddin, M. K.; Grätzel, M.; Ahmad, S.; Douhal, A. Direct Monitoring of Ultrafast Electron and Hole Dynamics in Perovskite Solar Cells. *Physical Chemistry Chemical Physics* **2015**, *17* (22), 14674–14684. https://doi.org/10.1039/C5CP01119A.

(80) Horn, J.; Minda, I.; Schwoerer, H.; Schlettwein, D. Direct Observation of Charge Injection From $CH_3NH_3PbI_{3-x}Cl_x$ to Organic Semiconductors Monitored With Sub-Ps Transient Absorption Spectroscopy. *physica status solidi (b)* **2019**, *256* (3), 1800265. https://doi.org/10.1002/pssb.201800265.

(81) Zhang, H.; Liu, M.; Yang, W.; Judin, L.; Hukka, T. I.; Priimagi, A.; Deng, Z.; Vivo, P. Thionation Enhances the Performance of Polymeric Dopant-Free Hole-Transporting Materials for Perovskite Solar Cells. *Adv Mater Interfaces* **2019**, *6* (18), 1901036. https://doi.org/10.1002/admi.201901036.

(82) Handa, T.; Tex, D. M.; Shimazaki, A.; Wakamiya, A.; Kanemitsu, Y. Charge Injection Mechanism at Heterointerfaces in $CH_3NH_3PbI_3$ Perovskite Solar Cells Revealed by Simultaneous Time-Resolved Photoluminescence and Photocurrent Measurements. *J Phys Chem Lett* **2017**, *8* (5), 954–960. https://doi.org/10.1021/acs.jpclett.6b02847.

(83) Baloch, A. A. B.; Alharbi, F. H.; Grancini, G.; Hossain, M. I.; Nazeeruddin, Md. K.; Tabet, N. Analysis of Photocarrier Dynamics at Interfaces in Perovskite Solar Cells by Time-Resolved Photoluminescence. *The Journal of Physical Chemistry C* **2018**, *122* (47), 26805–26815. https://doi.org/10.1021/acs.jpcc.8b07069.

(84) Sheng, R.; Ho-Baillie, A.; Huang, S.; Chen, S.; Wen, X.; Hao, X.; Green, M. A. Methylammonium Lead Bromide Perovskite-Based Solar Cells by Vapor-Assisted Deposition. *The Journal of Physical Chemistry C* **2015**, *119* (7), 3545–3549. https://doi.org/10.1021/jp512936z.

(85) Krogmeier, B.; Staub, F.; Grabowski, D.; Rau, U.; Kirchartz, T. Quantitative Analysis of the Transient Photoluminescence of $CH_3NH_3PbI_3$/$PC_{61}BM$ Heterojunctions by Numerical Simulations. *Sustain Energy Fuels* **2018**, *2* (5), 1027–1034. https://doi.org/10.1039/C7SE00603A.

(86) Makuta, S.; Liu, M.; Endo, M.; Nishimura, H.; Wakamiya, A.; Tachibana, Y. Photo-Excitation Intensity Dependent Electron and Hole Injections from Lead Iodide Perovskite to Nanocrystalline TiO_2 and Spiro-OMeTAD. *Chemical Communications* **2016**, *52* (4), 673–676. https://doi.org/10.1039/C5CC06518F.

(87) Kim, B. J.; Kim, M.; Lee, D. G.; Lee, G.; Bang, G. J.; Jeon, J. B.; Choi, M.; Jung, H. S. Interface Design of Hybrid Electron Extraction Layer for Relieving Hysteresis and Retarding Charge Recombination in Perovskite Solar Cells. *Adv Mater Interfaces* **2018**, *5* (23), 1800993. https://doi.org/10.1002/admi.201800993.

(88) Li, Y.; Zhao, Y.; Chen, Q.; Yang, Y. (Michael); Liu, Y.; Hong, Z.; Liu, Z.; Hsieh, Y.-T.; Meng, L.; Li, Y.; Yang, Y. Multifunctional Fullerene Derivative for Interface Engineering in Perovskite Solar Cells. *J Am Chem Soc* **2015**, *137* (49), 15540–15547. https://doi.org/10.1021/jacs.5b10614.

(89) Xing, G.; Wu, B.; Chen, S.; Chua, J.; Yantara, N.; Mhaisalkar, S.; Mathews, N.; Sum, T. C. Interfacial Electron Transfer Barrier at Compact TiO_2/$CH_3NH_3PbI_3$ Heterojunction. *Small* **2015**, *11* (29), 3606–3613. https://doi.org/10.1002/smll.201403719.

(90) Dursun, I.; Maity, P.; Yin, J.; Turedi, B.; Zhumekenov, A. A.; Lee, K. J.; Mohammed, O. F.; Bakr, O. M. Why Are Hot Holes Easier to Extract than Hot Electrons from Methylammonium Lead

Iodide Perovskite? *Adv Energy Mater* **2019**, *9* (22), 1900084. https://doi.org/10.1002/aenm.201900084.

(91) Shen, Q.; Ogomi, Y.; Chang, J.; Tsukamoto, S.; Kukihara, K.; Oshima, T.; Osada, N.; Yoshino, K.; Katayama, K.; Toyoda, T.; Hayase, S. Charge Transfer and Recombination at the Metal Oxide/$CH_3NH_3PbClI_2$/Spiro-OMeTAD Interfaces: Uncovering the Detailed Mechanism behind High Efficiency Solar Cells. *Phys. Chem. Chem. Phys.* **2014**, *16* (37), 19984–19992. https://doi.org/10.1039/C4CP03073G.

(92) Xing, G.; Mathews, N.; Sun, S.; Lim, S. S.; Lam, Y. M.; Grätzel, M.; Mhaisalkar, S.; Sum, T. C. Long-Range Balanced Electron- and Hole-Transport Lengths in Organic-Inorganic $CH_3NH_3PbI_3$. *Science (1979)* **2013**, *342* (6156), 344–347. https://doi.org/10.1126/science.1243167.

(93) Zheng, F.; Wen, X.; Bu, T.; Chen, S.; Yang, J.; Chen, W.; Huang, F.; Cheng, Y.; Jia, B. Slow Response of Carrier Dynamics in Perovskite Interface upon Illumination. *ACS Appl Mater Interfaces* **2018**, *10* (37), 31452–31461. https://doi.org/10.1021/acsami.8b13932.

(94) Pydzińska, K.; Karolczak, J.; Kosta, I.; Tena-Zaera, R.; Todinova, A.; Idígoras, J.; Anta, J. A.; Ziółek, M. Determination of Interfacial Charge-Transfer Rate Constants in Perovskite Solar Cells. *ChemSusChem* **2016**, *9* (13), 1647–1659. https://doi.org/10.1002/cssc.201600210.

(95) de Quilettes, D. W.; Vorpahl, S. M.; Stranks, S. D.; Nagaoka, H.; Eperon, G. E.; Ziffer, M. E.; Snaith, H. J.; Ginger, D. S. Impact of Microstructure on Local Carrier Lifetime in Perovskite Solar Cells. *Science (1979)* **2015**, *348* (6235), 683–686. https://doi.org/10.1126/science.aaa5333.

(96) Jariwala, S.; Sun, H.; Adhyaksa, G. W. P.; Lof, A.; Muscarella, L. A.; Ehrler, B.; Garnett, E. C.; Ginger, D. S. Local Crystal Misorientation Influences Non-Radiative Recombination in Halide Perovskites. *Joule* **2019**, *3* (12), 3048–3060. https://doi.org/10.1016/j.joule.2019.09.001.

(97) An, Q.; Paulus, F.; Becker-Koch, D.; Cho, C.; Sun, Q.; Weu, A.; Bitton, S.; Tessler, N.; Vaynzof, Y. Small Grains as Recombination Hot Spots in Perovskite Solar Cells. *Matter* **2021**, *4* (5), 1683–1701. https://doi.org/10.1016/j.matt.2021.02.020.

(98) Xu, W.; Du, T.; Sachs, M.; Macdonald, T. J.; Min, G.; Mohan, L.; Stewart, K.; Lin, C.-T.; Wu, J.; Pacalaj, R.; Haque, S. A.; McLachlan, M. A.; Durrant, J. R. Asymmetric Charge Carrier Transfer and Transport in Planar Lead Halide Perovskite Solar Cells. *Cell Rep Phys Sci* **2022**, *3* (5), 100890. https://doi.org/10.1016/j.xcrp.2022.100890.

(99) Braly, I. L.; deQuilettes, D. W.; Pazos-Outón, L. M.; Burke, S.; Ziffer, M. E.; Ginger, D. S.; Hillhouse, H. W. Hybrid Perovskite Films Approaching the Radiative Limit with over 90% Photoluminescence Quantum Efficiency. *Nat Photonics* **2018**, *12* (6), 355–361. https://doi.org/10.1038/s41566-018-0154-z.

(100) Yang, Y.; Yang, M.; Moore, D. T.; Yan, Y.; Miller, E. M.; Zhu, K.; Beard, M. C. Top and Bottom Surfaces Limit Carrier Lifetime in Lead Iodide Perovskite Films. *Nat Energy* **2017**, *2* (2), 16207. https://doi.org/10.1038/nenergy.2016.207.

(101) Wolff, C. M.; Caprioglio, P.; Stolterfoht, M.; Neher, D. Nonradiative Recombination in Perovskite Solar Cells: The Role of Interfaces. *Advanced Materials* **2019**, *31* (52), 1902762. https://doi.org/10.1002/adma.201902762.

(102) Christians, J. A.; Leighton, D. T.; Kamat, P. V. Rate Limiting Interfacial Hole Transfer in Sb_2S_3 Solid-State Solar Cells. *Energy Environ. Sci.* **2014**, *7* (3), 1148–1158. https://doi.org/10.1039/C3EE43844A.

(103) Du, T.; Xu, W.; Xu, S.; Ratnasingham, S. R.; Lin, C.-T.; Kim, J.; Briscoe, J.; McLachlan, M. A.; Durrant, J. R. Light-Intensity and Thickness Dependent Efficiency of Planar Perovskite Solar

Cells: Charge Recombination *versus* Extraction. *J Mater Chem C Mater* **2020**, *8* (36), 12648–12655. https://doi.org/10.1039/D0TC03390A.

(104) Pazos-Outón, L. M.; Szumilo, M.; Lamboll, R.; Richter, J. M.; Crespo-Quesada, M.; Abdi-Jalebi, M.; Beeson, H. J.; Vrućinić, M.; Alsari, M.; Snaith, H. J.; Ehrler, B.; Friend, R. H.; Deschler, F. Photon Recycling in Lead Iodide Perovskite Solar Cells. *Science (1979)* **2016**, *351* (6280), 1430–1433. https://doi.org/10.1126/science.aaf1168.

(105) Richter, J. M.; Abdi-Jalebi, M.; Sadhanala, A.; Tabachnyk, M.; Rivett, J. P. H.; Pazos-Outón, L. M.; Gödel, K. C.; Price, M.; Deschler, F.; Friend, R. H. Enhancing Photoluminescence Yields in Lead Halide Perovskites by Photon Recycling and Light Out-Coupling. *Nat Commun* **2016**, *7* (1), 13941. https://doi.org/10.1038/ncomms13941.

(106) Gan, Z.; Wen, X.; Chen, W.; Zhou, C.; Yang, S.; Cao, G.; Ghiggino, K. P.; Zhang, H.; Jia, B. The Dominant Energy Transport Pathway in Halide Perovskites: Photon Recycling or Carrier Diffusion? *Adv Energy Mater* **2019**, *9* (20). https://doi.org/10.1002/aenm.201900185.

(107) Draguta, S.; Thakur, S.; Morozov, Y. V.; Wang, Y.; Manser, J. S.; Kamat, P. V.; Kuno, M. Spatially Non-Uniform Trap State Densities in Solution-Processed Hybrid Perovskite Thin Films. *J Phys Chem Lett* **2016**, *7* (4), 715–721. https://doi.org/10.1021/acs.jpclett.5b02888.

(108) Kim, J.; Godin, R.; Dimitrov, S. D.; Du, T.; Bryant, D.; McLachlan, M. A.; Durrant, J. R. Excitation Density Dependent Photoluminescence Quenching and Charge Transfer Efficiencies in Hybrid Perovskite/Organic Semiconductor Bilayers. *Adv Energy Mater* **2018**, *8* (35), 1802474. https://doi.org/10.1002/aenm.201802474.

(109) Yamada, Y.; Yamada, T.; Shimazaki, A.; Wakamiya, A.; Kanemitsu, Y. Interfacial Charge-Carrier Trapping in $CH_3NH_3PbI_3$-Based Heterolayered Structures Revealed by Time-Resolved Photoluminescence Spectroscopy. *J Phys Chem Lett* **2016**, *7* (11), 1972–1977. https://doi.org/10.1021/acs.jpclett.6b00653.

(110) Manser, J. S.; Kamat, P. V. Band Filling with Free Charge Carriers in Organometal Halide Perovskites. *Nat Photonics* **2014**, *8* (9), 737–743. https://doi.org/10.1038/nphoton.2014.171.

(111) Trimpl, M. J.; Wright, A. D.; Schutt, K.; Buizza, L. R. V.; Wang, Z.; Johnston, M. B.; Snaith, H. J.; Müller-Buschbaum, P.; Herz, L. M. Charge-Carrier Trapping and Radiative Recombination in Metal Halide Perovskite Semiconductors. *Adv Funct Mater* **2020**, *30* (42), 2004312. https://doi.org/10.1002/adfm.202004312.

(112) Tian, Y.; Peter, M.; Unger, E.; Abdellah, M.; Zheng, K.; Pullerits, T.; Yartsev, A.; Sundström, V.; Scheblykin, I. G. Mechanistic Insights into Perovskite Photoluminescence Enhancement: Light Curing with Oxygen Can Boost Yield Thousandfold. *Physical Chemistry Chemical Physics* **2015**, *17* (38), 24978–24987. https://doi.org/10.1039/C5CP04410C.

(113) Hoke, E. T.; Slotcavage, D. J.; Dohner, E. R.; Bowring, A. R.; Karunadasa, H. I.; McGehee, M. D. Reversible Photo-Induced Trap Formation in Mixed-Halide Hybrid Perovskites for Photovoltaics. *Chem Sci* **2015**, *6* (1), 613–617. https://doi.org/10.1039/C4SC03141E.

(114) Motti, S. G.; Patel, J. B.; Oliver, R. D. J.; Snaith, H. J.; Johnston, M. B.; Herz, L. M. Phase Segregation in Mixed-Halide Perovskites Affects Charge-Carrier Dynamics While Preserving Mobility. *Nat Commun* **2021**, *12* (1), 6955. https://doi.org/10.1038/s41467-021-26930-4.

(115) Gautam, S. K.; Kim, M.; Miquita, D. R.; Bourée, J.; Geffroy, B.; Plantevin, O. Reversible Photoinduced Phase Segregation and Origin of Long Carrier Lifetime in Mixed-Halide Perovskite Films. *Adv Funct Mater* **2020**, *30* (28). https://doi.org/10.1002/adfm.202002622.

(116) Huang, L.; Ge, Z.; Zhang, X.; Zhu, Y. Oxygen-Induced Defect-Healing and Photo-Brightening of

Halide Perovskite Semiconductors: Science and Application. *J Mater Chem A Mater* **2021**, *9* (8), 4379–4414. https://doi.org/10.1039/D0TA10946K.

(117) Fang, H.-H.; Adjokatse, S.; Wei, H.; Yang, J.; Blake, G. R.; Huang, J.; Even, J.; Loi, M. A. Ultrahigh Sensitivity of Methylammonium Lead Tribromide Perovskite Single Crystals to Environmental Gases. *Sci Adv* **2016**, *2* (7). https://doi.org/10.1126/sciadv.1600534.

(118) Scheidt, R. A.; Samu, G. F.; Janáky, C.; Kamat, P. V. Modulation of Charge Recombination in $CsPbBr_3$ Perovskite Films with Electrochemical Bias. *J Am Chem Soc* **2018**, *140* (1), 86–89. https://doi.org/10.1021/jacs.7b10958.

(119) Schelhas, L. T.; Christians, J. A.; Berry, J. J.; Toney, M. F.; Tassone, C. J.; Luther, J. M.; Stone, K. H. Monitoring a Silent Phase Transition in $CH_3NH_3PbI_3$ Solar Cells via *Operando* X-Ray Diffraction. *ACS Energy Lett* **2016**, *1* (5), 1007–1012. https://doi.org/10.1021/acsenergylett.6b00441.

(120) Sandberg, O. J.; Kurpiers, J.; Stolterfoht, M.; Neher, D.; Meredith, P.; Shoaee, S.; Armin, A. On the Question of the Need for a Built-In Potential in Perovskite Solar Cells. *Adv Mater Interfaces* **2020**, *7* (10). https://doi.org/10.1002/admi.202000041.

(121) Jašinskas, V.; Franckevičius, M.; Gelžinis, A.; Chmeliov, J.; Gulbinas, V. Direct Tracking of Charge Carrier Drift and Extraction from Perovskite Solar Cells by Means of Transient Electroabsorption Spectroscopy. *ACS Appl Electron Mater* **2023**, *5* (1), 317–326. https://doi.org/10.1021/acsaelm.2c01346.

(122) Samu, G. F.; Scheidt, R. A.; Kamat, P. V.; Janáky, C. Electrochemistry and Spectroelectrochemistry of Lead Halide Perovskite Films: Materials Science Aspects and Boundary Conditions. *Chemistry of Materials* **2018**, *30* (3), 561–569. https://doi.org/10.1021/acs.chemmater.7b04321.

(123) Hsu, H.-Y.; Ji, L.; Ahn, H. S.; Zhao, J.; Yu, E. T.; Bard, A. J. A Liquid Junction Photoelectrochemical Solar Cell Based on P-Type $MeNH_3PbI_3$ Perovskite with 1.05 V Open-Circuit Photovoltage. *J Am Chem Soc* **2015**, *137* (46), 14758–14764. https://doi.org/10.1021/jacs.5b09758.

(124) Shallcross, R. C.; Zheng, Y.; Saavedra, S. S.; Armstrong, N. R. Determining Band-Edge Energies and Morphology-Dependent Stability of Formamidinium Lead Perovskite Films Using Spectroelectrochemistry and Photoelectron Spectroscopy. *J Am Chem Soc* **2017**, *139* (13), 4866–4878. https://doi.org/10.1021/jacs.7b00516.

(125) Samu, G. F.; Balog, Á.; De Angelis, F.; Meggiolaro, D.; Kamat, P. V.; Janáky, C. Electrochemical Hole Injection Selectively Expels Iodide from Mixed Halide Perovskite Films. *J Am Chem Soc* **2019**, *141* (27), 10812–10820. https://doi.org/10.1021/jacs.9b04568.

(126) Samu, G. F.; Scheidt, R. A.; Balog, Á.; Janáky, C.; Kamat, P. V. Tuning the Excited-State Dynamics of CuI Films with Electrochemical Bias. *ACS Energy Lett* **2019**, *4* (3), 702–708. https://doi.org/10.1021/acsenergylett.9b00182.

(127) Yang, T.; Wu, B.; Ding, C.; Yan, X.; Tian, W.; Jin, S. Proton-Controlled Electron Injection in MoS_2 During Hydrogen Evolution Revealed by Time-Resolved Spectroelectrochemistry. *J Am Chem Soc* **2025**, *147* (5), 4531–4540. https://doi.org/10.1021/jacs.4c16536.

(128) Francàs, L.; Selim, S.; Corby, S.; Lee, D.; Mesa, C. A.; Pastor, E.; Choi, K.-S.; Durrant, J. R. Water Oxidation Kinetics of Nanoporous $BiVO_4$ Photoanodes Functionalised with Nickel/Iron Oxyhydroxide Electrocatalysts. *Chem Sci* **2021**, *12* (21), 7442–7452. https://doi.org/10.1039/D0SC06429G.

(129) Barroso, M.; Mesa, C. A.; Pendlebury, S. R.; Cowan, A. J.; Hisatomi, T.; Sivula, K.; Grätzel, M.; Klug, D. R.; Durrant, J. R. Dynamics of Photogenerated Holes in Surface Modified α-Fe $_2$ O $_3$ Photoanodes for Solar Water Splitting. *Proceedings of the National Academy of Sciences* **2012**, *109* (39), 15640–15645. https://doi.org/10.1073/pnas.1118326109.

(130) Balog, Á.; Janáky, C. The Effect of Trap States on the Optoelectronic Properties of Nanoporous Nickel Oxide. *J Electrochem Soc* **2019**, *166* (5), H3265–H3270. https://doi.org/10.1149/2.0361905jes.

(131) Koenderink, A. F.; Tsukanov, R.; Enderlein, J.; Izeddin, I.; Krachmalnicoff, V. Super-Resolution Imaging: When Biophysics Meets Nanophotonics. *Nanophotonics* **2022**, *11* (2), 169–202. https://doi.org/10.1515/nanoph-2021-0551.

(132) Patrizi, B.; Cozza, C.; Pietropaolo, A.; Foggi, P.; Siciliani de Cumis, M. Synergistic Approach of Ultrafast Spectroscopy and Molecular Simulations in the Characterization of Intramolecular Charge Transfer in Push-Pull Molecules. *Molecules* **2020**, *25* (2), 430. https://doi.org/10.3390/molecules25020430.

(133) Chen, W.; Pham, N. D.; Wang, H.; Jia, B.; Wen, X. Spectroscopic Insight into Efficient and Stable Hole Transfer at the Perovskite/Spiro-OMeTAD Interface with Alternative Additives. *ACS Appl Mater Interfaces* **2021**, *13* (4), 5752–5761. https://doi.org/10.1021/acsami.0c19111.

(134) Kang, G.; Yoon, J.-S.; Kim, G.-W.; Choi, K.; Park, T.; Baek, R.-H.; Lim, J. Electron Trapping and Extraction Kinetics on Carrier Diffusion in Metal Halide Perovskite Thin Films. *J Mater Chem A Mater* **2019**, *7* (45), 25838–25844. https://doi.org/10.1039/C9TA06254H.

(135) Zhu, Z.; Ma, J.; Wang, Z.; Mu, C.; Fan, Z.; Du, L.; Bai, Y.; Fan, L.; Yan, H.; Phillips, D. L.; Yang, S. Efficiency Enhancement of Perovskite Solar Cells through Fast Electron Extraction: The Role of Graphene Quantum Dots. *J Am Chem Soc* **2014**, *136* (10), 3760–3763. https://doi.org/10.1021/ja4132246.

(136) Nussbaum, S.; Socie, E.; Fish, G. C.; Diercks, N. J.; Hempel, H.; Friedrich, D.; Moser, J.-E.; Yum, J.-H.; Sivula, K. Photogenerated Charge Transfer in Dion–Jacobson Type Layered Perovskite Based on Naphthalene Diimide. *Chem Sci* **2023**, *14* (22), 6052–6058. https://doi.org/10.1039/D3SC00783A.

(137) Wang, L.; McCleese, C.; Kovalsky, A.; Zhao, Y.; Burda, C. Femtosecond Time-Resolved Transient Absorption Spectroscopy of $CH_3NH_3PbI_3$ Perovskite Films: Evidence for Passivation Effect of PbI_2. *J Am Chem Soc* **2014**, *136* (35), 12205–12208. https://doi.org/10.1021/ja504632z.

(138) Jain, N.; Zhu, Y.; Maurya, D.; Varghese, R.; Priya, S.; Hudait, M. K. Interfacial Band Alignment and Structural Properties of Nanoscale TiO2 Thin Films for Integration with Epitaxial Crystallographic Oriented Germanium. *J Appl Phys* **2014**, *115* (2). https://doi.org/10.1063/1.4861137.

(139) Rajabathar, J. R.; Al-Lohedan, H. A.; Arokiyaraj, S.; Issa, Z. A.; Dash, C. S.; Murugesan, S.; Khadheer Pasha, S. K.; Al-dhayan, D. M.; Appaturi, J. N. Characterization of Pure Rutile Titania Nanoparticle Prepared by Feasible Method for Coatings and Visible Light-Driven Dye Removal Application. *Coatings* **2021**, *11* (10), 1150. https://doi.org/10.3390/coatings11101150.

(140) Tan, W.; Bowring, A. R.; Meng, A. C.; McGehee, M. D.; McIntyre, P. C. Thermal Stability of Mixed Cation Metal Halide Perovskites in Air. *ACS Appl Mater Interfaces* **2018**, *10* (6), 5485–5491. https://doi.org/10.1021/acsami.7b15263.

(141) McMeekin, D. P.; Sadoughi, G.; Rehman, W.; Eperon, G. E.; Saliba, M.; Hörantner, M. T.; Haghighirad, A.; Sakai, N.; Korte, L.; Rech, B.; Johnston, M. B.; Herz, L. M.; Snaith, H. J. A

Mixed-Cation Lead Mixed-Halide Perovskite Absorber for Tandem Solar Cells. *Science (1979)* **2016**, *351* (6269), 151–155. https://doi.org/10.1126/science.aad5845.

(142) Prathapani, S.; Bhargava, P.; Mallick, S. Electronic Band Structure and Carrier Concentration of Formamidinium–Cesium Mixed Cation Lead Mixed Halide Hybrid Perovskites. *Appl Phys Lett* **2018**, *112* (9). https://doi.org/10.1063/1.5016829.

(143) Jiang, C.-S.; Yang, M.; Zhou, Y.; To, B.; Nanayakkara, S. U.; Luther, J. M.; Zhou, W.; Berry, J. J.; van de Lagemaat, J.; Padture, N. P.; Zhu, K.; Al-Jassim, M. M. Carrier Separation and Transport in Perovskite Solar Cells Studied by Nanometre-Scale Profiling of Electrical Potential. *Nat Commun* **2015**, *6* (1), 8397. https://doi.org/10.1038/ncomms9397.

(144) Harwell, J. R.; Baikie, T. K.; Baikie, I. D.; Payne, J. L.; Ni, C.; Irvine, J. T. S.; Turnbull, G. A.; Samuel, I. D. W. Probing the Energy Levels of Perovskite Solar Cells via Kelvin Probe and UV Ambient Pressure Photoemission Spectroscopy. *Physical Chemistry Chemical Physics* **2016**, *18* (29), 19738–19745. https://doi.org/10.1039/C6CP02446G.

(145) Daboczi, M.; Hamilton, I.; Xu, S.; Luke, J.; Limbu, S.; Lee, J.; McLachlan, M. A.; Lee, K.; Durrant, J. R.; Baikie, I. D.; Kim, J.-S. Origin of Open-Circuit Voltage Losses in Perovskite Solar Cells Investigated by Surface Photovoltage Measurement. *ACS Appl Mater Interfaces* **2019**, *11* (50), 46808–46817. https://doi.org/10.1021/acsami.9b16394.

(146) Zhang, W.; Pathak, S.; Sakai, N.; Stergiopoulos, T.; Nayak, P. K.; Noel, N. K.; Haghighirad, A. A.; Burlakov, V. M.; deQuilettes, D. W.; Sadhanala, A.; Li, W.; Wang, L.; Ginger, D. S.; Friend, R. H.; Snaith, H. J. Enhanced Optoelectronic Quality of Perovskite Thin Films with Hypophosphorous Acid for Planar Heterojunction Solar Cells. *Nat Commun* **2015**, *6* (1), 10030. https://doi.org/10.1038/ncomms10030.

(147) Kwon, H.-C.; Yang, W.; Lee, D.; Ahn, J.; Lee, E.; Ma, S.; Kim, K.; Yun, S.-C.; Moon, J. Investigating Recombination and Charge Carrier Dynamics in a One-Dimensional Nanopillared Perovskite Absorber. *ACS Nano* **2018**, *12* (5), 4233–4245. https://doi.org/10.1021/acsnano.7b07559.

(148) Li, M.; Bhaumik, S.; Goh, T. W.; Kumar, M. S.; Yantara, N.; Grätzel, M.; Mhaisalkar, S.; Mathews, N.; Sum, T. C. Slow Cooling and Highly Efficient Extraction of Hot Carriers in Colloidal Perovskite Nanocrystals. *Nat Commun* **2017**, *8* (1), 14350. https://doi.org/10.1038/ncomms14350.

(149) Jiménez-López, J.; Puscher, B. M. D.; Guldi, D. M.; Palomares, E. Improved Carrier Collection and Hot Electron Extraction Across Perovskite, C_{60}, and TiO_2 Interfaces. *J Am Chem Soc* **2020**, *142* (3), 1236–1246. https://doi.org/10.1021/jacs.9b09182.

(150) Edholm, O.; Blomberg, C. Stretched Exponentials and Barrier Distributions. *Chem Phys* **2000**, *252* (1–2), 221–225. https://doi.org/10.1016/S0301-0104(99)00349-3.

(151) Berberan-Santos, M. N.; Bodunov, E. N.; Valeur, B. Mathematical Functions for the Analysis of Luminescence Decays with Underlying Distributions 1. Kohlrausch Decay Function (Stretched Exponential). *Chem Phys* **2005**, *315* (1–2), 171–182. https://doi.org/10.1016/j.chemphys.2005.04.006.

(152) Hidayat, R.; Nurunnizar, A. A.; Fariz, A.; Herman; Rosa, E. S.; Shobih; Oizumi, T.; Fujii, A.; Ozaki, M. Revealing the Charge Carrier Kinetics in Perovskite Solar Cells Affected by Mesoscopic Structures and Defect States from Simple Transient Photovoltage Measurements. *Sci Rep* **2020**, *10* (1), 19197. https://doi.org/10.1038/s41598-020-74603-x.

(153) Wu, W.; Liao, J.; Zhong, J.; Xu, Y.; Wang, L.; Huang, J. Suppressing Interfacial Charge Recombination in Electron-Transport-Layer-Free Perovskite Solar Cells to Give an Efficiency

Exceeding 21 %. *Angewandte Chemie International Edition* **2020**, *59* (47), 20980–20987. https://doi.org/10.1002/anie.202005680.

(154) Chen, X.; Sárosi, K.; Tóth, B.; Gilicze, B.; Bengery, Z.; Mogyorósi, K.; Janáky, C.; Samu, G. F. Electrochemical Modulation of Hole Extraction in NiO/Perovskite Bilayers. *Adv Mater Interfaces* **2025**. https://doi.org/10.1002/admi.202500159.

(155) Cui, D.; Yang, Z.; Yang, D.; Ren, X.; Liu, Y.; Wei, Q.; Fan, H.; Zeng, J.; Liu, S. (Frank). Color-Tuned Perovskite Films Prepared for Efficient Solar Cell Applications. *The Journal of Physical Chemistry C* **2016**, *120* (1), 42–47. https://doi.org/10.1021/acs.jpcc.5b09393.

(156) Deng, S.; Blach, D. D.; Jin, L.; Huang, L. Imaging Carrier Dynamics and Transport in Hybrid Perovskites with Transient Absorption Microscopy. *Adv Energy Mater* **2020**, *10* (26). https://doi.org/10.1002/aenm.201903781.

(157) DuBose, J. T.; Kamat, P. V. Hole Trapping in Halide Perovskites Induces Phase Segregation. *Acc Mater Res* **2022**, *3* (7), 761–771. https://doi.org/10.1021/accountsmr.2c00076.

(158) Huang, T.; Tan, S.; Nuryyeva, S.; Yavuz, I.; Babbe, F.; Zhao, Y.; Abdelsamie, M.; Weber, M. H.; Wang, R.; Houk, K. N.; Sutter-Fella, C. M.; Yang, Y. Performance-Limiting Formation Dynamics in Mixed-Halide Perovskites. *Sci Adv* **2021**, *7* (46). https://doi.org/10.1126/sciadv.abj1799.

Publication list

Hungarian Scientific Bibliography (MTMT) identifier: 10076162

Publications related to the scientific topic of the dissertation:

1) **Xiangtian Chen**, Krisztina Sárosi, Bálint Tóth, Barnabás Gilicze, Zsolt Bengery, Károly Mogyorósi, Csaba Janáky, Gergely Ferenc Samu, Electrochemical Modulation of Hole Extraction in NiO/Perovskite Bilayers. Adv. Mater. Interfaces **2025**, 10.1002/admi.202500159.

   IF2024 =4.3

2) **Xiangtian, Chen**, Prashant V. Kamat, Csaba Janáky, Gergely Ferenc Samu*****. Charge Transfer Kinetics in Halide Perovskites: On the Constraints of Time-Resolved Spectroscopy Measurements. ACS Energy Lett. **2024**, 9, 3187–3203.

   IF2024 = 19.3

3) **Xiangtian, Chen**, Hannu P. Pasanen, Ramsha Khan, Nikolai V. Tkachenko, Csaba Janáky*****, Gergely Ferenc Samu*****. Effect of Single-Crystal TiO_2/Perovskite Band Alignment on the Kinetics of Electron Extraction. J. Phys. Chem. Lett. **2024**, 15, 2057–2065.

   IF2024 = 4.8

Conferences

Oral presentations:

1) **Chen Xiangtian**, Csaba Janáky, Gergely Ferenc Samu. The effect of single crystal TiO_2/perovskite band alignment on the kinetics of electron extraction.
   XLVI. Chemistry Lectures, 17-19, October 2023, Szeged, Hungary.
2) **Chen Xiangtian**, Csaba Janáky, Gergely Ferenc Samu. Study of the effect of single crystal TiO_2/perovskite band alignment on the kinetics of electron transfer.
   Solar2Chem conference, 18-22, September 2023, Tarragona, Spain.
3) **Chen Xiangtian**, Csaba Janáky, Gergely Ferenc Samu. Crystal facet dependent electron extraction at TiO_2/perovskite revealed by time resolved spectroscopy
   Solar2Chem EPFL workshop, 22-24, May 2023, Lausanne, Switzerland
4) **Chen Xiangtian**, Csaba Janáky, Gergely Ferenc Samu. Investigation of electron extraction at TiO_2/perovskite interface by time resolved spectroscopy.
   Solar2Chem Cambridge workshop, 6-9, December 2022, Cambridge, UK

Poster presentations:

1) **Chen Xiangtian**, Csaba Janáky, Gergely Ferenc Samu. Crystal Facet Dependent Electron Extraction in TiO_2/Perovskite Revealed by Time Resolved Photoluminescence and Transient Absorption Spectroscopy.
   Solar2chem Winter School, 22-24, February 2023, Valencia, Spain
2) **Chen Xiangtian**, Csaba Janáky, Gergely Ferenc Samu. The Application of Photoluminescence Spectroscopy in Perovskite Based Solar Cell/Photoelectrodes Study.
   Solar2Chem X Seafuel Symposium, 1st, April 2022, Tenerife, Spain

Acknowledgements

Doing a Ph.D. is never an easy task, especially doing it in a country far away from home. I need to thank many individuals from different countries, who accompany me through this difficult, but inspiring journey.

Firstly, I would like to express my gratitude to **Prof. Ágota Tóth**, head of the Department of Physical Chemistry and Materials Science, for the opportunity to attend and finish the doctoral studies.

I am grateful to my supervisors for the guidance and support in research work. **Dr. Csaba Janáky** taught me research attitudes and trained my critical thinking skills. His questions in group meetings are always valuable. **Dr. Gergely F. Samu** worked closely with me. He taught me all the experimental details. We had weekly discussions on all the difficulties and challenges I confronted in research work. During this Ph.D., I had the opportunity to visit a research group guided by **Prof. Nikolai V. Tkachenko** in Finland. Although he's not my "official" supervisor, he taught me transient absorption spectroscopy and helped with my first paper.

I would like to thank all colleagues and friends at Szeged: **John Mark Christian M. Dela Cruz**, **Dr. Zheng Zhang**, **Cintia Hajdú**, **Dr. Hye Won Jeong**, **Dr. Chanderpratap Singh**, **Dr. Egon Kecsenovity**, **Dr. Ádám Balog**, **Dr. Gábor Bencsik**, **Katalin Sziveri**, and from Solar2chem program: **Jokotadeola Adeoluwa Odutola**, **Dr. Kathrin Naumann**, **Francesca Lorenzutti**, **Dr. Pavle Nikačević** and so on, and from Finland: **Dr. Hannu P. Pasanen** and **Dr. Ramsha Khan**. My Ph.D. life was enriched because of the existence of these people. It was also them who accompanied me through all the difficult days so that I can make the accomplishment finally.

Last but not least, I owe my deepest gratitude to **my parents** for their unconditional love and support. Their faith in me and their constant encouragement have been my anchor throughout this demanding journey.

Appendix

Table A1. Details of the fitting parameters obtained with the different evaluation methods of the TRPL decay curves.

	Sample	Method	A_1	τ_1 (ns)	A_2	τ_2 (ns)	β	A_3	τ_3 (ns)	τ_{eff} (ns)
Exponential fitting	Glass/perovskite	Bi-exponential	-	-	0.74	22.1	-	0.26	84.2	28.0
	TiO_2/perovskite	Bi-exponential	-	-	0.82	11.2	-	0.18	49.0	13.5
		Tri-exponential	0.43	3.4	0.49	17.6	-	0.08	64.9	-
Stretched exponential fitting	Glass/perovskite	Bi-exponential			0.88	23.9	0.88	0.12	117.7	-
	TiO_2/perovskite	Add one more exponential component	0.69	11.6	0.29	23.9	0.88	0.02	117.8	-

Table A2. Details of fitting parameters for different evaluation methods of the TA decay traces.

	Sample	Method	A_1	τ_1 (ns)	A_2	τ_2 (ns)	A_3	τ_3 (ns)	β	τ_{eff} (ns)
Exponential fitting	Glass/ perovskite	Bi-exponential	-	-	0.26	1.1	0.74	10.8	-	7.5
	TiO_2/ perovskite	Bi-exponential	-	-	0.27	0.9	0.73	6.4	-	4.9
		Tri-exponential	0.03	0.2	0.50	1.8	0.47	11.9	-	-
Stretched exponential fitting	Glass/ perovskite	Mono-exponential	-	-	-	-	1.00	6.7	0.67	-
	TiO_2/ perovskite	Mono-exponential	-	-	-	-	1.00	3.6	0.67	-
	TiO_2/ perovskite	Bi-exponential	-	-	0.3	1.9	0.67	6.7	0.67	-

Table A3. Fitting details, calculated average lifetime and apparent rate constant k of mp-NiO/$FA_{0.83}Cs_{0.17}PbI_3$ at different excitation fluences.

Fluence ($\mu J/cm^2$)	A_1	T_1 (ps)	A_2	T_2 (ps)	A_3	T_3 (ps)	Average lifetime (ps)	k (ns^{-1})
32	0.37	5217	0.42	552	0.23	72	2178	0.46
25	0.45	5217	0.51	280	-	-	2496	0.40
19	0.53	5217	0.44	303	-	-	2902	0.34
16	0.57	5217	0.37	578	-	-	3201	0.31
13	0.63	5217	0.33	562	-	-	3480	0.29
10	0.74	5217	0.22	493	-	-	3974	0.25
6	1.00	5217	-	-	-	-	5217	0.19

Table A4. Fitting details, calculated average lifetime and apparent rate constant k of mp-NiO/$FA_{0.83}Cs_{0.17}Pb(I_{0.83}Br_{0.17})_3$ at different excitation fluences.

Fluence ($\mu J/cm^2$)	A_1	T_1 (ps)	A_2	T_2 (ps)	A_3	T_3 (ps)	Average lifetime (ps)	k (ns^{-1})
32	0.29	1619	0.31	286	0.41	72	587	1.70
25	0.33	1619	0.32	253	0.35	69	639	1.56
19	0.44	1619	0.52	146	-	-	791	1.26
16	0.52	1619	0.48	144	-	-	911	1.10
13	0.58	1619	0.35	193	-	-	1011	0.99
10	0.74	1619	0.23	232	-	-	1253	0.80
6	1.00	1619	-	-	-	-	1619	0.62

Table A5. Fitting details, calculated average lifetime and apparent rate constant k of mp-NiO/$FA_{0.83}Cs_{0.17}Pb(I_{0.6}Br_{0.4})_3$ at different excitation fluences.

Fluence ($\mu J/cm^2$)	A_1	T_1 (ps)	A_2	T_2 (ps)	A_3	T_3 (ps)	Average lifetime (ps)	k (ns^{-1})
32	0.34	5216	0.48	373	0.1	39	1957	0.51
25	0.43	5216	0.54	329	-	-	2426	0.41
19	0.45	5216	0.5	476	-	-	2598	0.39
16	0.48	5216	0.48	542	-	-	2775	0.36
13	0.33	5216	0.59	1519	-	-	2695	0.37
10	1.00	5216	-	-	-	-	5216	0.19
6	1.00	5576	-	-	-	-	5576	0.18

Table A6. Fitting parameters, average lifetime and apparent rate constant (k) of mp-NiO/$FA_{0.83}Cs_{0.17}PbI_3$ at applied potential of 0.4 V vs. Ag/AgCl at various excitation fluence.

Fluence ($\mu J/cm^2$)	A_1	T_1 (ps)	A_2	T_2 (ps)	A_3	T_3 (ps)	Average lifetime (ps)	k (ns^{-1})
25	0.70	1698	0.25	127	-	-	1222	0.82
19	0.79	1698	0.27	85	-	-	1363	0.73
16	0.88	1698	0.19	180	-	-	1526	0.66
13	1.00	1698	-	-	-	-	1698	0.59
10	1.00	2573	-	-	-	-	2573	0.39
6	1.00	2577	-	-	-	-	2577	0.39

Table A7. Fitting parameters, average lifetime and apparent rate constant (k) of mp-NiO/$FA_{0.83}Cs_{0.17}PbI_3$ at applied potential of 0 V vs. Ag/AgCl at various excitation fluence.

Fluence ($\mu J/cm^2$)	A_1	T_1 (ps)	A_2	T_2 (ps)	A_3	T_3 (ps)	Average lifetime (ps)	k (ns^{-1})
25	0.62	1731	0.34	130	-	-	1119	0.89
19	0.76	1731	0.23	36	-	-	1324	0.76
16	0.84	1731	0.08	272	-	-	1478	0.68
13	1.00	1731	-	-	-	-	1731	0.58
10	1.00	3387	-	-	-	-	3387	0.30
6	1.00	4532	-	-	-	-	4532	0.22

Table A8. Fitting parameters, average lifetime and apparent rate constant (k) of mp-NiO/$FA_{0.83}Cs_{0.17}PbI_3$ at applied potential of -0.4 V vs. Ag/AgCl at various excitation fluence.

Fluence ($\mu J/cm^2$)	A_1	T_1 (ps)	A_2	T_2 (ps)	A_3	T_3 (ps)	Average lifetime (ps)	k (ns^{-1})
25	0.22	1717	0.45	452	0.35	58	601.0419608	1.7
19	0.54	1717	0.38	223	-	-	1019	0.98
16	0.74	1717	0.17	153	-	-	1299	0.77
13	1.00	1717	-	-	-	-	1717	0.58
10	1.00	2046	-	-	-	-	2046	0.49
6	1.00	2031	-	-	-	-	2031	0.49

Table A9. Fitting parameters, average lifetime and apparent rate constant (k) of mp-

$NiO/FA_{0.83}Cs_{0.17}PbI_3$ at various potentials at the excitation fluence of 19 μJ/cm^2.

Potential (V vs. Ag/AgCl)	A_1	T_1 (ps)	A_2	T_2 (ps)	A_3	T_3 (ps)	Average lifetime (ps)	k (ns^{-1})
0.4	0.73	1910	0.28	101	-	-	1423	0.70
0.2	0.77	1910	0.32	132	-	-	1513	0.66
0	0.68	1910	0.27	118	-	-	1332	0.75
-0.2	0.61	1910	0.3	182	-	-	1225	0.82
-0.4	0.59	1910	0.4	149	-	-	1187	0.84
-0.2	0.62	1910	0.34	189	-	-	1251	0.80
0	0.67	1910	0.3	112	-	-	1314	0.76
0.2	0.69	1910	0.23	140	-	-	1353	0.74
0.4	0.69	1910	0.3	211	-	-	1382	0.72

Table A10. Fitting parameters, average lifetime and apparent rate constant (k) of mp-$NiO/FA_{0.83}Cs_{0.17}Pb(I_{0.83}Br_{0.17})_3$ at applied potential of 0.4 V vs. Ag/AgCl at various excitation fluence.

Fluence (μJ/cm^2)	A_1	T_1 (ps)	A_2	T_2 (ps)	A_3	T_3 (ps)	Average lifetime (ps)	k (ns^{-1})
25	0.24	2192	0.31	44	0.43	243	646	1.55
19	0.3	2192	0.21	31	0.50	223	775	1.29
16	0.48	2192	0.46	220	-	-	1160	0.86
13	0.62	2192	0.29	192	-	-	1420	0.70
10	0.74	2192	0.24	124	-	-	1652	0.61
6	1.00	2192	-	-	-	-	2192	0.46

Table A11. Fitting parameters, average lifetime and apparent rate constant (k) of mp-$NiO/FA_{0.83}Cs_{0.17}Pb(I_{0.83}Br_{0.17})_3$ at applied potential of 0 V vs. Ag/AgCl at various excitation fluence.

Fluence (μJ/cm^2)	A_1	T_1 (ps)	A_2	T_2 (ps)	A_3	T_3 (ps)	Average lifetime (ps)	k (ns^{-1})
25	0.009	2396	0.73	72	0.25	644	236	4.24
19	0.06	2396	0.6	319	0.35	53	354	2.83
16	0.18	2396	0.54	449	0.28	52	768	1.45
13	0.48	2396	0.44	248	-	-	1269	0.79
10	0.63	2396	0.33	336	-	-	1625	0.62
6	1.00	2396	-	-	-	-	2396	0.42

Table A12. Fitting parameters, average lifetime and apparent rate constant (k) of mp-

NiO/$FA_{0.83}Cs_{0.17}Pb(I_{0.83}Br_{0.17})_3$ at applied potential of -0.4 V vs. Ag/AgCl at various excitation fluence.

Fluence ($\mu J/cm^2$)	A_1	T_1 (ps)	A_2	T_2 (ps)	A_3	T_3 (ps)	Average lifetime (ps)	k (ns^{-1})
25	0.03	2242	0.31	198	0.75	39	155	6.43
19	0.03	2242	0.65	73	0.38	308	225	4.44
16	0.14	2242	0.37	31	0.52	337	495	2.02
13	0.24	2242	0.49	639	0.27	93	967	1.03
10	0.62	2242	0.36	346	-	-	1517	0.66
6	1.00	2242	-	-	-	-	2242	0.45

Table A13. Fitting parameters, average lifetime and apparent rate constant (k) of mp-NiO/$FA_{0.83}Cs_{0.17}Pb(I_{0.83}Br_{0.17})_3$ at various potentials at the excitation fluence of 19 $\mu J/cm^2$.

Potential (V vs. Ag/AgCl)	A_1	T_1 (ps)	A_2	T_2 (ps)	A_3	T_3 (ps)	Average lifetime (ps)	k (ns^{-1})
0.4	1	1080	-	-	-	-	1080	0.93
0.2	0.6	1080	0.27	99	-	-	675	1.48
0	0.46	1080	0.51	93	-	-	546	1.83
-0.2	0.67	1080	0.28	22	-	-	730	1.37
-0.4	0.24	1080	0.4	23	0.38	128	316	3.16
-0.2	0.34	1080	0.46	17	0.38	223	447	2.24
0	0.27	1080	0.41	62	0.34	560	504	1.99
0.2	0.42	1080	0.46	663	-	-	800	1.25
0.4	0.76	1080	0.14	63	-	-	831	1.20